Time-Reversal Symmetry Breaking in Quantum Billiards

Vom Fachbereich Physik
der Technischen Universität Darmstadt

zur Erlangung des Grades
eines Doktors der Naturwissenschaften
(Dr. rer. nat.)

genehmigte

D i s s e r t a t i o n

angefertigt von

Dipl.-Phys. Florian Schäfer
aus Dieburg

Darmstadt 2009
D 17

Referent:	Professor Dr. rer. nat. Dr. h.c. mult. A. Richter
Korreferent:	Professor Dr. rer. nat. J. Wambach
Tag der Einreichung:	1. Dezember 2008
Tag der Prüfung:	26. Januar 2009

Abstract

The present doctoral thesis describes experimentally measured properties of the resonance spectra of flat microwave billiards with partially broken time-reversal invariance induced by an embedded magnetized ferrite. A vector network analyzer determines the complex scattering matrix elements. The data is interpreted in terms of the scattering formalism developed in nuclear physics.

At low excitation frequencies the scattering matrix displays isolated resonances. At these the effect of the ferrite on isolated resonances (singlets) and pairs of nearly degenerate resonances (doublets) is investigated. The hallmark of time-reversal symmetry breaking is the violation of reciprocity, i.e. of the symmetry of the scattering matrix. One finds that reciprocity holds in singlets; it is violated in doublets. This is modeled by an effective Hamiltonian of the resonator. A comparison of the model to the data yields time-reversal symmetry breaking matrix elements in the order of the level spacing. Their dependence on the magnetization of the ferrite is understood in terms of its magnetic properties.

At higher excitation frequencies the resonances overlap and the scattering matrix elements fluctuate irregularly (Ericson fluctuations). They are analyzed in terms of correlation functions. The data are compared to three models based on random matrix theory. The model by Verbaarschot, Weidenmüller and Zirnbauer describes time-reversal invariant scattering processes. The one by Fyodorov, Savin and Sommers achieves the same for systems with complete time-reversal symmetry breaking. An extended model has been developed that accounts for partial breaking of time-reversal invariance. This extended model is in general agreement with the data, while the applicability of the other two models is limited. The cross-correlation function between forward and backward reactions determines the time-reversal symmetry breaking matrix elements of the Hamiltonian to up to 0.3 mean level spacings. Finally the sensitivity of the elastic enhancement factor to time-reversal symmetry breaking is studied. Based on the data elastic enhancement factors below 2 are found which is consistent with breaking of time-reversal invariance in the regime of overlapping resonances.

The present work provides the framework to probe for broken time-reversal invariance in any scattering data by a multitude of methods in the whole range between isolated and overlapping resonances.

Zusammenfassung

Die vorliegende Doktorarbeit beschreibt Eigenschaften experimentell gemessener Resonanzspektren flacher Mikrowellenbillards. Hierbei induziert ein in den Resonator eingebrachter magnetisierter Ferrit eine partiell gebrochene Zeitumkehrinvarianz. Ein Vektor-Netzwerkanalysator bestimmt die komplexen Streumatrixelemente. Die Daten werden im Rahmen der in der Kernphysik entwickelten Streutheorie interpretiert.

Bei niedrigen Anregungsfrequenzen zeigt die Streumatrix isolierte Resonanzen. An diesen wird der Einfluss des Ferriten auf einzelne Resonanzen (Singuletts) und auf Paare fast entarteter Resonanzen (Dubletts) untersucht. Ein Merkmal für Zeitumkehrbrechung ist die Verletzung der Reziprozität, also der Symmetrie der Streumatrix. Die Experimente belegen, dass Reziprozität in Singuletts gilt und in Dubletts verletzt wird. Sie werden durch einen effektiven Hamilton-Operator modelliert. Ein Vergleich des Modells mit den Daten ergibt zeitumkehrbrechende Matrixelemente in der Größe des Niveauabstands, deren Abhängigkeit von der Magnetisierung des Ferriten durch dessen Eigenschaften verstanden ist.

Bei hohen Frequenzen überlappen die Resonanzen und die Streumatrixelemente fluktuieren irregulär (Ericson Fluktuationen). Sie werden anhand von Korrelationsfunktionen analysiert. Die Daten werden mit drei Modellen verglichen. Das Modell von Verbaarschot, Weidenmüller und Zirnbauer beschreibt zeitumkehrinvariante Streuprozesse, jenes von Fyodorov, Savin und Sommers leistet das gleiche für Systeme mit vollständig gebrochener Zeitumkehrsymmetrie. Ein erweitertes Modell für den Fall einer teilweise gebrochenen Symmetrie wurde entwickelt und angewandt. Es ist in guter Übereinstimmung mit den Daten, wohingegen die Anwendbarkeit der bekannten Modelle limitiert ist. Die Kreuzkorrelationsfunktion zwischen Reaktionen in Vorwärts- und Rückwärtsrichtung ermittelt symmetriebrechende Matrixelemente von bis zu 0.3 mittleren Niveauabständen. Schließlich wird die Sensitivität des elastischen Verstärkungsfaktors auf Zeitumkehrbrechung untersucht. Verstärkungsfaktoren kleiner 2 werden beobachtet. Dies ist konsistent mit Zeitumkehrbrechung im Bereich überlappender Resonanzen.

Die vorliegende Arbeit stellt den Rahmen dar, um mit einer Vielzahl von Methoden beliebige Streudaten auf gebrochene Zeitumkehrsymmetrie im kompletten Bereich von isolierten bis hin zu überlappenden Resonanzen zu untersuchen.

Contents

1 Introduction

In 1686, Sir Isaac Newton presented to the Royal Society the first of the three books in his series *Philosophiae naturalis principia mathematica* [1], revolutionizing science. In this book he presented three laws that should describe classical mechanics once and for all: First, a body maintains its state unless a net force acts on it; second, this force equals the change of momentum of the body; third, every action demands for an equal and opposite reaction. As a consequence the fate of every particle in the universe seemed to be already decided as the knowledge of its current state should suffice to describe its future state for eternity.

More than 200 years passed until Jules Henri Poincaré published *Les Méthodes nouvelles de la Mécanique Céleste* in 1892 [2]. In this work he proved that the motion of more than two orbiting bodies in phase space cannot be predicted for arbitrary times, since one cannot expand the solution of Newton's equations in a convergent Taylor series with respect to time. It was more than 50 years later, when this problem of long-time prediction in mechanics was successfully tackled by Kolmogorov [3], followed by Arnold [4] and Moser [5]. The combined result is now known as the KAM theory [6] and states that in weakly perturbed conservative many-body systems some stable orbits still remain. However, for most initial conditions the orbits become unstable (their series expansions do not converge) and non-periodic in their time evolution, a feature later termed as *chaos* [7]. The occurrence of this chaotic behavior is not in contradiction to Newton's laws. His equations correctly describe classical dynamics, it is just that their solutions cannot always be formulated explicitly.

A prototype to study the rich dynamics of classical mechanics was found in *billiards* [8–10]—an area bounded by hard walls in which particles move freely. Already in the early 1970s interest arose on the question of how chaotic properties of classical billiards translate into the world of quantum mechanics, giving birth to the field of *quantum chaos*. It was clear that familiar concepts such as orbits in phase space do not directly apply to quantum systems. Nevertheless, due to the strong ties to their classical counterparts, the question of universal features of these *quantum billiards* was posed [11, 12]. It turned out that, indeed, universal spectral properties do exist which can be described to high precision by a statistical approach, the so-called *random matrix theory* [13]. Another method

to describe quantum billiards is used by a semiclassical treatment, the so-called periodic orbit theory [14, 15], where the system is characterized in terms of all its classical periodic orbits.

Experimentally, a most successful analog system for quantum billiards is provided by flat microwave resonators [16–19]. In Sec. 2 of the present work the basic concepts of these experiments are recapitulated. Since 1994, the experimental investigation of quantum billiards included systems with broken time-reversal symmetry, achieved by the insertion of magnetized ferrites [20, 21]. Section 3 of the present work is dedicated to the explanation of this type of *induced* time-reversal symmetry breaking in microwave billiards. Before this advancement in the experimental technique the study of quantum billiards was limited to the investigation of generic features of integrable and chaotic systems with time-reversal symmetry. The breaking of this symmetry gave access to the investigation of universal features of chaotic systems without time-reversal invariance and permitted additional comparisons with random matrix theory in this regime. While those early microwave experiments mostly focused on spectral properties, the present work directly investigated the scattering process.

In the 1960s an important discovery was made in a different field of physics: Christenson, Cronin, Fitch and Turlay obtained evidence for the decay of the neutral K-meson into two pions [22]. This implies the simultaneous violation of charge (C) and parity (P) conservation in the weak interaction. Relativistic field theory requires that the combined symmetry of charge, parity and time-reversal (CPT) holds. Therefore, the experiment of Christenson *et al.* entailed a violation of time-reversal ($\mathcal{T}$) symmetry[1]. Subsequently, much effort was devoted to search for $\mathcal{T}$ non-conserving contributions to the strong interaction in nuclear reactions [24–30]. Until the present day, only upper limits of the order of 10^{-3} for contributions of $\mathcal{T}$ non-conserving effects to the total scattering amplitude could be established [31, 32]. These experiments exploited fluctuations in nuclear cross sections that were first pointed to, albeit for $\mathcal{T}$ invariant systems, by Torleif Ericson [33] in 1960. He realized that in energy regions in which a large number of

[1] In a strict sense, there is no symmetry connected to time-reversal. The operator of time-reversal is antiunitary (see Sec. 2.2) and therefore not related to any conserved quantum number [23]. As a consequence, time-reversal invariance—which is a more proper terminology—is not related to a symmetry. However, usage of the term "time-reversal symmetry" is common and well established in the literature and will therefore be used with the above remark in mind in the present work, too.

resonant states overlap, cross sections are not structureless functions of energy but rather display pronounced fluctuations, now called *Ericson fluctuations*. Later, this led him to the conclusion that effects of $\mathcal{T}$ breaking are best observed in this regime [34, 35] by virtue of an enhancement mechanism.

It was believed for some time that effects of $\mathcal{T}$ violation cannot manifest themselves in nuclear reactions proceeding via an isolated resonance [36]. In 1975 it was pointed out [37], however, that this is not true for differential cross sections if reaction channels with different spins can interfere. Experiments followed this insight some years later [38]. Using a setup where $\mathcal{T}$ violating effects should have been detectable it was established that within the experimental uncertainties $\mathcal{T}$ invariance holds. Until recently [39], this concept has never been carried over to quantum billiards with their possibilities of controlled $\mathcal{T}$ breaking. Therefore, Sec. 4 of the present work discusses the traceability of time-reversal symmetry breaking by investigations of isolated resonances in detail.

This study of isolated resonances already demonstrates that quantum billiards do not only serve as a paradigm for the investigation of eigenvalue and wave function properties, they also provide a tool to investigate properties of scattering systems [16, 40–42]. The connection between the properties of the Hamiltonian of the closed billiard and the scattering process has been given by Albeverio *et al.* [41]. Their description is identical to the one formulated by Mahaux and Weidenmüller [43] for nuclear reactions. The process of scattering implies a connection of the formerly closed quantum system to the outside world. Thus it is closely linked to the investigations of open systems in general, where interest due to rapid progress in nanotechnology and the development of new mesoscopic devices is currently high [44–46]. Resonances of open systems have short lifetimes which is equivalent to large resonance widths Γ. If the widths are comparable to the mean level spacing D, that is $\Gamma/D \approx 1$, the resonances overlap. In this regime the conductance (the universal measure of electron transport) fluctuates in analogy to the Ericson fluctuations in compound nucleus reactions [47]. A theoretical description of these fluctuations for all values of Γ/D is challenging and was achieved in 1984 by Verbaarschot, Weidenmüller and Zirnbauer (VWZ) [48] for $\mathcal{T}$ invariant systems. Their analytic expression predicts the correlation functions of the fluctuations and is applicable not only in the regime of fully overlapping resonances but also in that of partially overlapping and isolated ones. It took more

than twenty years to rigorously confirm the predictions of this model [49]. These developments are further pursued in Sec. 5 of the present work and correlation functions of open, $\mathcal{T}$ non-invariant systems are studied. In these investigations a second model by Fyodorov, Savin and Sommers (FSS) [50] is considered, too, that provides the information analog to the VWZ model but for the case of fully broken $\mathcal{T}$ symmetry.

Both models, VWZ and FSS, only approximately describe microwave resonator experiments with magnetized ferrites. Section 6 of the present work proves that the induced $\mathcal{T}$ breaking is incomplete. This motivated an extension of the VWZ formalism to the regime of partial $\mathcal{T}$ violation. The application of this model in the present work proves its validity in the whole range between isolated and overlapping resonances as well as for a large variety of $\mathcal{T}$ breaking strengths. Coming back to conductance properties of mesoscopic devices with magnetic fields, the phenomenon of weak localization [51], known as *elastic enhancement* in nuclear reactions, is investigated at the end of the present work and considered as another tool to detect consequences of time-reversal symmetry breaking.

The present thesis provides a basis to probe the dynamics of general quantum systems with respect to time-reversal invariance. The exploited theoretical concepts originate from nuclear physics. There the question of $\mathcal{T}$ non-conserving contributions to the strong interaction is of fundamental interest. The present work used microwave billiards to model the compound nucleus. A ferrite induced $\mathcal{T}$ breaking in the resonators and simulated a hypothetical time-reversal symmetry breaking amplitude of the strong interaction. The introduced methods allow for investigations of $\mathcal{T}$ breaking effects in the whole range between isolated and overlapping resonances. Applications in the broader scope of general scattering systems, to study e.g. the fluctuation properties of the conductance in mesoscopic devices [44] or in Rydberg atoms [52, 53], are now feasible.

2 Basics

The present work rests upon five pillars. Experiments on *microwave resonators*, a technique perfected by years of experience in the field of experimental quantum chaos and progress in microwave technology, provide the data basis for all analyses. To understand the experimental findings methods from *nuclear physics* as well from *quantum chaos* are employed. The statistical properties of the latter of which can, to high precision, be modeled by *random matrix theory*. Quantum mechanics contributes the theory of broken *time-reversal invariance*. This section gives short introductions to each of these topics.

2.1 Quantum chaos and quantum billiards

In classical physics every system can be described by a Hamiltonian function. This leads to a set of first order differential equations which implies that knowledge of the initial condition of every variable and parameter of the system is sufficient to predict the state of the system for arbitrary times in the future. However, in reality every initial condition, as for example position or momentum, can only be determined up to some finite precision, thus introducing uncertainty into the prediction of future development that generally increases in time. The rate of uncertainty growth can either be linear or exponential in time which serves to distinguish between classical *regular* and classical, deterministic *chaotic* dynamics. In an at least two-dimensional, flat potential the difference between these two cases is caused by the boundary, where the potential jumps to infinity. Thus the term *billiard* is commonly used to refer to those systems.

Physically, the dependence of the dynamics on the shape of the billiard boundary can be explained by the symmetries it defines. A classical system with N degrees of freedom is called integrable if a set of N constants of the motion exist, restricting the flow of particle trajectories in the $2N$-dimensional phase space to an N-dimensional surface [54]. According to Noether's theorem every symmetry of the Hamiltonian corresponds to one conserved quantity [55], each a constant of the motion. If now the billiard is found to be integrable, solutions of Hamilton's

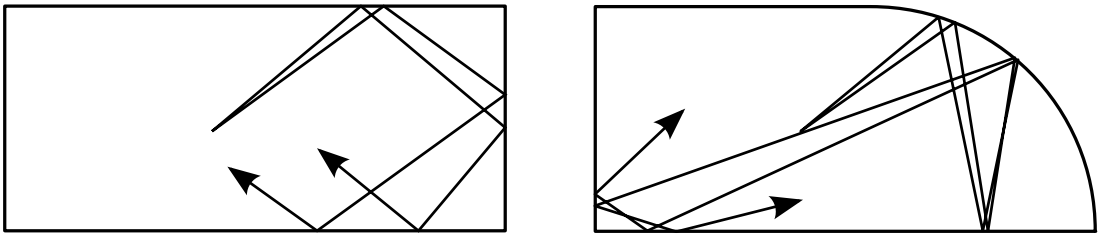

a) regular b) chaotic

Fig. 2.1: Examples of classical trajectories in two billiard shapes: a) In a billiard with a rectangular boundary the distance between particles with slightly different initial momenta increases linearly in time. The motion is regular. b) In the Bunimovich billiard [9], shaped like a quarter stadium, the distance grows exponentially in time. This is a characteristic feature of chaotic dynamics.

equations can be given in closed form and uncertainties grow at most linearly in time. The dynamics is regular (see Fig. 2.1a). In contrast, the lack of symmetries reduces the number of constants of the motion (see Fig. 2.1b). For the trajectory of a particle no analytical expression exists, and approximations in the form of series expansions diverge [54]. This leads to so-called deterministic chaos, as ever so small uncertainties in the initial conditions will grow exponentially in time rendering any long term predictions impossible.

The term *quantum chaos* includes all quantum mechanical systems whose classical analogs would display chaotic behavior. Of special interest are *quantum billiards* whose potentials are, but for infinitely high potential boundaries, flat, in analogy to classical billiards. It was discovered that both, the eigenvalues and the eigenfunctions, of chaotic quantum billiards exhibit universal statistical properties [56]. Their description is a major goal in the field of quantum chaos.

2.2 Time-reversal invariance

In classical mechanics the operation of time-reversal T is defined as

$$t \overset{T}{\mapsto} -t, \quad \mathbf{x} \overset{T}{\mapsto} \mathbf{x}\,, \tag{2.1}$$

where t denotes the time and $\mathbf{x}$ is the position of a particle with mass m. As a consequence, momenta $\mathbf{p} = m\,\mathrm{d}\mathbf{x}/\mathrm{d}t$ and angular momenta $\mathbf{L} = \mathbf{x}\times\mathbf{p}$ change their signs under T, i.e. motions are reversed. Newton's law of motion is a second order differential equation in t, it therefore remains unchanged under application of T. In classical electrodynamics, electromagnetic fields are described by Maxwell's equations. In this case, time-reversal implies

$$t \overset{T}{\mapsto} -t, \quad \mathbf{B} \overset{T}{\mapsto} -\mathbf{B}, \quad \mathbf{J} \overset{T}{\mapsto} -\mathbf{J}\,, \tag{2.2}$$

since the currents $\mathbf{J}$ and the magnetic fields $\mathbf{B}$ are microscopically produced by electrons in motion, whose directions are reversed by T. Under these transformations Maxwell's equations remain unchanged [23].

The time-dependent Schrödinger equation

$$\left(-\frac{\hbar^2}{2\,m}\Delta + V(\mathbf{r})\right)\,\Psi(\mathbf{r},t) = i\,\hbar\frac{\partial\,\Psi(\mathbf{r},t)}{\partial\,t} \tag{2.3}$$

with the solution $\Psi(\mathbf{r},t)$ is not invariant under $t \mapsto -t$. An additional complex conjugation of the solution $\Psi(\mathbf{r},t) \mapsto \Psi^*(\mathbf{r},-t)$ is required to satisfy the time-reversed version of Eq. (2.3). It follows that the quantum mechanical time-reversal operator $\hat{\mathcal{T}}$ cannot be unitary but instead has to be antiunitary [23]. Exploiting this structure of $\hat{\mathcal{T}}$, it can be shown that Hamiltonians of time-reversal invariant systems without spin-1/2 interactions can be represented by real and symmetric matrices [57]. This property stays unchanged under orthogonal transformations

$$H' = O\,H\,O^T\,. \tag{2.4}$$

Here, O is an orthogonal matrix, $O\,O^T = 1$. Removing the restriction of time-reversal invariance leads to Hamiltonians that cannot be represented by real matrices any longer. However, they are still Hermitian, a property that is preserved under unitary transformations

$$H' = U\,H\,U^\dagger \tag{2.5}$$

where $U\,U^\dagger = 1$, i.e. U is unitary.

2.3 Random matrix theory

In 1984 Bohigas, Giannoni and Schmit wrote in their seminal paper [13]:

> "Spectra of time-reversal-invariant systems whose classical analogs are K [that is strongly chaotic] systems show the same level fluctuation properties as predicted by GOE..."

This famous conjecture established the close connection between properties of quantum systems whose classical analogs show chaotic dynamics and a part of statistical physics known as random matrix theory (RMT). The objective of RMT is a description of quantum systems based on symmetry considerations and general properties of physical systems alone. It was developed, having the spectra of complex nuclei in mind [58], in the 1950s and 1960s by Wigner, Dyson and Mehta. An exhaustive review of the development and applications of RMT can be found in Ref. [59].

In RMT the information content of the Hamiltonian is restricted to the symmetry considerations of Eq. (2.4) and Eq. (2.5). Taking these into account, RMT leads to ensembles of matrices [59] with probability distributions $\mathcal{P}_{N\beta}(H) \propto \exp(-\beta \operatorname{tr} H^2)$, where the Hamiltonian H is represented as a $N \times N$ matrix. For physical systems the limit $N \to \infty$ has to be considered. The parameter β depends on the considered symmetry class: for time-reversal invariant systems $\beta = 1$ defines the Gaussian orthogonal ensemble (GOE); for time-reversal non-invariant systems $\beta = 2$ represents the Gaussian unitary ensemble (GUE). The case $\beta = 4$, the Gaussian symplectic ensemble (GSE) of interacting spin-1/2 particles, is mentioned for completeness but is not of further interest for the present work.

Diagonalization of H taken from the GOE directly leads to predictions on the spectral properties of chaotic, $\mathcal{T}$ invariant quantum systems. These properties describe the mean spacing of the eigenvalues, the fluctuations of the distances between adjacent eigenvalues about this mean ("spectral fluctuations") and the correlations between such distances [58]. The predictions have been confirmed in numerous experiments [17–19, 60, 61]. In this way, the conjecture by Bohigas, Giannoni and Schmit has been corroborated.

2.4 Nuclear physics and scattering formalism

In nuclear physics much insight is gained by performing nuclear reaction experiments using particle accelerators. The principle of these experiments can be described as a three-step process. In a first step an accelerated particle is moving toward the reaction target. Ideally all quantum numbers (spin, parity, momentum, etc.) are known. This set of numbers labels the incident channel. In a second step the particle hits the target, that is, it interacts locally with some potential which might cause some of the quantum numbers to change. In the third and final step a particle leaves the interaction region to be registered by some detector system that determines the new set of quantum numbers which now labels the final channel. This whole process defines a scattering problem where the fundamental challenge is to determine the transition probability from a given initial channel to a given final channel.

In quantum mechanics this process of scattering is described in terms of a scattering matrix S. Its elements are defined by

$$S_{fi} := \langle \Psi_f | S | \Psi_i \rangle \,, \tag{2.6}$$

with $|\Psi_i\rangle$ and $|\Psi_f\rangle$ being the initial and final states, respectively. The connection between the Hamiltonian H of the system and the scattering matrix S is elaborated by Mahaux and Weidenmüller within the framework of compound nucleus reactions in Ref. [43] as

$$S(E) = 1 - 2\pi i \, W^\dagger (E - H^{\text{eff}})^{-1} W \,, \tag{2.7}$$

with W as the coupling between the internal Hamiltonian H and the scattering channels. The coupling modifies H to become an effective Hamiltonian $H^{\text{eff}} = H - i\pi \, W W^\dagger$ in Eq. (2.7). It should be noted that the scattering matrix is in general a complex valued object and in nuclear physics only the cross section, that is its modulus square, is experimentally accessible.

Equation (2.7) provides the crucial connection between theory and measurement. It links the information of the scattering matrix obtained in experiments to the Hamiltonian which is of interest to theoretical considerations. For quantum systems exhibiting chaotic dynamics the Hamiltonian can be described using

RMT. The couplings W are given parameters of the problem and are often assumed to follow a Gaussian distribution. A possible energy dependence of W is often neglected. Using this universal description of a scattering process, Eq. (2.7) allows for predictions of statistical properties of the scattering matrix.

2.5 Microwave resonators

To probe the statistical properties of quantum systems experimentally is a demanding task. In nuclear physics large accelerator facilities are required in order to measure the scattering properties of nuclei. In these experiments, suitable many-particle descriptions are difficult to obtain, the experimentalist has only few opportunities to influence the properties of the scattering systems and it is difficult to gather consistent data sets large enough for statistically significant results. Nevertheless, such work has been done and good agreement between observed spectra and statistical predictions of the RMT has been found [62–66].

In recent years, another access to quantum systems has become available via quantum dots and other mesoscopic systems. In these custom tailored devices quantum transport properties are readily accessible and of great interest [67]. However, neither in experiments with nuclei nor with mesoscopic devices can the full complex S-matrix be measured.

This is possible, however, in experiments with flat microwave resonators. In these resonators of height d, for excitation frequencies below

$$f_{\max} = \frac{c_0}{2\,d}\,, \tag{2.8}$$

where c_0 is the speed of light, only TM_0 modes can be excited. For these modes the electrical field vector is always perpendicular to the bottom of the resonator. Under these conditions, the Maxwell equations reduce to the scalar Helmholtz equation [68]

$$(\Delta + k^2)\,\varphi(\mathbf{r}) = 0, \quad k = 2\pi\, f/c_0 \tag{2.9}$$

with the boundary condition

$$\varphi(\mathbf{r})|_{\partial\Omega} = 0\,. \tag{2.10}$$

Then, the electric field inside the resonator is $\mathbf{E}(\mathbf{r}) = \varphi(\mathbf{r})\,\mathbf{n}$, where $\mathbf{n}$ is the vector normal to the surface area Ω which is bounded by $\partial\Omega$. Thus the amplitude $\varphi(\mathbf{r})$ of the electric field is formally identical with the wave function $\psi(\mathbf{r})$ obtained from Schrödinger's equation

$$(\Delta + k^2)\,\psi(\mathbf{r}) = 0, \quad k = \sqrt{2\,m\,E}/\hbar \tag{2.11}$$

of a single particle in a billiard potential. Together with the boundary condition

$$\psi(\mathbf{r})|_{\partial\Omega} = 0 \tag{2.12}$$

the complete correspondence between the electromagnetic problem Eqs. (2.9, 2.10) and the quantum mechanical system Eqs. (2.11, 2.12) is established.

A flat microwave resonator is schematically shown in Fig. 2.2. Three high-conductivity copper plates form the resonating cavity. The middle plate defines the shape Ω of the corresponding potential. In order to achieve a high quality factor Q inside the resonator, contact resistances are suppressed by tightly screwing the system together and by applying wires of solder close to the inner contour [69]. This setup allows for Q values between 10^3 and 10^4. While experiments with superconducting niobium cavities [18] achieve quality values up to 10^7, the present work relies on normal conducting resonators as magnetized ferrites are to be inserted into the billiard (see Sec. 3). Small holes (diameter about 2 mm) are drilled into the lid of the resonator through which thin wires (diameter about 0.5 mm) are inserted into the cavity. The wires act as dipole antennas to couple the rf power into and out of the resonator.

A vectorial network analyzer (VNA) produces rf power with adjustable frequency. The VNA is connected to a coaxial line that, in turn, is attached to one antenna. Depending on the excitation frequency, part of the signal delivered by the VNA is reflected back into the coaxial line and another part excites an electromagnetic standing wave pattern. The VNA can either analyze the reflected signal or it can be connected to a second antenna to track the transmitted signal. The VNA compares the emitted and received signal according to amplitude *and* phase. This process yields the complex scattering matrix element. The full S-matrix is obtained by sequential reflection and transmission measurements. This scattering matrix comprises, however, only the observable channels as defined by

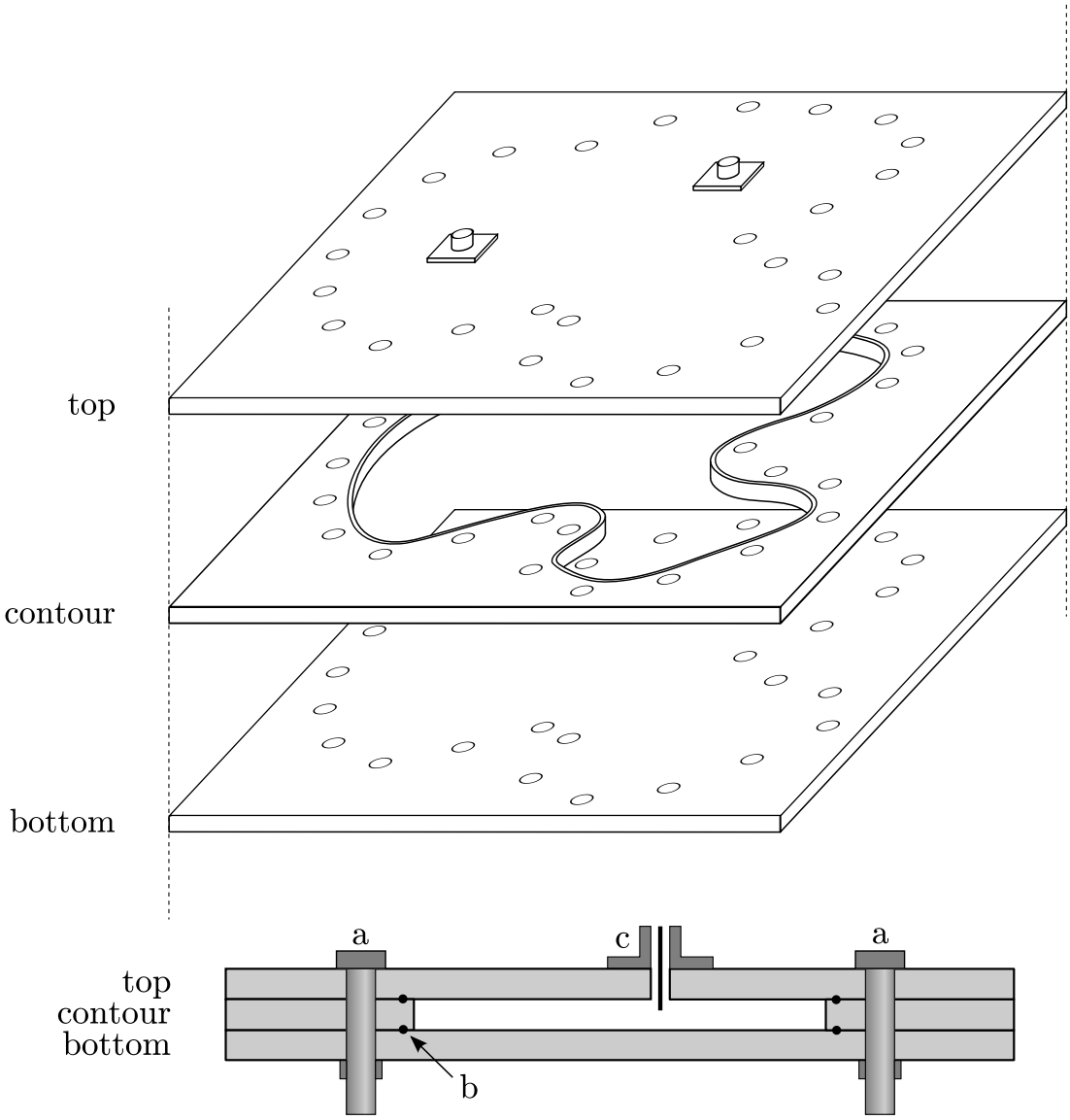

Fig. 2.2: Exploded view (upper figure) and sectional drawing (lower figure) of a modular microwave resonator. Visible are the top, contour and bottom plate, typically made out of copper, 5 mm in thickness. The lateral dimensions of the resonator usually are about 500 mm. The contour plate defines the shape of the billiard. The plates are tightly connected by screws (a) while solder (b) ensures good electrical contact between the three plates. The coupling of rf power into the resonator is achieved by short antennas (c).

the antennas. Dissipative effects due to absorption in the walls of the cavity are observed indirectly, see Sec. 5.3.

3 Induced time-reversal symmetry breaking

In nature, only the weak interaction is known to break time-reversal symmetry (see Sec. 1). Therefore all experiments which do not involve the weak interaction and aim at investigating effects of time-reversal symmetry breaking (TRSB) need to resort to "tricks" in order to induce TRSB in the system of interest. Furthermore, a way to simulate a reversal of time has to be available, if differences between a forward and a backward propagation in time are to be unveiled.

In conductance experiments with mesoscopic devices TRSB is usually achieved by means of an externally applied magnetic field. Electrons transmitted through the structures are confined to circular paths by the Lorentz force. They will not retrace their paths under $\mathcal{T}$ unless the external field is reversed. By keeping it unchanged an induced type of TRSB within the mesoscopic devices can be accomplished. Experimental realizations include the investigations of weak localization effects [51] and universal conductance fluctuations [44]. In acoustics, a simulated reversal of time direction is accomplished by the usage of time-reversal mirrors. They are made of large transducer arrays that sample, time reverse and re-emit acoustic wave fields [70]. Induced TRSB has been demonstrated in rotational flows where the propagation of ultrasound waves displays weak localization [71]. Recently, TRSB observed in superconductors attracted much attention [72–74], where magnetic moments of coupled electron spins induce $\mathcal{T}$ breaking.

Dissipative effects are *not* to be associated with a breaking of $\mathcal{T}$ invariance. While dissipation leads to a distinct time arrow in the macroscopic world, it does not influence the symmetry properties of the Hamiltonian H of a scattering system. In the framework of Eq. (2.7) dissipation is only included in the coupling W, where absorptive channels represent dissipative effects. These channels are not accessible to the experimenter; the measurable S-matrix is sub-unitary while the complete S-matrix remains unitary. However, this does not imply TRSB. If one could keep track of all the energy lost through dissipation and reverse the direction of time, the initial state would be recovered. This only holds for systems where H is $\mathcal{T}$ invariant. In a system with "true" $\mathcal{T}$ breaking even a hypothetical reversal of all final states would not lead back to the initial state.

3.1 Time-reversal in microwave billiards

The most direct way to probe time-reversal symmetry is to reverse the direction of time and to observe the evolution of the system under study—which is of course impossible, as nature has not provided us with a method to reverse time. In classical mechanics, $\mathcal{T}$ corresponds to a reversal of motion and can thus be simulated by negating all velocities at the *end* of the classical paths. In electrodynamics, according to Eq. (2.2), magnetic fields $\mathbf{B}$ and currents $\mathbf{J}$ need to be inverted.

In scattering systems, by definition of Eq. (2.6), the interchange of the initial and the final channel corresponds to a reversal of time. Using Eq. (2.7), it can be shown that for a $\mathcal{T}$ invariant Hamiltonian H, i.e. a real and symmetric H,

$$S_{ab} = S_{ba}, \ a \neq b \tag{3.1}$$

holds. Equation (3.1) yields the definition of *reciprocity*. Taking the modulus square

$$\sigma_{ab} = |S_{ab}|^2 = |S_{ba}|^2 = \sigma_{ba} \tag{3.2}$$

states the weaker condition of *detailed balance* [75] and involves only cross sections, which are experimentally accessible in nuclear physics [38]. While detailed balance only requires the equivalence of the modulus, reciprocity demands the agreement in modulus *and* phase—the former provides a necessary, the latter a sufficient condition for the detection of TRSB.

These observations directly lead to a recipe for the simulation of a reversed time evolution in experiments with microwave resonators: Simply interchange the input and the output channel. A violation of reciprocity will then give direct prove of (induced) $\mathcal{T}$ breaking.

3.2 Ferrites and ferromagnetic resonance

A ferrite is a non-conductive ceramic with a ferrimagnetic crystal structure. As in antiferromagnets, its magnetic moments on different sublattices are opposed and

their magnitudes differ. Thus a spontaneous magnetization remains [76]. Under the influence of a sufficiently strong external magnetic field $\mathbf{H}_{\mathrm{ex}}$—the required strength depends on the saturation magnetization $4\pi\, M_{\mathrm{s}}$ and geometry dependent demagnetization corrections—the individual moments couple to a ferromagnetic order, which can effectively be described as a macroscopic magnetic moment $\mathbf{M}$, see Fig. 3.1.

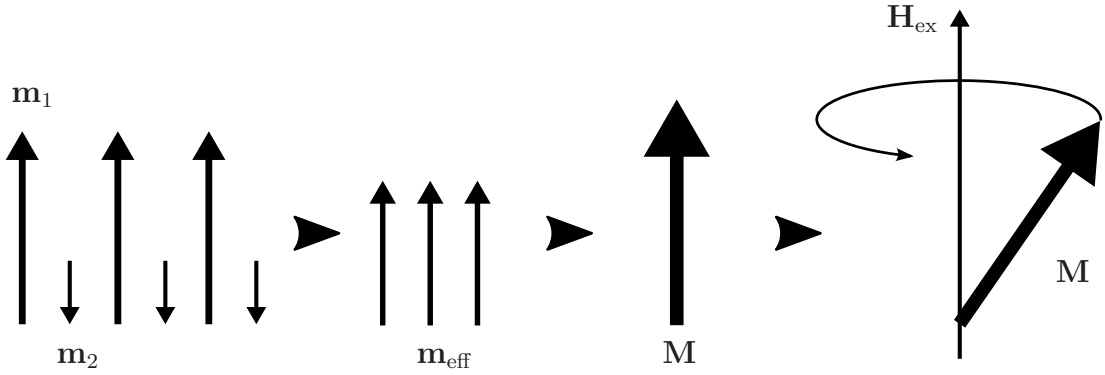

Fig. 3.1: Sketch of the magnetic structure of ferrites in an external magnetic field. Two sublattices have opposed magnetic moments $\mathbf{m}_1, \mathbf{m}_2$. In each crystal cell these couple to a single moment $\mathbf{m}_{\mathrm{eff}}$, thereby behaving like a ferromagnetic structure. In a macroscopic treatment isolated magnetic moments sum up to a macroscopic magnetic moment $\mathbf{M}$ which precesses around the external magnetic field $\mathbf{H}_{\mathrm{ex}}$.

In a classical treatment [77] the field $\mathbf{H}_{\mathrm{ex}}$ exerts on the moment $\mathbf{M}$ an angular momentum of $\mathbf{M} \times \mathbf{H}_{\mathrm{ex}}$. The magnetic moment and the angular momentum $\mathbf{J}$ are connected via $\mathbf{M} = -\gamma\, \mathbf{J}$, with

$$\gamma = g \frac{e}{2\, m_e\, c_0} = g \frac{\mu_B}{\hbar} \approx g \cdot 8.7941 \frac{\mathrm{MHz}}{\mathrm{Oe}} \tag{3.3}$$

being the gyromagnetic ratio. Thus the equation of motion reads

$$\frac{\mathrm{d}\mathbf{J}}{\mathrm{d}t} = \mathbf{M} \times \mathbf{H} \quad \Rightarrow \quad \dot{\mathbf{M}} = -\gamma\, \mathbf{M} \times \mathbf{H}, \tag{3.4}$$

where the internal magnetic field strength $\mathbf{H} = \mathbf{H}(\mathbf{H}_{\mathrm{ex}}, \mathbf{N})$ is a function of $\mathbf{H}_{\mathrm{ex}}$ and a geometry dependent demagnetization factor $\mathbf{N}$. The calculation of $\mathbf{N}$ is only feasible for elliptically shaped ferrites, but not for the cylindrical shapes (diameter 4 mm, height 5 mm, cf. Sec. 3.4) used in the present work. Equation (3.4)

determines the precession with the Larmor frequency $\omega_0 = \gamma\, H$ of $\mathbf{M}$ around the direction of $\mathbf{H}$ (see Fig. 3.1, rightmost figure).

For a further analysis of Eq. (3.4) the time dependence of $\mathbf{H}$ and $\mathbf{M}$ will be described in first order as

$$\mathbf{H}(t) = \mathbf{H}_0 + \mathbf{h}\, e^{i\,\omega\, t}, \quad \mathbf{M}(t) = \mathbf{M}_\mathrm{s} + \mathbf{m}\, e^{i\,\omega\, t}, \tag{3.5}$$

where $\mathbf{H}_0$ denotes a sufficiently large time independent magnetic field to bring the ferrite into its saturation magnetization $\mathbf{M}_\mathrm{s}$ and $\mathbf{h}$ ($\mathbf{m}$) is a perturbation perpendicular to $\mathbf{H}_0$ ($\mathbf{M}_\mathrm{s}$) with angular frequency ω. Taking $\mathbf{H}_0$, $\mathbf{M}_\mathrm{s}$ along the z-axis the dynamical components in Eq. (3.5) are connected by

$$\begin{pmatrix} m_x \\ m_y \\ m_z \end{pmatrix} = \begin{pmatrix} \chi & -i\,\kappa & 0 \\ i\,\kappa & \chi & 0 \\ 0 & 0 & 0 \end{pmatrix} \begin{pmatrix} h_x \\ h_y \\ h_z \end{pmatrix}, \tag{3.6}$$

that is the tensor of magnetic susceptibility. Its components

$$\chi(\omega) = \frac{\omega_0\,\omega_M}{\omega_0^2 - \omega^2}, \quad \kappa(\omega) = \frac{\omega\,\omega_M}{\omega_0^2 - \omega^2}, \quad \omega_0 = \gamma\, H_0, \quad \omega_M = \gamma\, 4\pi M_\mathrm{s} \tag{3.7}$$

display a pronounced resonance behavior and are only non-vanishing close to the so-called *ferromagnetic resonance*. In this treatment effects of damping (which prevent singularities at resonance) have been neglected [78].

3.3 Ferrites in microwave billiards

The idea of induced TRSB always resorts to the introduction of an invariant reference frame into the system that does not change under time-reversal. In experiments using electrons in microstructures an invariant external magnetic field provokes, say, clockwise rotation. A reversal of time is simulated by only reversing the momenta of the electrons. Accordingly, in a $\mathcal{T}$ invariant system they would now move counterclockwise. However, due to the unchanged magnetic field they are still going around in a clockwise fashion—time-reversal symmetry

is broken in an induced way. In acoustics, the invariant reference frame can be established by a rotational flow of the transport medium [71].

In experiments with microwave billiards the propagation of electromagnetic waves has to be influenced in a non-reciprocal manner. Again, this is done by the introduction of a reference frame, the precession of magnetic moments interacting with the magnetic field component of the electromagnetic wave inside the resonator. This is achieved by means of magnetized ferrites. In order to understand the connection to the ferromagnetic resonance, it should first be recalled from Sec. 2.5 that for excitation frequencies below $f_{\max}$ only TM_0 modes propagate inside the resonator. Therefore, if a ferrite inside the microwave billiard is magnetized perpendicular to the bottom of the resonator, the rf magnetic fields are perpendicular to the magnetization field, $\mathbf{h} \perp \mathbf{H}_0$, and the conditions Eq. (3.5) are met.

It is instructive to separate the electromagnetic fields into circularly polarized ones which leads to $\chi_\pm = \chi \pm \kappa$ and $m_\pm = \chi_\pm h_\pm$. The resonance condition now reads as

$$\chi_\pm(\omega) = \frac{\omega_M}{\omega_0 \mp \omega}\,. \tag{3.8}$$

This expresses the $\mathcal{T}$ breaking properties of the ferromagnetic resonance with respect to circularly polarized magnetic rf fields; the susceptibility changes and the resonating structure is only visible for the "+" direction of polarization. Damping effects lead to complex valued contributions to Eq. (3.8) describing an exponential attenuation of the rf fields at resonance [78]. In the Landau-Lifshitz form [77] losses are attributed to a relaxation time T, resulting in a finite linewidth $\Delta H = 2/(\gamma T)$ of the ferromagnetic resonance and the magnetic susceptibility

$$\chi_\pm(\omega) = \frac{\omega_M}{(\omega_0 + i/T) \mp \omega}\,, \tag{3.9}$$

is a complex quantity. Inside the microwave billiard every rf magnetic field can be decomposed into circularly polarized fields of, in general, unequal magnitudes. Due to the complex susceptibility the ferrite strongly damps one of these components while leaving the other nearly unaffected. A simulated reversal of time, as described in Sec. 3.1, leads to an interchange of the magnitudes, thus changing the net effect of the ferrite on the rf electromagnetic field and inducing TRSB.

3.4 Ferrite in a waveguide

In the following, all experiments involving ferrites utilize calcium vanadium garnets, type "CV19"[2]. These exhibit a saturation magnetization $4\pi\, M_{\mathrm{s}} = 1859$ Oe, a dielectric constant $\varepsilon = 14.6$ and a resonance linewidth $\Delta\, H_{-3\ \mathrm{dB}} = 17.5$ Oe. The samples used were of cylindrical shape, each 5 mm in height and with diameters varying between 4 and 10 mm in steps of 2 mm.

Waveguides are an ideal tool to investigate the TRSB effect of ferrites. Over a broad frequency range a nearly uniform level of energy, transmitted in a mode of single circular magnetic polarization, allows for a detailed study of time direction dependent absorptive properties. This has been done thoroughly in Ref. [79]. The results for the ferrite 4 mm in diameter, which is of special interest in the following experiments, are shown in Fig. 3.2. A linear dependence of the fer-

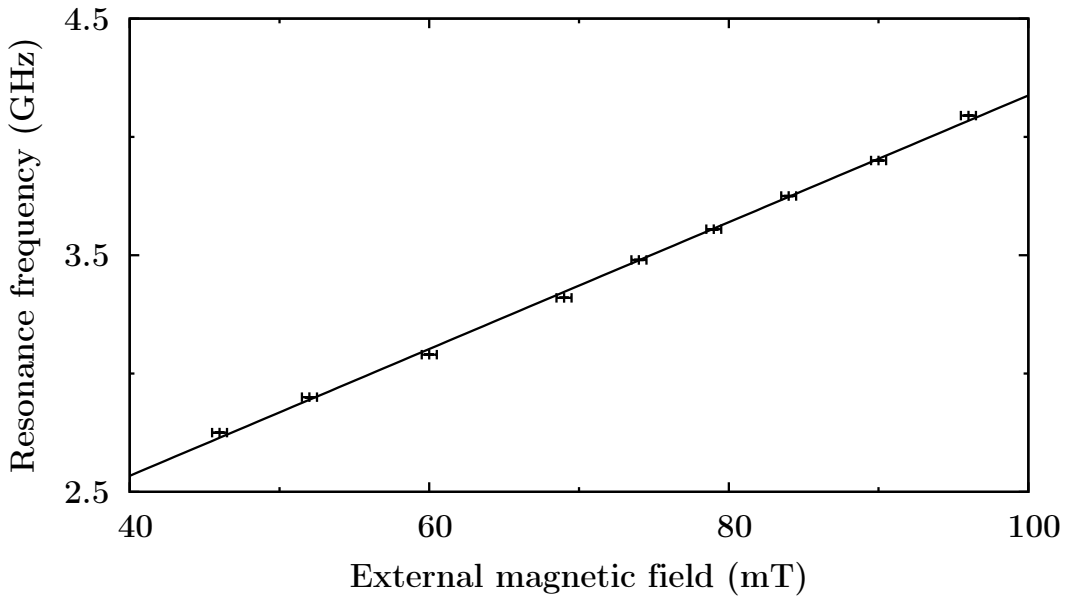

Fig. 3.2: Dependence of ferromagnetic resonance on magnetic field strength B. The data points were taken using a 4 mm diameter CV19 ferrite. The error bars account for a uncertainty of ± 0.5 mT in the determination of B at the center of the ferrite, the error in the resonance frequencies is less than the symbol size. (Based on Ref. [79].)

[2]Courtesy of AFT MATERIALS GmbH, Spinnerei 44, 71522 Backnang, Germany

romagnetic resonance frequency f on the external magnetic field strength B is nicely confirmed. A linear fit to the data yields [79]

$$f(B) = (0.0268 \pm 0.0004)\frac{\text{GHz}}{\text{mT}}\, B + (1.50 \pm 0.03)\ \text{GHz}\,. \tag{3.10}$$

In the light of Eq. (3.7) this linear dependence might seem to be imperative. However, Eq. (3.7) deals with magnetic fields *inside* the ferrite. A conversion between external and intrinsic fields has to take effects of demagnetization into account. It is due to the rotational symmetry of the ferrite cylinder that the linearity between magnetic field strength and ferromagnetic resonance persists [76].

4 Isolated resonances

The most simple resonating systems comprise only an isolated resonance (singlet) or two nearly degenerate resonances (doublet). In experiments with quantum billiards these also constitute, according to Eq. (2.7), the most basic scattering experiments. It is instructive to study the effects of induced time-reversal symmetry breaking on these. This section to a large extend follows the discussion outlined in Ref. [39] and establishes that two-state systems are the simplest ones to show effects of TRSB. In that respect these experiments differ from the situation in compound nucleus reactions. As has been pointed out in Ref. [37], in differential cross sections of reactions proceeding via isolated resonances a violation of detailed balance is possible due to interference effects in the channels of the final states. Coaxial cables normally allow only for single-mode propagation and thus suppress this mechanism. Due to the simple structure of the S-matrix model describing doublets in microwave resonators it is possible to recover the complete information about the effective Hamiltonian and to link this to the properties of the magnetized ferrite.

4.1 Experimental setup

The setup must be designed such that first the spectrum contains isolated resonances as well as pairs of nearly degenerate ones, and that second a violation of $\mathcal{T}$ invariance is accomplished.

A resonator of circular shape can be used to investigate both, isolated and nearly degenerate resonances. A scheme of the setup is shown in Fig. 4.1, a photograph of the actual cavity is reproduced in Fig. 4.2. The circular resonator is constructed from plates of copper, has a diameter of 250 mm and a height of 5 mm. In the two-dimensional regime the corresponding Helmholtz equation, Eq. (2.9), yields an analytic result. It depends on two quantum numbers; the radial quantum number $n = 1, 2, 3, \ldots$ and the azimuthal quantum number $m = 0, 1, 2, \ldots$. For every $m > 0$ the solutions are doubly degenerate. In a real experiment this degeneracy is lifted by inevitable deviations from the circular

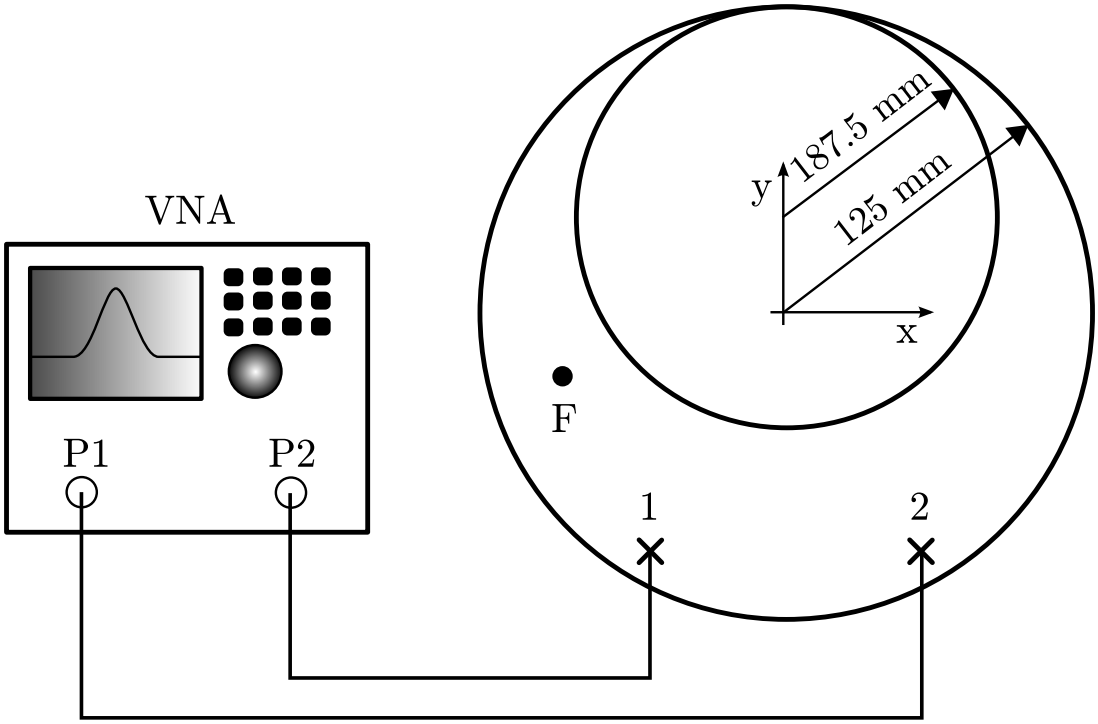

Fig. 4.1: Scheme of the experimental setup (not to scale). The antennas 1 and 2 connected to the vector network analyzer (VNA) are located at $(x, y) = (\pm 78.5 \text{ mm}, -83.5 \text{ mm})$, the ferrite cylinder is placed at the position $(x, y) = (-100 \text{ mm}, -30 \text{ mm})$. For the investigation of isolated singlets the inner circle, a copper disk, is included in the setup to transform the circular into an annular billiard.

shape as introduced, e.g., by a ferrite. This leads to pairs of nearly degenerate resonances. The introduction of an additional inner conducting disk (187.5 mm in diameter, see Fig. 4.1) that touches the boundary of the circular resonator, can be interpreted as going from small deviations to big distortions. In the resulting fully chaotic annular billiard [80–82] all degeneracies are suppressed in the lowest excitations. The result is a picket fence like structure of isolated resonances for these lowest lying modes. The results of the experiments on the annular billiard have already been treated in Ref. [79] and are for completeness recapitulated in Sec. 4.2.

In the preceding discussion in Sec. 3.3 it has been shown that, theoretically, magnetized ferrites should be able to break time-reversal symmetry. Numerous works already have established those TRSB effects in microwave billiards [20, 21,

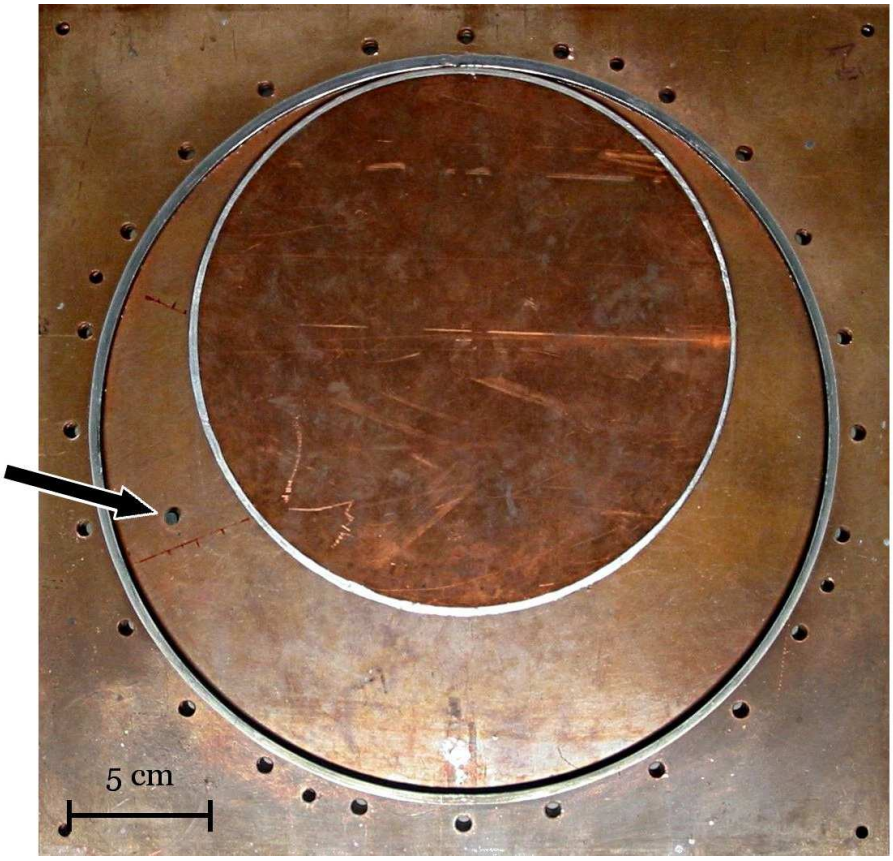

Fig. 4.2: Photograph of the annular billiard. Shown is the center plate defining the contour of the resonator (a circle) together with the asymmetrically placed disk required for the annular setup. Additionally, part of the bottom plate is visible. The arrow points to the ferrite. Also visible are the rings of solder close to the boundaries to ensure good electrical connections between the plates. For the measurements an additional top plate, which includes the antennas, is placed atop this setup and secured in place by screws through the numerous holes visible.

83, 84], confirming changes in the eigenvalue and -vector statistics, as well as influences on transport properties. In the present experiments a ferrite (4 mm in diameter, see Sec. 3.4 for a discussion of its properties) is placed asymmetrically inside the resonator (cf. Figs. 4.1 and 4.2). The required static magnetic field is provided by strong cylindrical NdFeB magnets (20 mm in diameter, 5 mm or 10 mm in height, depending on the desired field strength). They are placed at the position of the ferrite, either on only one side or on both sides outside the cavity. Attached screw threads allow an adjustment of the distance between the magnets

and the surface of the resonator to within about 50 μm and thereby the fine tuning of the field strength. A scheme of the setup is shown in Fig. 4.3. Accordingly, magnetic field strengths of up to 360 mT (with uncertainties below 0.5 %) are obtained at the vertical center position of the ferrite inside the cavity. The large diameter of the magnets (20 mm) ensures a homogeneous magnetization of the ferrite across its cross section (4 mm in diameter). However, a relative variation of the magnetic field strength of about 3 % with two opposing magnets and of up to 45 % with a single magnet installed is inevitable. This variation of field strength leads to a broadening of the ferromagnetic resonance. By this, a reduced TRSB effect is probable that, however, covers a larger frequency range. The measurements were performed using an HP 8510C VNA. It was connected to the billiard with two coaxial cables of semi-rigid type; the outer conductor of these is made out of solid copper. The cables provide high phase and amplitude stability and are still flexible enough to allow for reasonably easy installation.

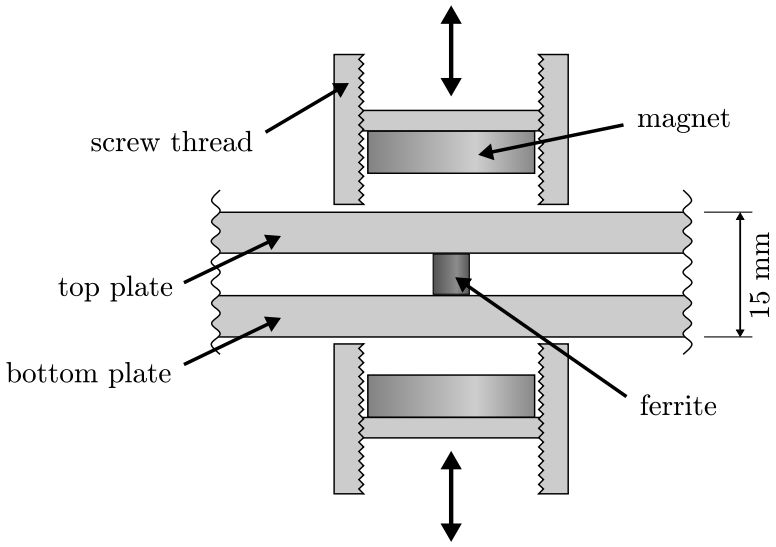

Fig. 4.3: Sectional drawing of the setup for the magnetization of the ferrite. The ferrite is positioned between the top and bottom plate inside the resonator. At its position two NdFeB magnets are placed outside the cavity. Each is held in place by a screw thread mechanism. The threads allow to vary the distance between the magnets and the ferrite.

4.2 Measurement results

A transmission spectrum of the annular billiard without a ferrite is shown in Fig. 4.4. Due to its chaotic dynamics degeneracies are suppressed. Up to 4.7 GHz the 8 lowest lying modes are separated by 250 MHz to 300 MHz. Their widths[3] range from 12 MHz (the first resonance) to 46 MHz (the fifth resonance). The mutual separation of at least 5 level widths justifies a treatment as isolated resonances.

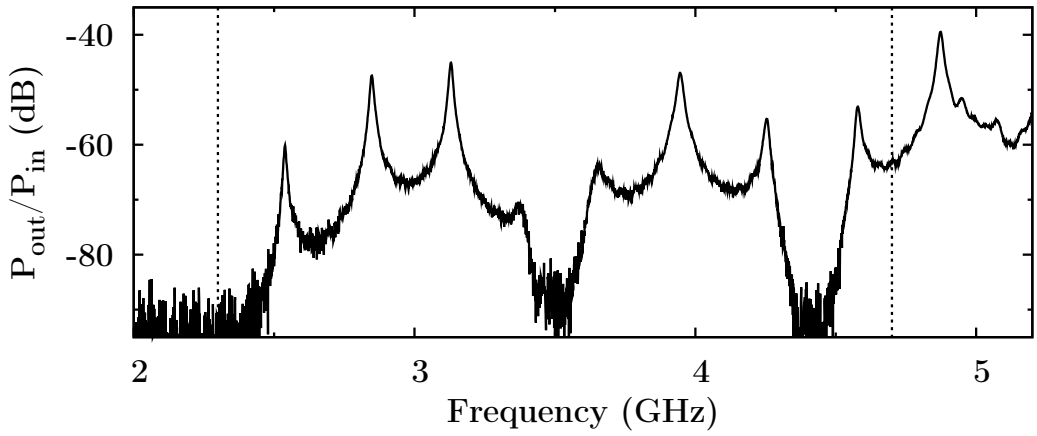

Fig. 4.4: Transmission spectrum of empty annular billiard: The ground state is at 2.54 GHz. The 8 modes between the dashed lines are separated from each other by at least 5 resonance widths and are therefore considered as being isolated singlets. (Based on Ref. [79].)

The insertion of a magnetized ferrite (see Sec. 4.1) induces TRSB. For a variety of magnetic field strengths between 28.5 mT and 119.3 mT the complex scattering matrix elements S_{12} and S_{21} are measured. In all measurements these two reciprocal spectra agree within 0.5 % in amplitude and phase, which is consistent with the principle of reciprocity. A representative pair of spectra is shown in Fig. 4.5.

Removing the inner copper disk leads to a circular billiard whose twofold degeneracies are partly lifted by the presence of the ferrite. This way the effect

[3]The width Γ of a resonance is defined as the full width at half maximum (FWHM), i.e. the broadness of the resonance (plotted as $|S_{ab}|$) at half its maximum value.

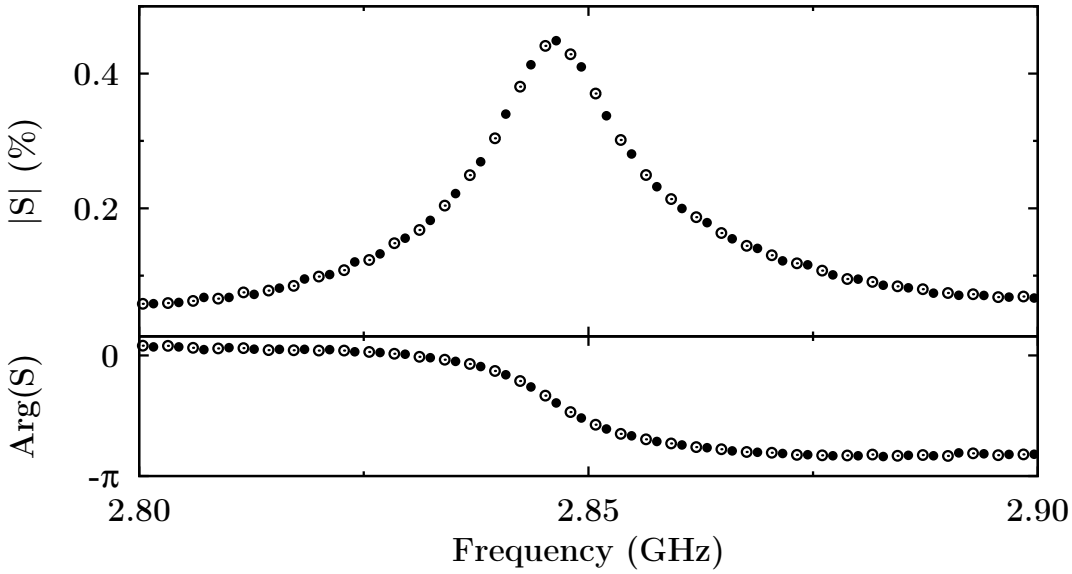

Fig. 4.5: Transmission spectra of the second singlet at 2.846 GHz in the fully chaotic annular billiard: S_{12} (open circles) and S_{21} (solid circles) are shown for an external field of 119.3 mT. Both amplitudes and phases coincide perfectly and reciprocity holds. The statistical errors of the data are smaller than the symbols. (Based on Ref. [39].)

of the ferrite on four isolated doublets at 2.43 GHz, 2.67 GHz, 2.89 GHz and 3.20 GHz has been studied. All measurements between 0 mT and 80.1 mT encompass the complete two channel S-matrix, consisting of $S_{11}, S_{12}, S_{21}, S_{22}$. The VNA has been carefully calibrated to remove any unwanted influences of the connecting cables and connectors. The influence of the ferrite on the resonance shape of the second doublet at 2.67 GHz is illustrated in Fig. 4.6. While in the case of singlets, the transmission did not depend on its direction, it is now of importance and influences the shape of the resonances and reciprocity is violated.

A violation of reciprocity is observed for the first to third doublet, but not for the fourth at 3.20 GHz. This seemingly contradicting behavior is explained by the distribution of the magnetic rf field inside the resonator. Using the software package *CST Microwave Studio* the electromagnetic field pattern was calculated in Ref. [79]. It was discovered that for the fourth doublet at the position of the ferrite the rf magnetic field of one of the two modes has a nodal line. The magnetic field vanishes at this position and the ferrite interacts only with one of the two

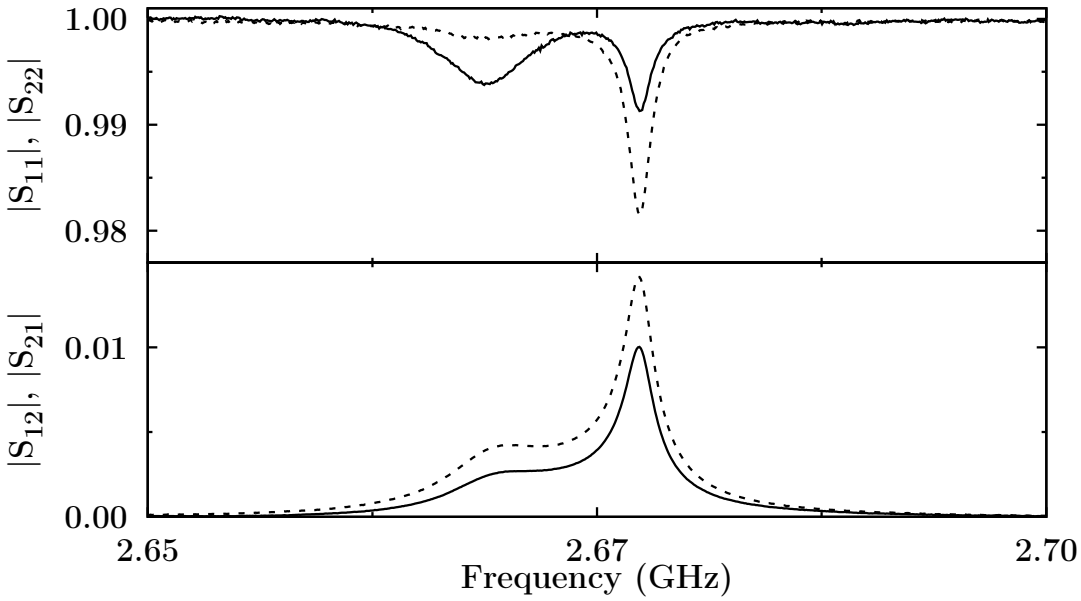

Fig. 4.6: The doublet at 2.67 GHz in the circular billiard with an external magnetic field of 36.0 mT. The upper part shows the absolute values of S_{11} (solid) and S_{22} (dashed), the lower one those of S_{12} (solid) and S_{21} (dashed) with uncertainties of about $5 \cdot 10^{-4}$. Reciprocity is violated. (Based on Ref. [39].)

modes. As a consequence, the fourth doublet-system behaves with respect to its response to TRSB effectively like a singlet case—where no violation of reciprocity can be observed. To check this explanation, the ferrite has been moved radially to $(x, y) = (-90\text{ mm}, -10\text{ mm})$ where, according to the simulation, it should be able to interact with both modes. Indeed, this results in a violation of reciprocity [79].

4.3 Analysis

The starting point to the understanding of the experiments presented above is the scattering matrix approach as formulated by Mahaux and Weidenmüller, given in Eq. (2.7). Adopted to the problem at hand it reads

$$S_{ab}(\omega) = \delta_{ab} - 2\pi\, i\, \langle a|W^\dagger\, (\omega - H^{\text{eff}})^{-1}\, W|b\rangle\,. \tag{4.1}$$

Here, $\omega/(2\pi)$ is the frequency of the rf field. In the case of singlets the effective Hamiltonian H^{eff} is one-dimensional, just a single complex number, say h. The matrix W describes the coupling of the waves in the coaxial cables ($|a\rangle, |b\rangle$) with the resonator singlet state $|1\rangle$. In this case W is a vector of length two and can be represented by

$$W|a\rangle = w_a\,, \quad W|b\rangle = w_b\,, \tag{4.2}$$

where $w_{a,b}$ are complex numbers. Using this notation Eq. (4.1) reduces to

$$S_{ab}(\omega) = \delta_{ab} - 2\pi\, i\, \frac{w_a^*\, w_b}{\omega - h}\,. \tag{4.3}$$

From this expression it is evident that, no matter the value of h, reciprocity holds as long as $w_{a,b}^* = w_{a,b}$, i.e. the coupling of the antennas is real valued. As the experimental results on the influence of TRSB on singlets indeed show no violation of reciprocity, it can be concluded that the coupling to the leads is real and therefore $\mathcal{T}$ invariant. This was to be expected as the coupling is realized by antennas consisting of simple metallic wires whose properties should not depend on the direction of time.

In the case of a doublet H^{eff} has dimension two. Because the coupling W connects two resonator states $|1\rangle$ and $|2\rangle$ with the waves in the two coaxial cables, it is a 2×2 matrix. Since the coupling is $\mathcal{T}$ invariant, W can be chosen real. One viable parametrization of W in terms of four real parameters is

$$W|a\rangle = N_a \begin{pmatrix} \cos\alpha \\ \sin\alpha \end{pmatrix}, \quad W|b\rangle = N_b \begin{pmatrix} \cos\beta \\ \sin\beta \end{pmatrix}\,. \tag{4.4}$$

To gain access to the $\mathcal{T}$ breaking properties of the effective Hamiltonian, it is decomposed into two parts, a symmetric and an antisymmetric component

$$H^{\text{eff}} = H^s + i\, H^a = \begin{pmatrix} H_{11}^s & H_{12}^s \\ H_{12}^s & H_{22}^s \end{pmatrix} + i \begin{pmatrix} 0 & H_{12}^a \\ -H_{12}^a & 0 \end{pmatrix}\,, \tag{4.5}$$

whose matrix elements are complex valued. This is because H^{eff} is not Hermitian; it includes losses. The factor i in front of H^a is by convention [85]. Of these two matrices only H^a breaks $\mathcal{T}$ invariance. (One again sees that TRSB cannot be observed for a singlet—the antisymmetric component vanishes.) The value of

H^a_{12} does not depend on the choice of the resonator basis states $|1\rangle, |2\rangle$, because H^a is invariant under orthogonal transformations.

The determination and connection of H^a_{12} to the ferromagnetic resonance is the main objective of the following analysis. For the estimation of H^a_{12}, Eq. (4.1) is expressed in terms of Eq. (4.4). This model is then fitted to the measured two-dimensional S-matrix. The fit adjusts the parameters of the problem to the data for all investigated magnetic field strengths. The problem includes 4 real $(N_a, N_b, \alpha, \beta)$ and 4 complex (the components of H^{eff}) parameters. Of these, the real ones describing the coupling W are considered to be, in first order, independent of the external magnetic field. This assumption holds if the resonator mode structure at the position of the antennas is independent of the external magnetic field. To get a consistent set of the field independent parameters N_a, N_b, α, β, the fit has to take the measured spectra for all S-matrix elements and for all strengths of the magnetic field *simultaneously* into account. Application of Eq. (4.5) then yields the $\mathcal{T}$ breaking matrix element, H^a_{12}, itself.

However, for a quantitative understanding of the degree of TRSB the value of H^a_{12} by itself is not an appropriate measure. It has to be compared to the spacing of the diagonal elements of H^s, in close analogy to the definition of symmetry breaking strengths in Refs. [86–90], a concept which will further be exploited in Sec. 6. A suitably adapted definition of a TRSB strength is

$$\xi = \left| \frac{2\, H^a_{12}}{H^s_{11} - H^s_{22}} \right| \tag{4.6}$$

which describes the physically relevant effect of H^a_{12}. Even a large $\mathcal{T}$ breaking matrix element would have no measurable impact if the resonances were to be too far apart, a situation similar to that of singlets where no TRSB is detectable. Full TRSB is expected to set in already for $\xi \approx 1$, where the modulus of H^a_{12} is in the order of the level spacing [88]. For the second and third doublets the respective values of H^a_{12} and ξ are shown in Fig. 4.7. Note the resonance like structure of H^a_{12} in modulus *and* phase; while the modulus goes, as a function of the external magnetic field, through a maximum the phase drops by about π. This is reminiscent of the structure of the ferromagnetic resonance.

Even though the experiments presented here are interpreted using principles based on quantum mechanics, the basic physics still is the interaction between

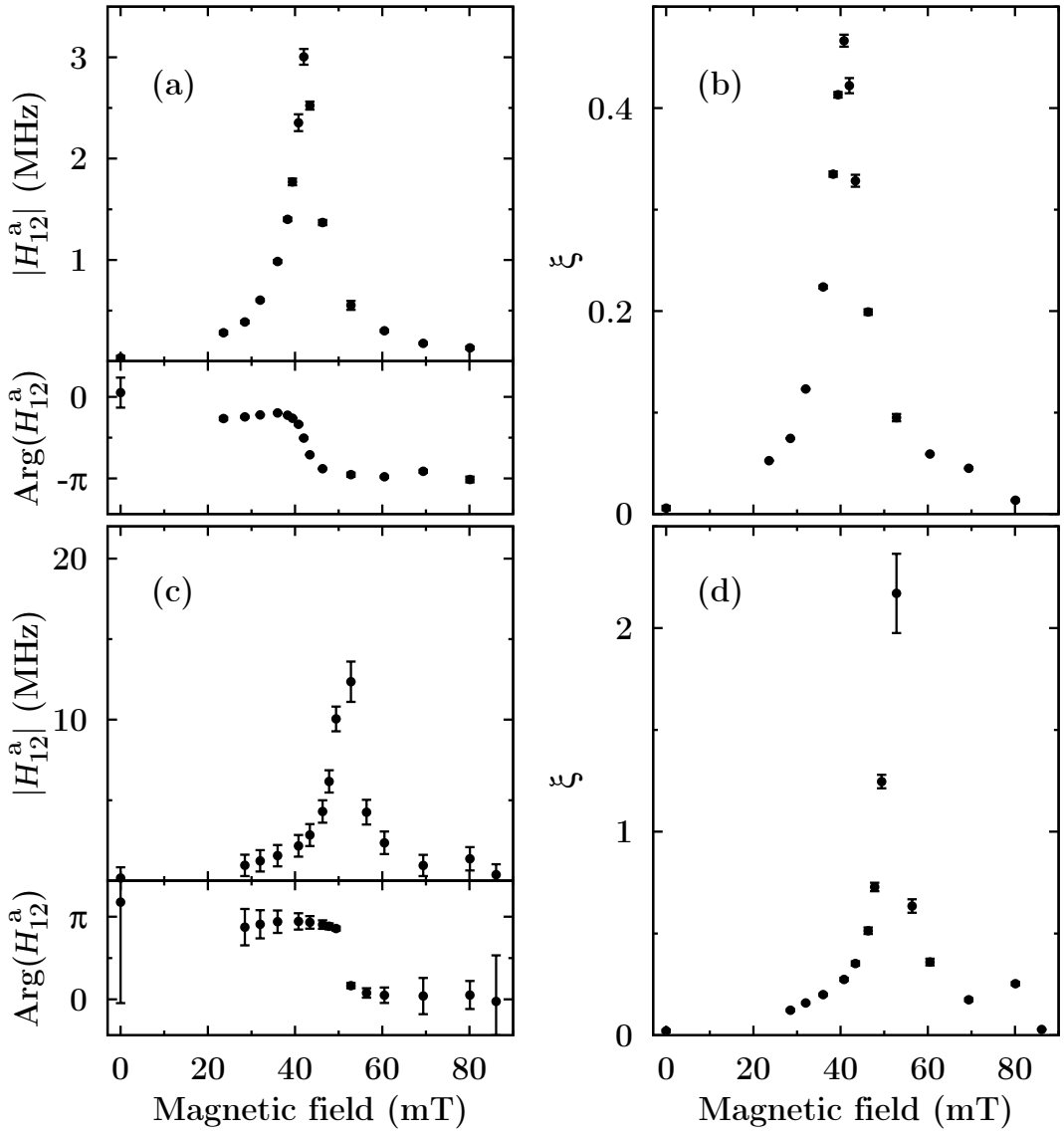

Fig. 4.7: The $\mathcal{T}$ violating matrix element H_{12}^a and the TRSB strength ξ for the second and third doublet at 2.67 GHz and 2.89 GHz, respectively. The upper panels display H_{12}^a in modulus and phase (a) and ξ in (b) for the second doublet. The lower panels (c) and (d) include the same information on the third doublet. The error bars indicate the variations of the results obtained by five independent executions of the experiment.

electromagnetic rf fields and precessing spins of a magnetized ferrite. Accordingly, an understanding of the results obtained for H_{12}^a based on the properties of the ferrite and its magnetization is desirable. As the ferrite couples only to one of two possible circular polarizations of the rf magnetic field (see Sec. 3.3), a reasonable

approach to model the effect of the ferrite is a change of the basis. The unitary matrix

$$U = \frac{1}{\sqrt{2}} \begin{pmatrix} 1 & -i \\ 1 & i \end{pmatrix} \tag{4.7}$$

transforms the two real resonator modes ($|1\rangle$, $|2\rangle$) into circularly polarized ones. In this basis the modes couple to three channels: the two antenna channels and a further one modeling the interaction with the small ferrite. The latter couples to only one of the two circular polarized modes, thereby inducing TRSB. Hence, the effective Hamiltonian in the original basis $|1\rangle$ and $|2\rangle$ is, based on Eq. (4.2.20b) of Ref. [43],

$$H^{\text{eff}}_{\mu\nu} = W_{\mu\nu} + \sum_{i=a,b,f} \int_{-\infty}^{\infty} \mathrm{d}\omega' \frac{W_{\mu i}(\omega') W^*_{\nu i}(\omega')}{\bar{\omega}^+ - \omega'} \,. \tag{4.8}$$

Here, the first term, $W_{\mu\nu}$ with $\{\mu, \nu\} \in \{1, 2\}$, describes the internal dynamics of the closed system without ferrite. The second one accounts for the coupling of the resonator modes to the antennas a and b and to the ferrite channel f, each with its respective coupling strength. The angular frequency $\bar{\omega}$ is infinitesimally shifted to positive complex values, so that $\bar{\omega}^+ = \bar{\omega} + i\,\epsilon,\ \epsilon > 0$.

In order to model the coupling $W_{\xi f}$ to the ferrite, the transformation to the circular basis with new couplings $\tilde{W}_{\xi f}$ introduced via

$$W_{\nu f}(\omega') = \sum_{\xi=1}^{2} U^*_{\xi\nu} \tilde{W}_{\xi f}(\omega') \tag{4.9}$$

is performed. According to the assumption of no coupling of the ferrite to one of the circular states, one of the $\tilde{W}_{\xi f}$ vanishes, say $\tilde{W}_{2f} = 0$. For the other coupling $\tilde{W}_{1f}$ a behavior proportional to the magnetic susceptibility (see Sec. 3.3)

$$\tilde{W}_{1f}(\omega') \propto \chi(\omega') = \frac{\omega_M}{\omega_0(B) - \omega' - i/T} \,, \tag{4.10}$$

is expected. Evaluation of Eqs. (4.7)–(4.10) finally leads to

$$H^a_{12}(B) = \frac{\pi}{2}\, \zeta\, B\, T\, \frac{\omega_M^2}{\omega_0(B) - \bar{\omega} - i/T} \,, \tag{4.11}$$

where the proportionality in Eq. (4.10) is expressed in terms of $\zeta\, B$. Here, the parameter ζ fixes the absolute coupling strength of the ferrite to the magnetic

rf field at its position and $\bar{\omega}$ is—while the ferromagnetic resonance is swept over the doublet by a varied external magnetic field—the resonance frequency of the TRSB effect. The relaxation time T, the angular frequency $\omega_M = \gamma\, 4\pi M_\mathrm{s}$ and the ferromagnetic resonance $\omega_0(B)$ as a function of the external field are known, see Sec. 3.4. The details of the derivation are given in Appendix A.

The model as presented here is valid for completely saturated ferrites only. For low magnetization field strengths a broadening of the resonance line shape in Eq. (4.10) due to the formation of domains of different magnetization inside the ferrite is likely. This broadening effect can be accounted for by a convolution

$$\tilde{H}^a_{12}(B) = \int_{-\infty}^{\infty} \mathrm{d}\omega'\, H^a_{12}(\omega')\, \Psi(\omega_0(B) - \omega')\,, \tag{4.12}$$

of the result Eq. (4.11) with a Gaussian distribution

$$\Psi(\omega) = \frac{e^{i\alpha}}{\sqrt{2\pi}\,\sigma}\, e^{-\frac{1}{2}(\omega/\sigma)^2}\,, \tag{4.13}$$

defined by a width σ and an additional phase contribution α.

The final model has four unknown parameters: σ, $\bar{\omega}$, ζ and α. They need to be determined from the experimentally obtained data for H^a_{12} by a fit. The values of the fitted parameters for the first three doublets are listed in Tab. 4.1. The results for the second and third doublet in the circular billiard are shown in Fig. 4.8. The data for the first doublet closely resemble those for the second doublet, shown here, and are equally well described by the model.

Tab. 4.1: Parameters of Eq. (4.12) for the first three doublets. The third doublet is not convoluted, hence σ and α are not defined in this case. (Based on Ref. [39].)

#	σ (Oe)	$\bar{\omega}/2\pi$ (GHz)	ζ (mT^{-1})	α (deg)
1	42.1 ± 9.3	2.427 ± 0.037	35.7 ± 4.6	-5 ± 8
2	15.5 ± 3.3	2.696 ± 0.011	10.8 ± 1.0	168 ± 7
3	$\cdots$	2.914 ± 0.003	37.3 ± 1.6	$\cdots$

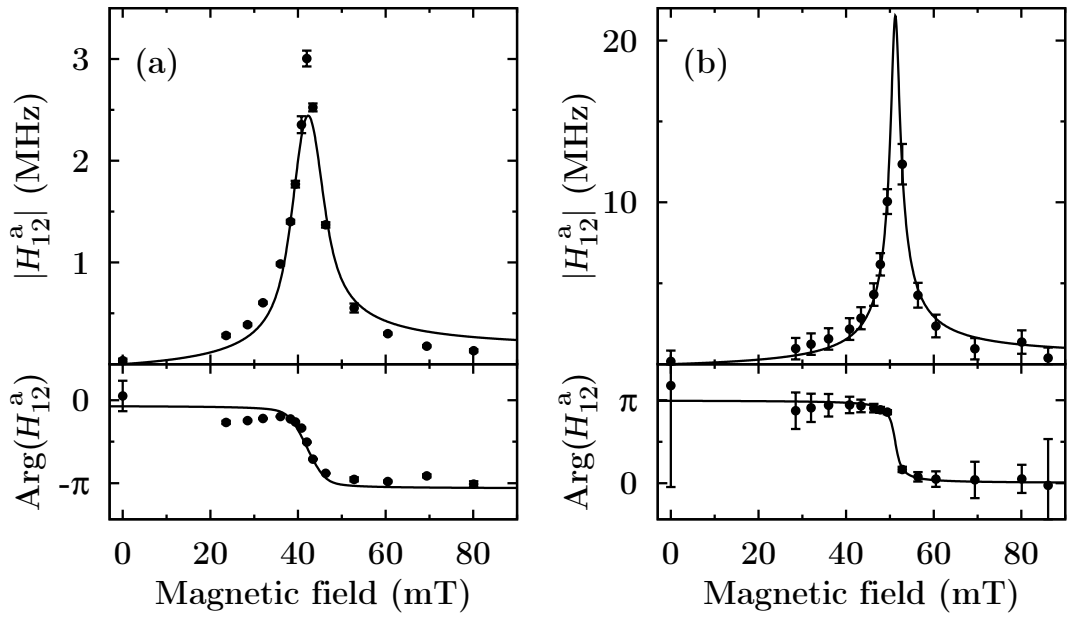

Fig. 4.8: Comparison of the experimentally determined H_{12}^a to the model description Eq. (4.11). A convolution, see Eq. (4.12), accounts for a magnetization distribution of width 15.5 Oe and reproduces the data for the second doublet (a) with good agreement. A direct application of the model without convolution is possible for the third doublet (b), as the higher external magnetic fields allow for a more homogeneous magnetization of the ferrite. For the error bars see the caption of Fig. 4.7. (Based on Ref. [39].)

An overall convincing agreement between the model and the data is found. Deviations are largest close to resonance where the magnetic susceptibility varies considerably over the frequency range of the doublet. The model cannot take these variations into account as it assumes a fixed degree of time-reversal symmetry breaking (H_{12}^a does not depend on ω). Furthermore for the third doublet (see Fig. 4.8b) no data could be taken close to resonance at about 50 mT. Here the absorptive properties of the ferrite too strongly influence the resonance shapes in the transmission spectra and prevent a description in a two-state model.

4.4 Conclusions

The most obvious effect of broken time-reversal symmetry on scattering systems is the violation of detailed balance or reciprocity which becomes evident in transmission measurements. However, the results obtained for measurements of singlets show that $\mathcal{T}$ breaking does not need to imply a violation of reciprocity in all cases. As the magnetic field of a singlet is just a vector oscillating back and forth in time, a reversal of time does not fundamentally change the character of its motion and leaves the interaction with the ferrite unchanged. In two-level systems, doublets, the rf magnetic fields of two modes add up coherently. This gives rise to elliptical motions which can in turn be decomposed into circular polarized modes. These couple differently to the ferrite, thus the net effect of the ferrite on the scattering system changes under time-reversal and reciprocity is violated. Using this insight, the $\mathcal{T}$ violating part of the effective Hamiltonian can be understood. On a broader scope the present work demonstrated that it is possible to probe time-reversal invariance in resonant systems already at fairly low excitation energies. As soon as two levels happen to interfere, $\mathcal{T}$ breaking cannot just be observed, it can even be quantified.

In general, for the study of TRSB effects it is, however, desirable to investigate scattering systems with many interfering resonances, a fact already pointed out in Ref. [36]. Interferences translate into a rich mode structure at the position of the ferrite which in turn results in more pronounced differences in the scattering matrix for time-reversed processes. This will be the topic of the next chapters.

5 Overlapping resonances

Scattering particles from a target is a basic process used to investigate the target. In many fields of physics, scattering provides a crucial approach to the dynamics of a system [44, 70, 91, 92]. This is especially true in nuclear physics where much information on the physics of a nucleus is gained by means of scattering experiments. There, impinging probe particles of not too high energy interact with the target nucleus and form an intermediate state, a so-called *compound nucleus*. The subsequent decay of the compound system gives rise to reaction cross sections that vary with the energy of the initial probe particle. For these processes the cross section displays resonances corresponding to (excited) states of the target nucleus. The S-matrix is described by Eq. (2.7). In this description every resonance is represented as a pole term in the complex plane (H^{eff} is complex due to the coupling W). For each excitation energy, their contributions add up coherently to the total scattering amplitude (and phase). At a low excitation energy of the target one finds isolated resonances, similar to the singlets and doublets studied in the preceding sections. With increasing excitation energy the mean level spacing D decreases while, at the same time, the mean width Γ of the resonances increases. This leads to overlapping resonances in reactions proceeding via a highly excited compound nucleus. Due to the coherent summation of the pole terms the cross section exhibits statistical fluctuations that cannot be attributed to single resonances any more. This effect was first predicted by Ericson [33, 93] in the 1960s and shortly thereafter experimentally confirmed in numerous works [94–99]. Individual resonances cannot be resolved any longer and standard level statistics [19, 56] do not apply any more. Instead of the parameters of individual levels, the experiment yields correlations between S-matrix elements or between cross sections. In 1984 Verbaarschot, Weidenmüller and Zirnbauer (VWZ) derived a general expression for the correlations between scattering matrix elements [48, 100]. This expression goes beyond the result for $\Gamma/D \gg 1$ by Ericson [101]. It is valid for GOE systems and (this is their main achievement) any ratio Γ/D. However, in nuclear physics till the present day no stringent experimental test of the VWZ formula could be performed as there only the cross section, i.e. the modulus square of the scattering matrix elements, is accessible.

Once again, the analogy between scattering experiments in nuclear physics and scattering experiments in microwave resonators is of great help. The reaction channels are modeled by the antennas and their connecting coaxial cables, that usually only support the propagation of a single mode each. The compound nucleus is in turn simulated by the microwave resonator. This recently allowed for a first rigorous and statistically sound test [49, 102] of the VWZ model and confirmed the consistency between experimentally determined autocorrelation functions and the VWZ model.

The present work takes these results one step further and investigates the TRSB effects of a ferrite on the fluctuation properties of the scattering matrix. In Sec. 5.1 the experimental setup and the process of data acquisition is explained. The breaking of time-reversal symmetry is demonstrated in Sec. 5.2 by the violation of reciprocity. Then, in Sec. 5.3 the dependence of the autocorrelation function on the symmetry of the scattering system is examined. This is exploited in Sec. 5.4, where the models for GOE and GUE systems are recapitulated. For a rigorous test of these models, fitting and testing procedures are required; they are presented in Secs. 5.6 and 5.7, respectively. All this leads to a statistical test of each of the two models in Sec. 5.8. There, it is shown that both GOE and GUE describe the data only in limiting situations. The present data require an extended model. It is described and tested in Sec. 6 and works with partially broken $\mathcal{T}$ symmetry.

5.1 Experiment

The microwave resonator used in the experiment must satisfy three requirements: First, its dynamics must be fully chaotic. Second, the regime of overlapping resonances must be accessible while still a reasonably high quality factor needs to be maintained. Third, $\mathcal{T}$ symmetry must be (partially) broken. These criteria are met by a large, tilted stadium billiard [103] of the type used in the first tests of the VWZ formula [49, 102].

The resonator is shaped according to a quarter circle with an attached trapezoid. It has been described in Ref. [104], however, the contour plate is replaced by

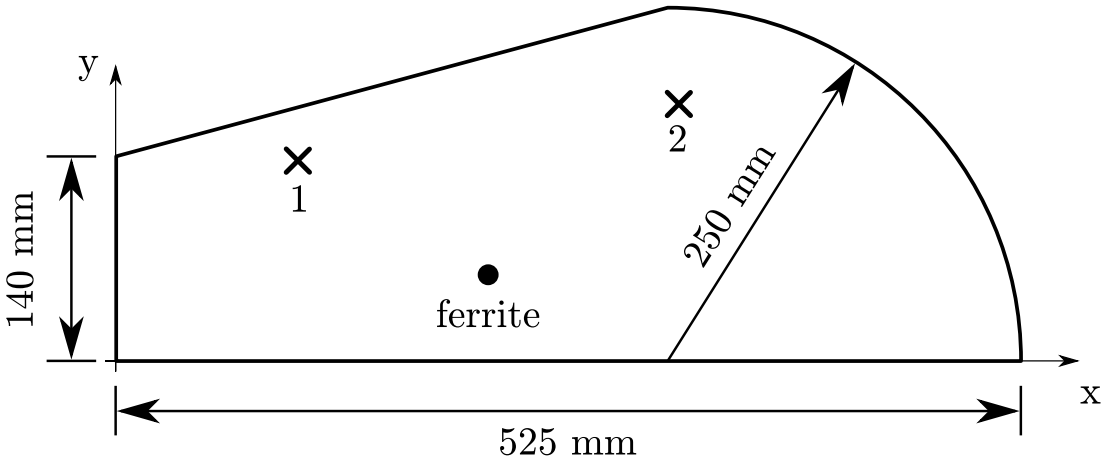

Fig. 5.1: Scheme of the tilted stadium billiard. The two antennas labeled 1 and 2 are located at $(x, y) = (105\text{ mm}, 140\text{ mm})$ and $(325\text{ mm}, 180\text{ mm})$, respectively. The height of the cavity is 5 mm. The ferrite (not drawn to scale) is positioned at $(x, y) = (215\text{ mm}, 60\text{ mm})$.

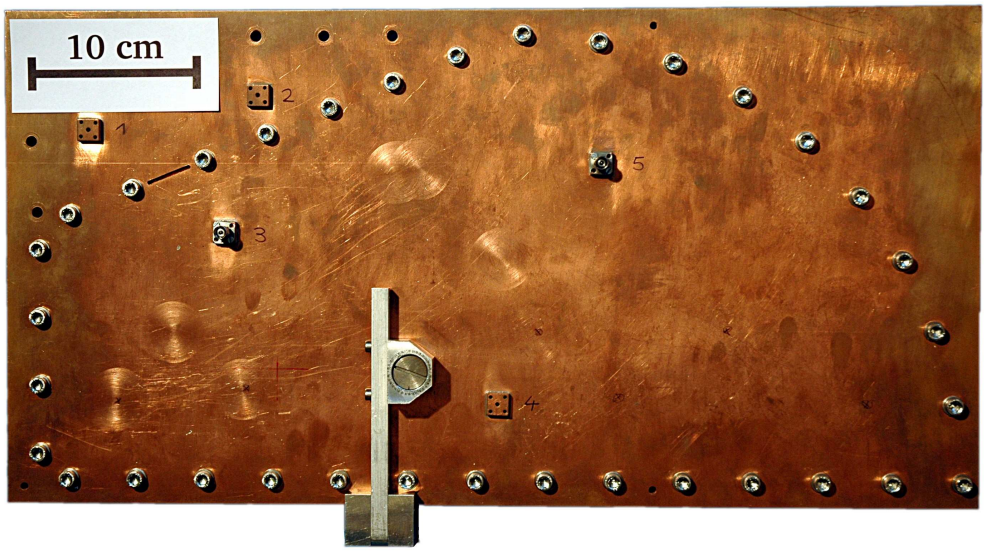

Fig. 5.2: Top plate of the tilted stadium. The line of screws indicates the contour of the resonator. Two antennas with HP 2.4 mm connectors are visible. At the position of the ferrite a magnet is placed together with its supporting structure (see also Fig. 4.3).

a newly fabricated copper plate which is only 5 mm in height to match the height of the ferrite. The top and bottom plates (copper, 5 mm thickness) are unchanged. Figure 5.1 gives the shape of the resonator and its dimensions; Fig. 5.2 shows the

top plate of the final setup. The tilted variant of the original stadium billiard [9] is chosen to suppress neutrally stable "bouncing ball" orbits [90]. These are known to introduce non-generic properties and would be in disagreement with RMT. The large area of the cavity ensures a high level density. Due to the reduced height the resonator can be treated as two-dimensional up to 30 GHz. A 2×2 scattering matrix can be measured by help of two antennas (labeled 1 and 2 on Fig. 5.1). Their metallic pins reach about 2.5 mm into the cavity and provide a good coupling between the bound states and the reaction channels. Time-reversal symmetry is again broken by the CV19 ferrite of 4 mm diameter used throughout this work. Its position is indicated on Fig. 5.1. The ferrite is magnetized by two NdFeB magnets (20 mm in diameter, 10 mm in height) on either side of the cavity. They are held in place by the same screw thread mechanism as in Sec. 4.1.

Data of the two-port S-matrix (S_{11}, S_{12}, S_{21}, S_{22}) have been measured in the frequency range of 1–25 GHz with a step width $\Delta f = 100$ kHz. The microwave resonator is connected to the VNA (model Agilent PNA-L N5230A) by coaxial cables of the type SF 101PEA by Hubert+Suhner of length 570 mm with HP2.4 connectors. The cables and connectors allow for reproducible measurements with good phase stability over the desired frequency range. A calibration of the setup is done with the Agilent N4693-60002 Electronic Calibration Module. This procedure removes the influence of the VNA and the coaxial cables (signal attenuation and frequency dependent phase shifts) on the data. However, this calibration does not take the radiation and absorption characteristics of the antennas into account. The attenuations of the antennas can be determined in reflection measurements of a cavity far from any resonances. In this situation, the reflection coefficient should be 1 but for absorptive losses in the antennas. A tiny circular resonator, 5 mm in diameter and 20 mm in depth, shows its first resonance at 33.02 GHz, allowing for a "clean" determination of these additional losses. Additional phase shifts of the signal due to the antennas can be eliminated by a line of best fit to achieve a stationary phase. The success of this post-VNA calibration procedure is illustrated in Fig. 5.3.

It is the nature of RMT to make statements on the general behavior of chaotic systems rather than a specific one. In analytical and numerical calculations this is achieved by *ensemble averages* over a large number of different Hamiltonians with the same symmetry properties at a fixed frequency. In the experiments

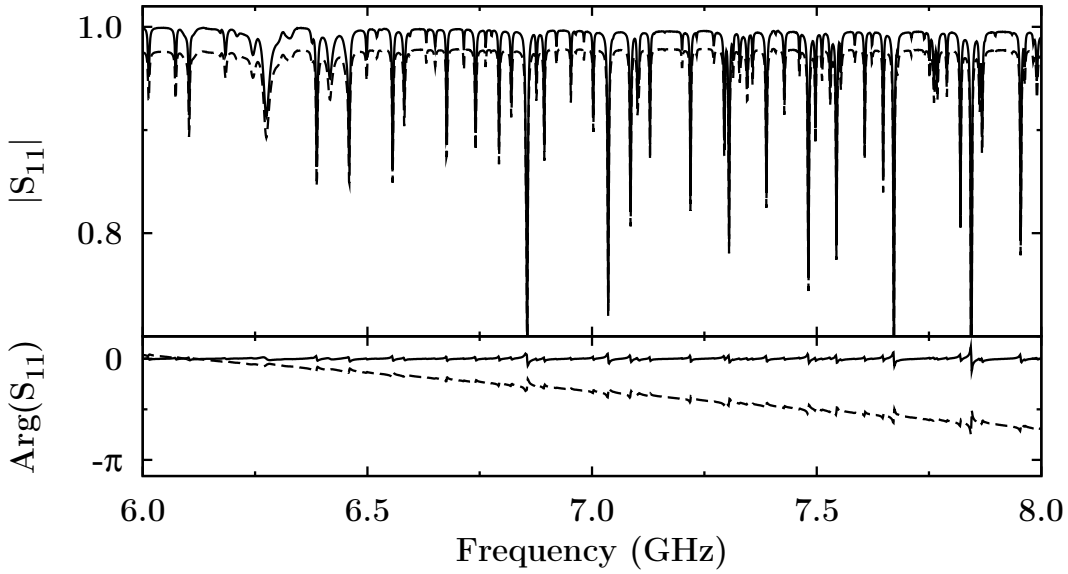

Fig. 5.3: Comparison of reflection spectra of the tilted stadium billiard before (dashed) and after (solid) correcting for the attenuation and phase shifts of the antennas. In the above frequency range of 6–8 GHz, an approximately constant attenuation of about 2 % in the amplitude (upper panel) and a linear phase change (lower panel) are removed.

this is normally not feasible, and *spectral averages* are performed, i.e. the Hamiltonian is kept fixed but the excitation frequency is changed. This method has its limitations, since the parameters—such as level density, coupling strength, losses—slowly change with frequency. This puts severe limits on the statistical significance of the available dataset. This problem is solved by a resonator with boundary conditions that depend on a parameter changed by the experimenter. The parameter can be provided by a movable wall [105, 106] or movable scatterers [107]. Only the latter procedure keeps the area of the resonator and thus the level density unchanged. Therefore the present experiments include an additional scatterer within the cavity volume; namely an iron disc, 20 mm in diameter and 5 mm in height. The ferromagnetic iron has no influence on the time-reversal symmetry of the Hamiltonian describing the billiard. The scatterer can be moved from the outside via a small permanent magnet. In this way the scatterer is freely moved inside the resonator. To minimize Ohmic and rf losses, a bar clamp is positioned around bottom and top plate at the position of the iron disk. It squeezes the plates and assures good electrical contact between the

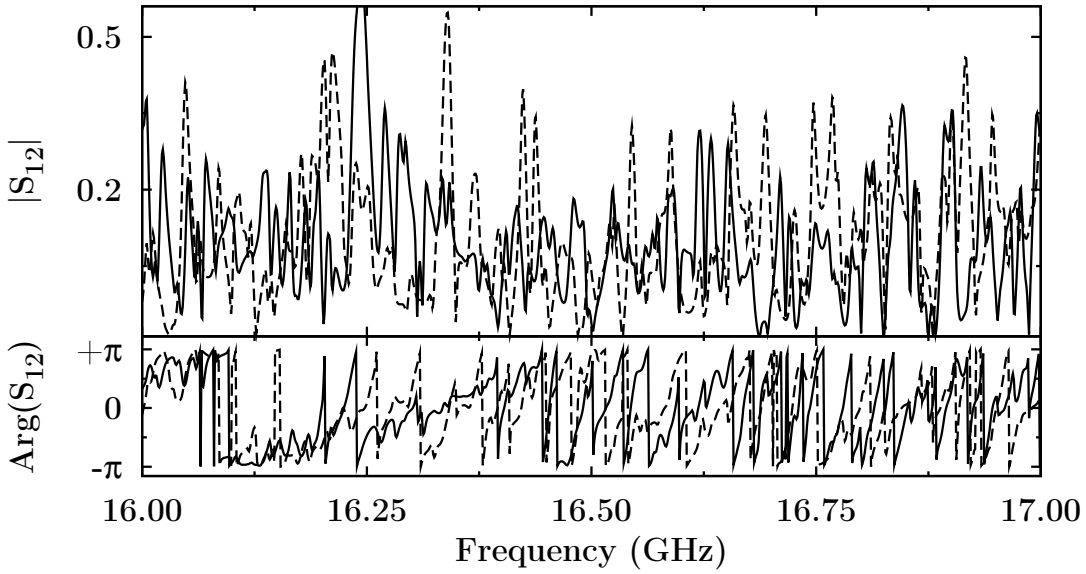

Fig. 5.4: Comparison of the transmission spectra of two realizations of the tilted stadium billiard. The upper panel displays the modulus, the lower one the phase of S_{12}. For the two realizations (dashed and solid lines), the iron disk has been shifted by about 50 mm. The remaining correlation (see its definition in Eq. (5.1)) has the absolute value of 0.18. This value is expected for independent spectra in the finite frequency interval given in the figure.

components. Care was taken to keep the scatterer at least one wavelength apart from both, the ferrite and the antennas, in order to preserve the physically relevant properties of the system. In this way, up to 12 independent spectra, which will be called *realizations*, have been obtained for each setup. An example of two realizations is shown in Fig. 5.4.

The quality of the data ensemble can be estimated looking at the residual correlation

$$R_{\alpha,\beta} = \frac{\langle S_{12,\alpha}\, S^*_{12,\beta}\rangle}{\sqrt{\langle |S_{12,\alpha}|^2\rangle \langle |S_{12,\beta}|^2\rangle}} \tag{5.1}$$

of transmission spectra of two realizations α and β, where $\langle\cdot\rangle$ denotes spectral averages. One expects $R_{\alpha,\beta} = 0$ for data taken over an infinite interval. For any finite data set $|R_{\alpha,\beta}| > 0$ is to be expected. An evaluation of Eq. (5.1) in the frequency range of 17.8–20 GHz includes about 300 resonances. Taking the average over all possible combinations of the 12 measured realizations gives

$|\overline{R^{\mathrm{meas}}_{\alpha,\beta}}| = 0.17 \pm 0.07$. Random matrix theory simulations (including 300 resonances) of independent spectra yield $|\overline{R^{\mathrm{RMT}}_{\alpha,\beta}}| = 0.06 \pm 0.03$ and confirm that the data of different realizations are nearly uncorrelated.

The number of resonances below the frequency f is given by Weyl's formula [108–110]

$$N_{\mathrm{Weyl}} = \frac{A\,\pi}{c_0^2}\,f^2 - \frac{L}{2\,c_0}\,f + \mathrm{const}\,. \tag{5.2}$$

Here, A and L are area and circumference of the resonator. The additional constant depends on the geometry of the billiard. The tilted stadium used here has the area of $A = 1029.4$ cm^2 and the circumference of $L = 136.0$ cm. Due to the quadratic term in Eq. (5.2), the level spacing D decreases with frequency. For a typical resonance width of $\Gamma = 1.3$ MHz at 3 GHz excitation frequency (see left panel of Fig. 5.5) the resonances are therefore isolated at low frequencies (see Sec. 4) and eventually start to overlap for higher excitation frequencies. At even higher frequencies the resonances fully overlap and the spectrum exhibits Ericson fluctuations. This transition is demonstrated in Fig. 5.5, which displays the modulus of S_{12} for isolated resonances ($\Gamma/D \ll 1$), for weakly overlapping ($\Gamma/D \approx 1$), and for strongly overlapping resonances ($\Gamma/D \gg 1$).

Unless in the regime of isolated resonances Γ and D cannot be determined directly. In nuclear physics the determination of Γ/D for overlapping resonances is challenging and requires a profound understanding of the statistical properties of the scattering process. This issue will be further addressed in Sec. 5.4.

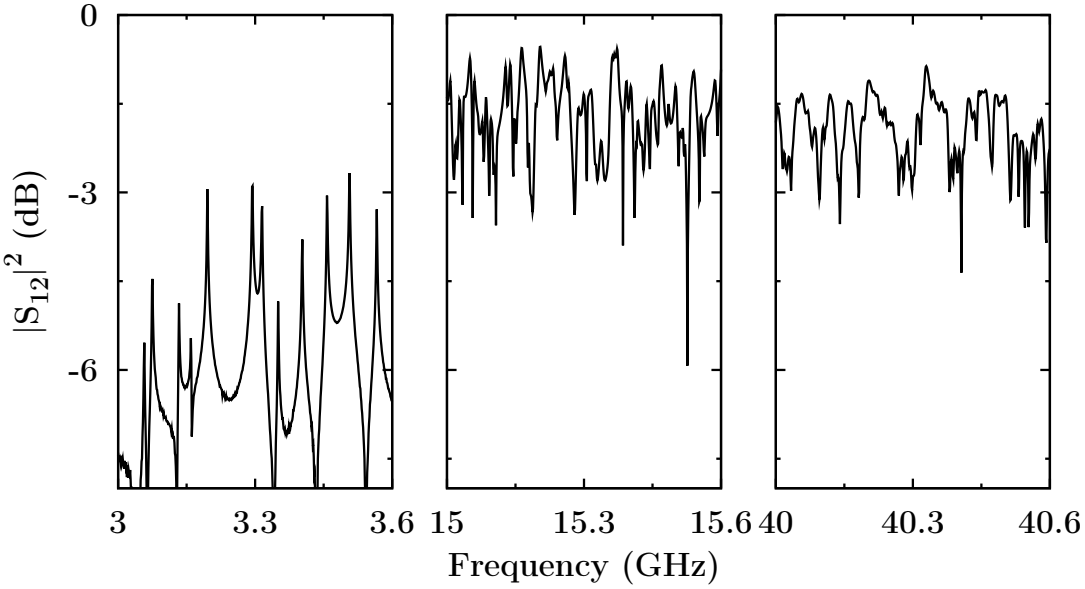

Fig. 5.5: Transmission spectra in the tilted stadium billiard for three frequency ranges. Left panel: At low frequencies the resonances are isolated; 12 resonances are visible. Center panel: At intermediate frequencies the resonances partially overlap and the naked eye cannot distinguish them any more. Weyl's formula predicts 64 resonances between 15 and 15.6 GHz. Right panel: At high frequencies the transmission shows no further resemblance to resonances; instead it fluctuates. This window includes about 500 resonant states. One can estimate this via an extension [49] of Eq. (5.2) to three dimensions. In each figure the ordinate is in the same logarithmic scale, $|S_{12}|^2\,\mathrm{dB} \hat{=} 10\log_{10}(|S_{12}|^2)$.

5.2 Reciprocity

A direct, intuitive way to estimate the time-reversal symmetry breaking effect of the ferrite is to compare forward to backward reactions. In the case of isolated resonances the violation of reciprocity, Eq. (3.1), served as a good indication of induced TRSB, see Fig. 4.6. Figure 5.6 demonstrates the violation of reciprocity in the range of 16–17 GHz. This proves that the ferrite, even though the ferromagnetic resonance lies for $B = 190$ mT at 6.6 GHz, still induces $\mathcal{T}$ breaking to some degree at higher frequencies.

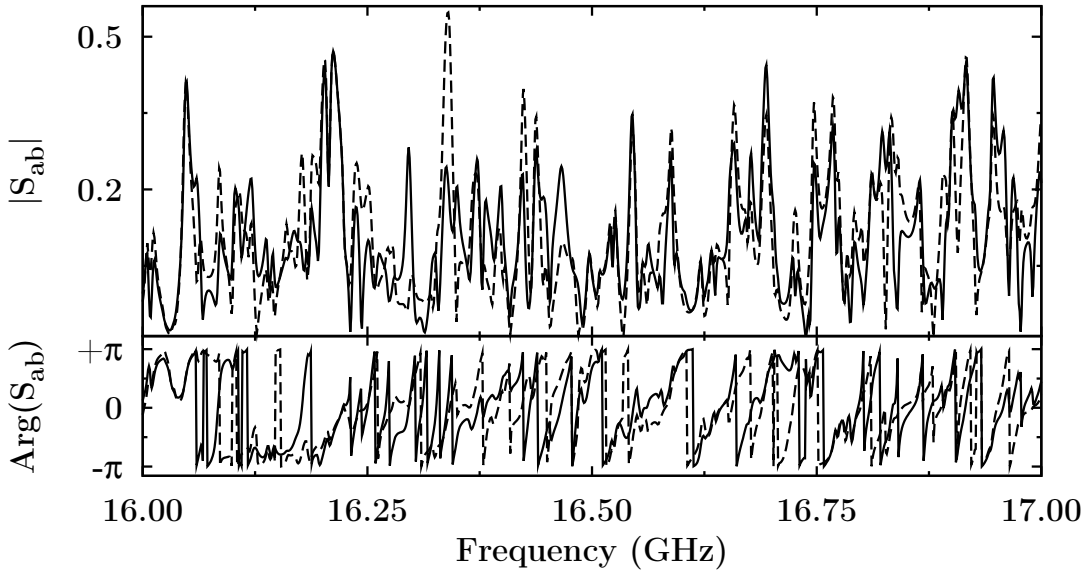

Fig. 5.6: Violation of reciprocity in the tilted stadium billiard. For an external magnetic field of 190 mT the two scattering matrix elements S_{12} (solid) and S_{21} (dashed) do not agree, neither in amplitude nor in phase.

A more detailed analysis is possible by means of a contrast function

$$\Delta = \frac{S_{12} - S_{21}}{|S_{12}| + |S_{21}|} \,. \tag{5.3}$$

It is bounded by 0 (reciprocity holds) and 1 (maximal $\mathcal{T}$ breaking effect). The results are given in Fig. 5.7; Δ shows strong fluctuations as a function of frequency. This is due to the small level spacing in the regime of Ericson fluctuations and

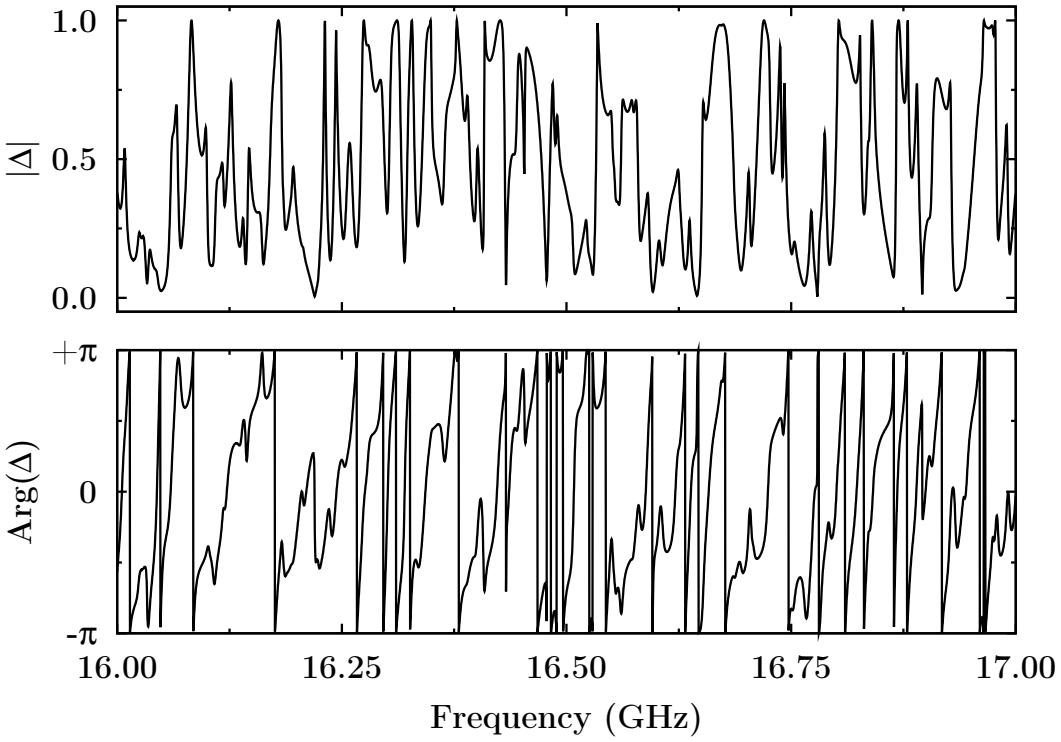

Fig. 5.7: Contrast function Eq. (5.3) in the tilted stadium billiard with an external magnetic field of 190 mT. Both, modulus (upper panel) and phase (lower panel), show strong fluctuations over the whole possible codomain of Δ.

demonstrates how sensitive the TRSB effect of the ferrite is to changes in the local structure of the rf magnetic field. The fluctuations of Δ correspond to independent fluctuations of the $\mathcal{T}$ conserving and $\mathcal{T}$ non-conserving reaction amplitudes in compound nucleus reactions [111, 112].

For this reason nuclear physicists have tried to detect the presumably small TRSB scattering amplitude via compound nucleus reactions [30, 113], especially in the regime of Ericson fluctuations. There, Δ was defined as the relative difference between the cross section in forward $\overrightarrow{\sigma}$ and backward $\overleftarrow{\sigma}$ directions, see Eq. (1) in Ref. [30]. The reaction amplitudes were decomposed into $\mathcal{T}$ non-invariant and $\mathcal{T}$ invariant parts f' and f, see Eq. (2) therein; f' and f were assumed to fluctuate independently. Then an average $\mathcal{T}$ non-invariant strength $\xi^2 = \langle|f'|^2\rangle/\langle|f|^2\rangle$ can be defined, see Eq. (3) in [30]. It follows that $\xi \leq |\Delta/(4\sqrt{\nu})|\, Z$, see Eq. (4) therein. The strength is evaluated in a cross section minimum, where the cross section is a factor ν smaller than the average cross

section; Z is a number related to the confidence interval of the test. The observed cross section difference Δ is enhanced by the factor $\sqrt{\nu}$. As a consequence the quoted experiment concentrated on energies where the cross sections exhibited a pronounced minimum. This enhancement of $\mathcal{T}$ violation effects was theoretically predicted by Ericson [34] and refined by Mahaux and Weidenmüller [35]. Knowledge of Δ then defines with a probability K an upper bound on ξ. Note that this analysis applies under the assumption $|f'| \ll |f|$, i.e. small $\mathcal{T}$ violation [113].

In the present experiments with microwave billiards, the frequency ranges considered so far are not suited for this analysis. Figure 5.7 shows that below 20 GHz the effect of the ferromagnetic resonance still leads to $|\Delta| \approx 1$. Therefore on Fig. 5.7 peaks in $|\Delta|$ do not correspond to valleys in $|S_{ab}|$ on Fig. 5.6. Going

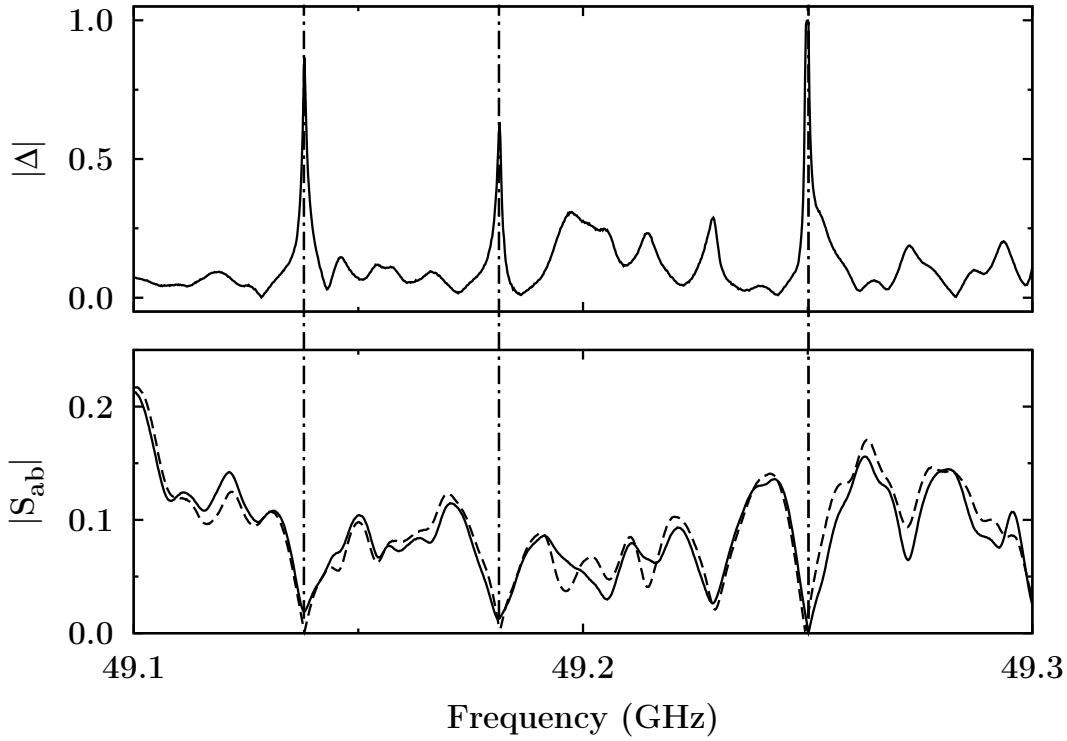

Fig. 5.8: Contrast function at very high excitation frequencies. With a magnetic field of 190 mT the effect of the ferromagnetic resonance on the scattering process is weak and the difference between $|S_{12}|$ and $|S_{21}|$ is small (solid and dashed lines, resp., in the lower panel). The contrast (upper panel) displays, however, sharp peaks wherever the transmission is minimal, see the dash-dotted vertical lines.

to higher excitation frequencies should, however, bring the microwave experiment into the situation of weak $\mathcal{T}$ breaking. To this end measurements up to 50 GHz (the upper limit of the VNA) have been carried out. At such high frequencies the residual influence of the ferromagnetic resonance is small. Nonetheless reciprocity is still violated. Figure 5.8 shows two reciprocal transmission spectra and the calculated values of $|\Delta|$. In full agreement with the expectations described above, the contrast exhibits peaks whenever the scattering amplitude undergoes a minimum. This corroborates the motivation for the nuclear scattering experiments performed more than 40 years ago [26].

The discussion of the present section shows the close relationship between scattering experiments in nuclear physics and in microwave resonators and emphasizes that this analogy even holds in the broader scope of $\mathcal{T}$ invariance and its (partial) breaking. However, for strong TRSB effects the relation between a given value of Δ and some quantum mechanically defined degree of TRSB is not clear. Hence, a further measure of TRSB is needed and will be discussed in Sec. 6.2.

5.3 Compound nucleus and Ericson fluctuations

In the 1930s, Bohr formulated the idea of nuclear reactions proceeding via an intermediate many particle state [114], the compound nucleus. A formal description of this scattering process is, as given by Mahaux and Weidenmüller [43], divided into two parts: The system of bound states and the free motion of incoming and outgoing particles as reaction channels. This is illustrated in Fig. 5.9. In this picture an incident particle a collides with the target nucleus A and forms an excited compound nucleus which eventually decays into an outgoing particle b and a residual nucleus B. The number of additional channels $c, c', \ldots$ varies with the excitation energy of the compound nucleus. In this model all interactions of the bound states with the outside world takes place via open reaction channels. The antennas connected to the microwave resonator obviously correspond to open channels. The inevitable Ohmic losses in microwave experiments are modeled as

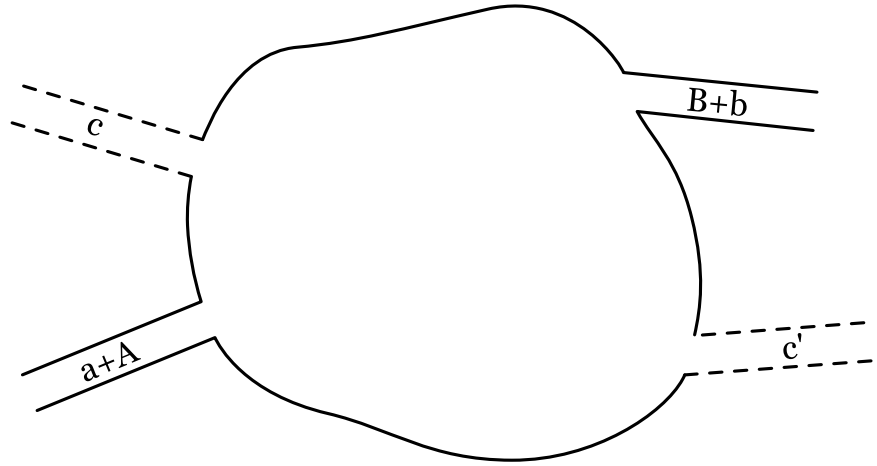

Fig. 5.9: A compound nucleus reaction schematically. The incident and outgoing particles are represented as (solid) channels that are connected to the chaotic system of bound states. The number of additionally accessible channels (dashed) depends on the excitation energy of the compound nucleus.

follows. One represents them by a large number[4] of "absorptive" (sometimes referred to as "parasitic") channels, each of which is weakly coupled to the scattering system [115, 116]. Only scattering channels connected to antennas can be individually studied; the measured S-matrix is sub-unitary.

Between formation and decay of the compound nucleus there is a period of equilibration, i.e. the time scale for intrinsic mixing of the compound nucleus states is small compared to the average nuclear decay time [117]. During this mixing time the energy is distributed in the nucleus. The excited nucleus decays when this process happens to be reversed and enough energy is concentrated in one place to allow for a part of it to separate. In contrast, "direct reactions" describe fast events where the projectile interacts only with a small part of the target nucleus and give simultaneously rise to additional contributions to the total cross section. However, direct reactions are not included in RMT because they do not involve the complete dynamics of the scattering system. It is possible

[4]A note on the definition of "large number": Analytical treatments usually consider the limit of an infinite number of infinitely weakly coupled channels. Numerical simulations require for the problem at hand about 30 channels with finite coupling in order to arrive at converged results. Experimentally, the number of required channels should be comparable to the ratio of the resonator surface area to the square of the wavelength, giving the number of independent surface cells.

to reduce the problem to one without direct contributions by a suitably chosen unitary transformation of the scattering matrix [118]. In microwave experiments fast processes correspond to a direct energy transfer between the emitting and the receiving antenna. This crosstalk between the channels a and b is defined as the frequency independent part of $S_{ab}(f)$, i.e. $\langle S_{ab}(f)\rangle$. In the present work this average value (evaluated in frequency windows of size 1 GHz) is $\leq 5 \times 10^{-5}$ at 1 GHz, $\leq 5 \times 10^{-3}$ at 10 GHz and $\leq 2 \times 10^{-2}$ at 25 GHz. In all cases this is less than about 8 % of $\langle |S_{ab}(f)|\rangle$. This justifies neglecting direct reactions in the further analysis.

To define the probability T_c for a particle to be transmitted from the system of bound states into a channel c, the S-matrix is decomposed into two parts; a slowly varying smooth part $\overline{S_{cc'}}$ originating from fast reactions and a fluctuating part $S^{\mathrm{fl}}_{cc'}$ describing resonant reactions. According to the foregoing paragraph it is

$$\overline{S_{cc'}} = 0 \text{ for } c \neq c' \,. \tag{5.4}$$

Summing the contributions from all final scattering channels $T_c = \sum_{c' \neq c} \overline{|S^{\mathrm{fl}}_{c'c}|^2}$ defines the *transmission coefficient* with $0 \leq T_c \leq 1$. The sum includes the absorptive channels. By the unitarity of the complete S-matrix, $\sum_{c'} |S_{c'c}|^2 = 1$, and Eq. (5.4) the result is

$$T_c = 1 - |\overline{S_{cc}}|^2 \,. \tag{5.5}$$

Thus T_c is the unitarity deficit of the average S-matrix. It turns out that the transmission coefficients T_c and the mean level spacing D of the compound system provide the complete list of parameters of the chaotic system of resonances. The preceding averages $\overline{\cdot}$ are meant to be ensemble averages which, due to ergodicity [14], in the experiment are replaced by spectral averages $\langle\cdot\rangle$, cf. Sec. 5.1.

When Ericson predicted the fluctuating nature of the cross section in the regime of overlapping resonances, he also showed that the autocorrelation function is the tool to analyze the fluctuations [33]. He understood that the fluctuations are characteristic of the dynamics and that they contribute, just like the average of the cross section, an essential part to the description of compound nucleus reactions [101]. The autocorrelation function of the S-matrix element S_{ab} is

$$C_{ab}(\epsilon) = \langle S_{ab}(f)\, S^*_{ab}(f+\epsilon)\rangle - |\langle S_{ab}(f)\rangle|^2 \,. \tag{5.6}$$

It quantifies the correlation between S_{ab} and S_{ab}^* at the points f and $f+\varepsilon$. Since S_{ab} is an analytic function of f the correlation cannot vanish identically for $\varepsilon \neq 0$. Ericson found

$$C_{ab}(\epsilon) = C_{ab}(0)\,\frac{1}{1+i\,\epsilon/\Gamma_{\mathrm{corr}}}\,. \tag{5.7}$$

This means that $|C_{ab}|^2$ decreases in form of the Lorentzian function, $|C_{ab}|^2 \propto 1/(1+(\varepsilon/\Gamma_{\mathrm{corr}})^2)$. The parameter Γ_{corr} is called the correlation length of S_{ab}. At $\epsilon = \Gamma_{\mathrm{corr}}$ the modulus square of the autocorrelation is down to half its initial value. At isolated resonances $1/\Gamma$ gives the timescale for the exponential decay of the compound nucleus. For strongly overlapping levels, where Eq. (5.7) holds, the compound nucleus also decays exponentially, on a timescale given by $1/\Gamma_{\mathrm{corr}}$. Thus Γ_{corr} takes over the role of the widths Γ of individual resonances in the regime of Ericson fluctuations. Points separated in the spectrum by more than $2\pi\,\Gamma_{\mathrm{corr}}$ can be considered as effectively uncorrelated. In nuclear physics the condition $\Gamma/D \gg 1$ is easily reached for reactions above the energy threshold for neutron emission. An introduction to nuclear cross section fluctuations is given in Ref. [93]. Experimental investigations of Ericson fluctuations and a comparison of the Lorentzian shape to the data are presented for example in Refs. [53, 96, 119].

It is interesting to note that the normalization factor $C_{ab}(0)$ appearing in Eq. (5.7) equals

$$C_{ab}(0) = (1+\delta_{ab})\,\frac{T_a\,T_b}{\sum_c T_c}\,, \tag{5.8}$$

in the Ericson regime of $\mathcal{T}$ invariant systems [120]. Except for the factor $1+\delta_{ab}$, this is the Hauser-Feshbach formula [121]. It postulates that formation and decay of the compound nucleus are independent of each other. The prefactor $1+\delta_{ab}$ takes the symmetry of the S-matrix into account. This *elastic enhancement factor* will be further discussed in Sec. 6.4. It expresses the fact that the compound nucleus "remembers" its entrance channel.

5.4 Models for GOE and GUE systems

The model Eq. (5.7) fails outside the Ericson regime. However, a general description of the statistical properties of fluctuations was given in 1984 by Verbaarschot, Weidenmüller and Zirnbauer [48, 100]. They derived an expression for $C_{ab}(\epsilon)$ that should hold for all possible values of T_c and for all regimes of Γ/D provided that RMT correctly assesses the properties of quantum chaos. Their model applies to time-reversal invariant systems.

Their starting point was Eq. (2.7). This ansatz was "completed" by taking the internal Hamiltonian H from the GOE. The idea to model compound nucleus reactions by RMT was justified, as numerical calculations had shown [122] that spectra of highly excited nuclei are in convincing agreement with predictions based on the GOE. The analytical solution of the problem is based on the mathematical methods of supersymmetry [123, 124]. The authors arrived at

$$\begin{aligned} C_{ab}(\epsilon) &= \frac{1}{8}\int_0^\infty \mathrm{d}\lambda_1 \int_0^\infty \mathrm{d}\lambda_2 \int_0^1 \mathrm{d}\lambda\, \mu(\lambda,\lambda_1,\lambda_2) \\ &\quad \times \exp\left(-i\,\pi\,\epsilon\,(\lambda_1+\lambda_2+2\lambda)/D\right) \\ &\quad \times J_{ab}(\lambda,\lambda_1,\lambda_2) \\ &\quad \times \prod_c \frac{(1-T_c\lambda)}{((1+T_c\lambda_1)\,(1+T_c\lambda_2))^{1/2}}\,, \end{aligned} \tag{5.9}$$

a three-fold integral containing the functions

$$\mu(\lambda,\lambda_1,\lambda_2) = \frac{\lambda\,(1-\lambda)\,|\lambda_1-\lambda_2|}{(\lambda+\lambda_1)^2\,(\lambda+\lambda_2)^2\,(\lambda_1\,\lambda_2\,(1+\lambda_1)\,(1+\lambda_2))^{1/2}} \tag{5.10}$$

and

$$\begin{aligned} J_{ab}(\lambda,\lambda_1,\lambda_2) &= \delta_{ab}\,T_a^2\,(1-T_a) \\ &\quad \times \left(\frac{\lambda_1}{1+T_a\lambda_1}+\frac{\lambda_2}{1+T_a\lambda_2}+\frac{2\lambda}{1-T_a\lambda}\right) \\ &\quad + \ (1+\delta_{ab})\,T_a\,T_b \\ &\quad + \left(\frac{\lambda_1\,(1+\lambda_1)}{(1+T_a\lambda_1)\,(1+T_b\lambda_1)}+\frac{\lambda_2\,(1+\lambda_2)}{(1+T_a\lambda_2)\,(1+T_b\lambda_2)}\right. \\ &\quad + \left.\frac{2\,\lambda\,(1-\lambda)}{(1-T_a\lambda)(1-T_b\lambda)}\right)\,. \end{aligned} \tag{5.11}$$

The three-fold integral cannot be evaluated analytically and even a numerical treatment is challenging. To prevent singularities a re-parametrization of the integrals is necessary [125]; the results then are integrated numerically using alternatively Monte Carlo and Gauss-Legendre algorithms, which arrive at the same results. The VWZ expression Eqs. (5.9)–(5.11) is parameterized in terms of the transmission coefficients T_c and the level spacing D. The latter one gauges the frequency scale.

In the Ericson regime, the VWZ expression reduces to the results Eqs. (5.7, 5.8) by Ericson [33], and by Hauser and Feshbach [121]. The correlation length is given by [126]

$$2\,\pi\,\frac{\Gamma_{\mathrm{corr}}}{D} = \sum_c T_c\,. \tag{5.12}$$

Prior to 1984, this relation was already known from heuristic arguments [127] and approximative solutions [128]. This enabled Richter *et al.* [129] to determine the mean level spacing D in the regime of overlapping resonances by a comparison of the measured autocorrelation function to Eq. (5.7) and by help of the relations (5.8, 5.12). The transmission coefficients T_a, T_b were obtained from the optical model [130].

In the regime $\Gamma/D \gg 1$ with equal T_c the VWZ expression need not be tested since it coincides with the simple and generally accepted result of Eq. (5.7). However, for only partially overlapping resonances $\Gamma/D \approx 1$, the VWZ model predicts deviations from a Lorentzian shape for $C_{ab}(\varepsilon)$. This was experimentally tested with microwave resonators in Refs. [40, 116]. However, no exhaustive statistical test of VWZ has been performed until recently. In Refs. [49, 102] it has been established that scattering data obtained from microwave billiards are indeed described by the VWZ expression, if the billiard is, in terms of classical physics, chaotic.

One goal of the present work is to understand, how broken $\mathcal{T}$ symmetry manifests itself in the fluctuations of the S-matrix. To this end a model only valid for the GOE is not sufficient. About 20 years after the breakthrough of Verbaarschot *et al.*, their path was retraced [50] and Fyodorov, Savin and Sommers (FSS) used the same mathematical methods to derive a result with an Hamiltonian taken from the GUE. Independently, Verbaarschot [131] arrived at the same expression in 2007. His derivation follows the original work more closely in style.

His final result

$$
\begin{aligned}
C_{ab}(\epsilon) &= \frac{1}{4}\int_1^\infty \mathrm{d}\lambda_1 \int_{-1}^1 \mathrm{d}\lambda_2 \, \frac{1}{(\lambda_1-\lambda_2)^2} \\
&\quad \times \exp(-i\,\pi\,\epsilon\,(\lambda_1-\lambda_2)/D) \\
&\quad \times J_{ab}(\lambda_1,\lambda_2) \\
&\quad \times \prod_c \frac{1+(\lambda_2-1)\,T_c/2}{1+(\lambda_1-1)\,T_c/2}
\end{aligned}
\tag{5.13}
$$

with

$$
\begin{aligned}
J_{ab}(\lambda_1,\lambda_2) &= T_a\,T_b \\
&\quad \times \Bigg[\Bigg(\frac{\lambda_1^2-1}{(1+T_a\,(\lambda_1-1)/2)\,(1+T_b\,(\lambda_1-1)/2)} \\
&\quad - \frac{\lambda_2^2-1}{(1+T_a\,(\lambda_2-1)/2)\,(1+T_b\,(\lambda_2-1)/2)}\Bigg) \\
&\quad + \delta_{ab}\,(1-T_a) \\
&\quad \times \left(\frac{\lambda_1-1}{1+T_a\,(\lambda_1-1)/2} - \frac{\lambda_2-1}{1+T_a\,(\lambda_2-1)/2}\right)^2\Bigg]
\end{aligned}
\tag{5.14}
$$

looks quite similar to the VWZ expression. In contrast to the GOE result, Eq. (5.13) is only a two-fold integral. Again, it must be evaluated numerically.

Both the result Eqs. (5.9)–(5.11) for $\mathcal{T}$ invariant systems, and the result Eqs. (5.13, 5.14) for strongly $\mathcal{T}$ broken systems are parameterized in terms of T_c and D. The level spacing D can be calculated from Weyl's formula, Eq. (5.2). The transmission coefficients associated with the antennas a and b can be determined directly from the definition Eq. (5.5) while those representing absorptive channels are not directly accessible. In the calculations these are included as about 300 equivalent, weakly coupled additional channels. Then the numerical results do not depend on the exact number of absorptive channels, only their sum τ_{abs} is relevant. One finds τ_{abs} by fitting the model correlation function to the data.

5.5 Experimental autocorrelation functions

A comparison of some of the experimentally obtained autocorrelation functions to the VWZ and FSS models is shown in Fig. 5.10. The ferrite was magnetized with

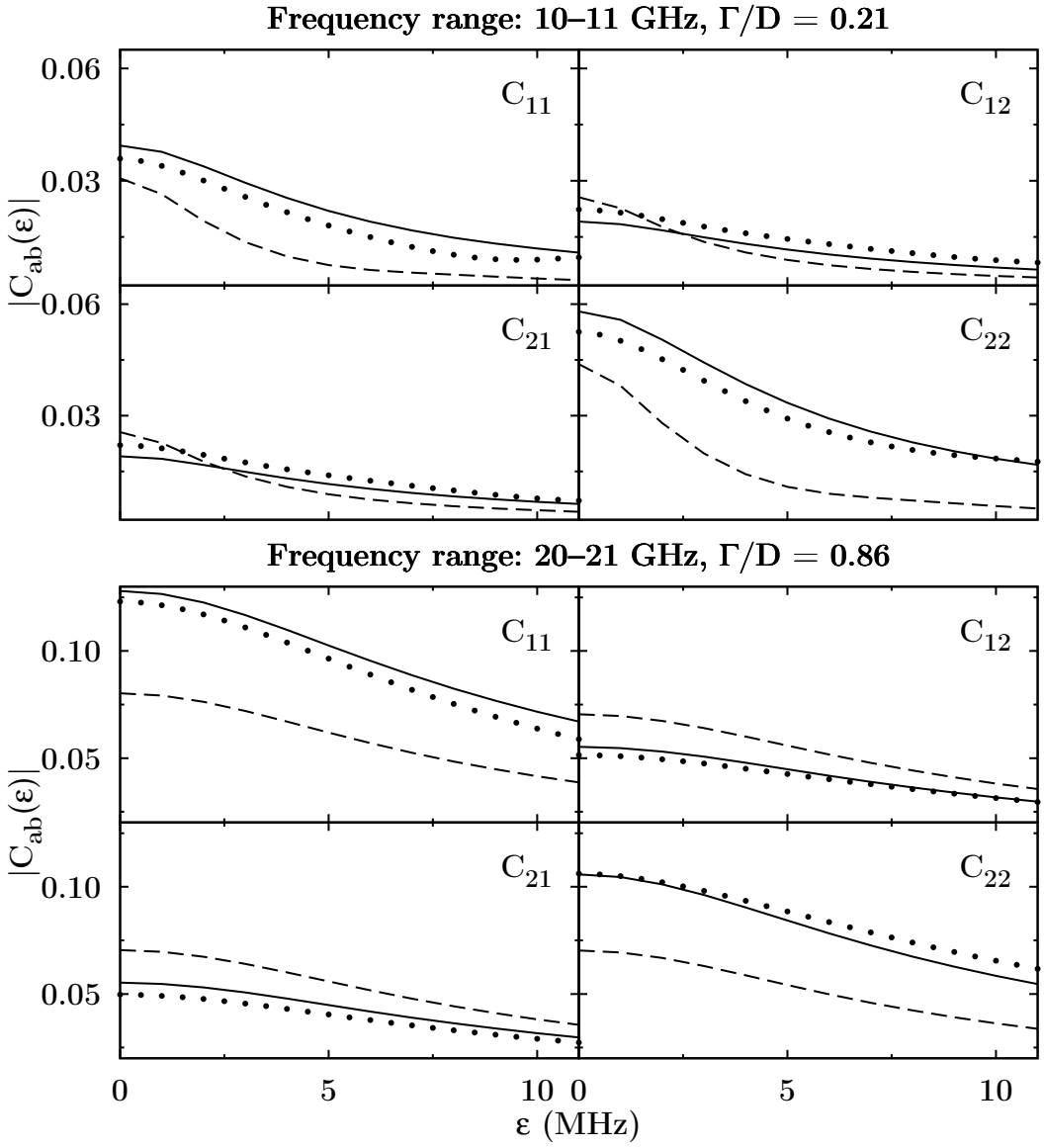

Fig. 5.10: Comparison of experimental autocorrelation functions (dots) for a single realization to the VWZ model (solid) and FSS model (dashed) predictions. The upper set of panels shows data with a magnetic field of 190 mT taken in the range 10–11 GHz, the lower one in the range 20–21 GHz. In each set the results for C_{11}, C_{12}, C_{21}, C_{22} are displayed.

a magnetic field of $B = 190$ mT. The figure shows data in the frequency ranges 10–11 GHz ($\Gamma/D = 0.21$) and 20–21 GHz ($\Gamma/D = 0.86$). The parameters T_1, T_2, τ_{abs} were determined by a maximum likelihood fit to the data, the level spacings D are known from Weyl's formula. The details on the applied fitting procedure are elucidated in Sec. 5.6. The obtained parameter sets are shown in Fig. 5.11. In general, the transmission coefficients increase with the excitation frequency, while the level spacings decrease. There are, however, systematic deviations in the estimation of τ_{abs}; the values predicted by FSS are mostly slightly larger. Summarizing the results shown in Figs. 5.10 and 5.11, one needs to assess whether

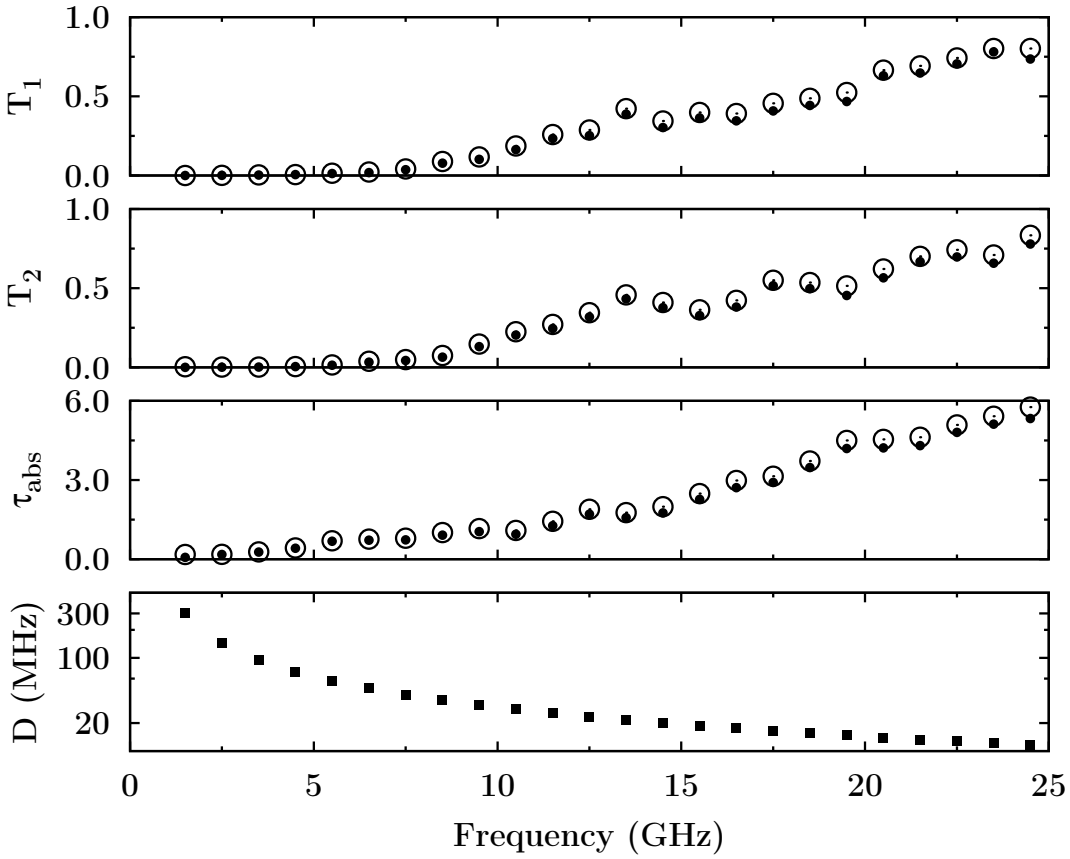

Fig. 5.11: Development of the parameters for the VWZ and FSS models for the data of a single realization with $B = 190$ mT. The panels display from top to bottom T_1, T_2, τ_{abs} and D. The transmission coefficients are obtained from the fit to VWZ (dots) and FSS (open circles). The level spacing D is known from Weyl's law and drawn in logarithmic scale.

VWZ or FSS correctly describes the data. Only, then it is possible to choose the correct parameter set. This decision cannot be made by the evaluation of the autocorrelation functions in Fig. 5.10, as there neighboring points are correlated. This calls for a proper statistical test, which will be discussed in Sec. 5.7.

5.6 Maximum likelihood fit

The absorptive parameter τ_{abs} is unknown and has, in a first step, to be determined by fitting the GOE based VWZ model or the GUE based FSS model to the experimental autocorrelation functions. In a second step, the quality of the fit has to be judged and the question "Does the model describe the data?" must be answered. Figure 5.12 shows data for the billiard with ferrite and magnetic field together with the fits. At a first glance, both fits give a rather poor result. While

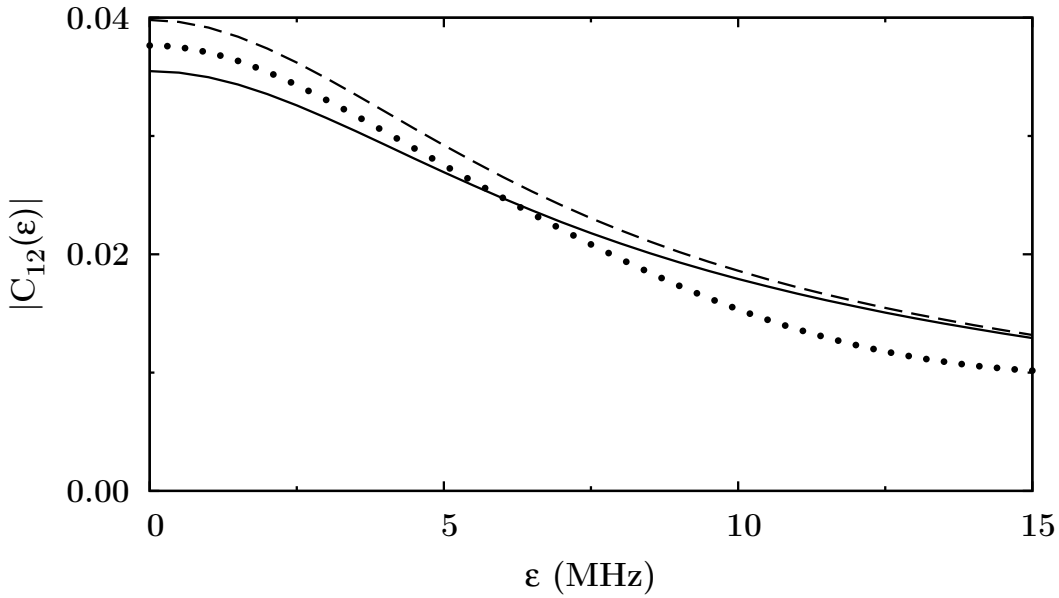

Fig. 5.12: Comparison between the experimentally determined autocorrelation function of S_{12} (dots), and the VWZ (solid) and FSS (dashed) models. The data were taken in the range of 16–17 GHz with a magnetic field of 190 mT. The input to the models was $T_a = 0.393$, $T_b = 0.388$ and $\tau_{\mathrm{abs}} = 2.758$ (2.953).

VWZ (solid line) starts too low and has a wrong slope, FSS (dashed line) starts too high but at least the slope approaches that of the data. To judge the quality of the fits error bars of the data have to be discussed. Two contributions are to be considered; (i) systematic errors due to an insufficient calibration of the VNA and (ii) errors due to the finite size of the data sample, so-called *finite range of data* (FRD) errors [132, 133]. The errors introduced by the VNA are negligibly small, see Sec. 5.1. Finite range of data errors arise from the finite number of independent data points included within each frequency window (cf. Sec. 5.3), whereas, in contradistinction, the theoretical models rely on expectation values over an infinite number of states. Finally, the measured scattering matrix $S(f)$ is correlated for different values of f. As a consequence the data points of the obtained correlation function do not scatter around their true value but either pass in a large range of ε all too high or all too low. This severely hampers a rigorous statistical test of the results, as error bars cannot be interpreted statistically for correlated data points.

The problems occur only if one works in the frequency representation of the data. One can represent them in the time domain by virtue of a Fourier transform. In this way one arrives at data that are statistically independent. Analyses of nuclear cross section fluctuations in the time domain have already been performed [134, 135] and first statistical tests have been developed [136]. Gorin and Seligmann already calculated the Fourier transform of the VWZ expression[5] for a theoretical comparison of fluctuations in chaotic and regular systems [137]. In experiments with microwave billiards, this route has already successfully been pursued in Ref. [138] and Refs. [49, 102]. In the latter ones the foundation has been laid for the analysis of the present data. The methods established in Ref. [49] to determine the most probable value of τ_{abs} can be summarized as follows:

- The experimental data are corrected for all unwanted influences of the measurement setup, see Sec. 5.1. The corrected data is divided into frequency bins of 1 GHz. This should ensure (i) a sufficiently large data sample for

[5] In the VWZ expression, Eq. (5.9), and the FSS model, Eq. (5.13), the only time dependence is found in the exponential functions. Applying a Fourier transform is a multiplication with $\exp(2\pi i\,\varepsilon\,t)$ while integrating over ε. This results in a Dirac δ-function that can be used to eliminate one of the remaining integrals. Ultimately the total number of integrals is reduced by one.

a statistical treatment and (ii) nearly constant parameters T_a, T_b, τ_{abs} and D of the model.

- For each matrix element, S_{11}, S_{12}, S_{21} and S_{22}, the absolute square of the Fourier transform $|\tilde{S}_{ab}|^2$ is calculated. Due to the Wiener-Khinchin theorem [139]

$$\tilde{C}_{ab}(t) = |\tilde{S}_{ab}(t)|^2 \tag{5.15}$$

this equals, for infinite data sets, the Fourier transform $\tilde{C}_{ab}(t)$ of the auto-correlation function $C_{ab}(\varepsilon)$. The $S_{ab}(f)$ are only available with a resolution Δf. Therefore a discrete Fourier transform must be applied. This transform is explained in Appendix B and leads to Fourier coefficients $x_k = |\tilde{S}_{ab}(t_k)|^2$ and a discretized time t_k. The real and imaginary parts of the coefficients $\tilde{S}_{ab}(t_k)$ have an approximately Gaussian distribution [102], see also Sec. 5.8.1 for a discussion of this property.

- The x_k are statistically independent and follow a χ^2-distribution with two degrees of freedom,

$$q(x_k|\bar{x}_k) = 1/\bar{x}_k \, \exp\left(-x_k/\bar{x}_k\right) . \tag{5.16}$$

The expectation values $\bar{x}_k$ are given by the Fourier transform of $C_{ab}(\varepsilon)$ provided by the model. On a logarithmic scale, i.e. $y_k = \ln x_k$ and $\eta_k = \ln \bar{x}_k$, the distribution (5.16) reads [102]

$$P(y_k|\eta_k) = \exp\left(y_k - \eta_k - e^{y_k - \eta_k}\right) . \tag{5.17}$$

In this representation the width of $P(y_k|\eta_k)$ does not depend on η_k, see Fig. 5.13, wheres the width of $q(x_k|\bar{x}_k)$ changes with $\bar{x}_k$.

- The $\bar{x}_k$ depend on the parameters $\zeta = (T_a, T_b, \tau_{\text{abs}}, D)$ of the model. At least τ_{abs} cannot be determined experimentally. Based on the distribution (5.16) the joint probability distribution of the statistically independent x_k is

$$p(x|\zeta) = \prod_k q(x_k|\bar{x}_k(\zeta)) . \tag{5.18}$$

The parameters T_a, T_b and D are assumed to be given; the parameter τ_{abs} is to be inferred. A maximum likelihood fit estimates τ_{abs}.

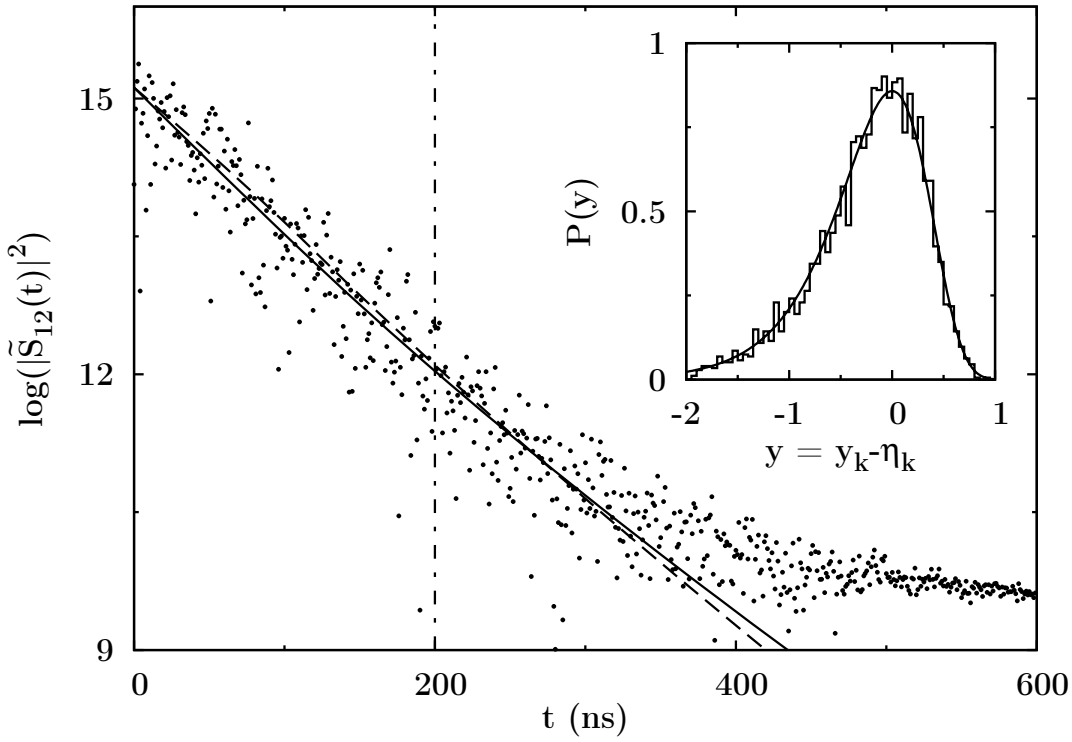

Fig. 5.13: Fourier transform $\tilde{S}_{12}(t)$ of a single realization in the range 16–17 GHz at $B = 190$ mT. See Fig. 5.12 for a representation the in frequency domain. The data (points) scatter around the VWZ (solid) and FSS (dashed) model predictions. All evaluations take only the time span up to 200 ns into account (dash-dotted vertical line) to avoid unwanted influences of noise. Inset: Experimental distribution of $\log(|\tilde{S}_{12}(t)|^2)$ around its mean value (histogram) and expected distribution (solid) from Eq. (5.17).

The analysis of the Fourier coefficients is illustrated in Fig. 5.13. It shows the data of Fig. 5.12 transformed into the time domain. The graph displays $\tilde{S}_{12}(t)$ on a logarithmic scale[6]. The data scatter around the mean η_t with constant spread, a consequence of statistically independent x_k following the distribution (5.17). After 400 ns the behavior of a nearly exponential decay drastically changes. At that time the signal has decayed 5 to 6 orders of magnitude and dropped below a constant, inevitable noise level. This noise corresponds to a low background noise in the measured frequency spectra and is mainly due to thermal noise in

[6]Throughout this work $\log(\cdot)$ is the logarithm to base 10, while $\ln(\cdot)$ denotes the natural logarithm.

the coaxial cables. At higher excitation frequencies the decay of the correlations is faster (Γ_{corr} increases with frequency) and the crossover to a noise influenced regime happens at earlier times. Thus an evaluable time frame 0–200 ns is defined in which all frequency ranges can still be analyzed without additional contributions due to noise. At early times the data points indicate a nearly exponential decay—an exactly exponential decay would be predicted by Eq. (5.7). The overall curvature of the data band indicates that advanced models such as VWZ (solid curve) and FSS (dashed curve) are really required. However, the best fits differ only slightly. The decision which one, if any, describes the data cannot be made just by looking at Fig. 5.13. In consequence, a statistical test is needed to come to a decision. The *goodness of fit* (GOF) test presented in the next section will provide the tool to arrive at such statements. The inset illustrates the distribution of the data points around their mean η_t. It is skewed in agreement with Eq. (5.17), a point to be further pursued in Sec 5.8.1. This non-Gaussian distribution prevents the usage of a standard χ^2-test. A GOF test needs to address the special properties of the distribution at hand [102].

5.7 Goodness of fit test

In the previous section it has been argued that (i) a GOF test is required and that (ii) the non-Gaussian distribution of the y_k prevents the application of the usual χ^2-test.

Based on the distribution Eq. (5.16), it is shown in App. C.1 that the function

$$d(y_k|\eta_k(\zeta)) = \frac{1}{\gamma}\left(e^{y_k-\eta_k} - (y_k - \eta_k) - 1\right) \tag{5.19}$$

quantifies the deviation between the data y_k and the predicted η_k. Here, $\gamma \approx 0.5772$ is Euler's constant. The expression d is positive definite; it is a function of the difference $y_k - \eta_k$; is zero exactly if $y_k = \eta_k$; and its expectation value is unity. Hence it fulfills all requirements of a distance value. Equation (5.19) is not symmetric with respect to $\eta_k(\zeta)$. It weights positive and negative deviations of y_k from the mean η_k differently and thus accounts for the skewed distribution (5.17).

Averaging over all m data points, one obtains the expression

$$d_\Sigma = \frac{1}{m} \sum_{k=0}^{m-1} d(y_k|\eta_k(\zeta)) \tag{5.20}$$

which replaces the usual χ^2-test expression. The distribution of d_Σ allows to judge the compatibility between the data and the model under test.

In a traditional χ^2-test the probability P to get a χ^2 value smaller than the experimental one, $\chi^2_{\rm exp}$, under the assumption of a valid model description is calculated. A threshold is defined, say 0.9, and if the calculated probability $P(\chi^2_{\rm exp})$ is above the threshold, the assumption is rejected, see the lower panel of Fig. 5.14. The chance of having erroneously rejected the model is one minus the threshold, 0.1 in the example.

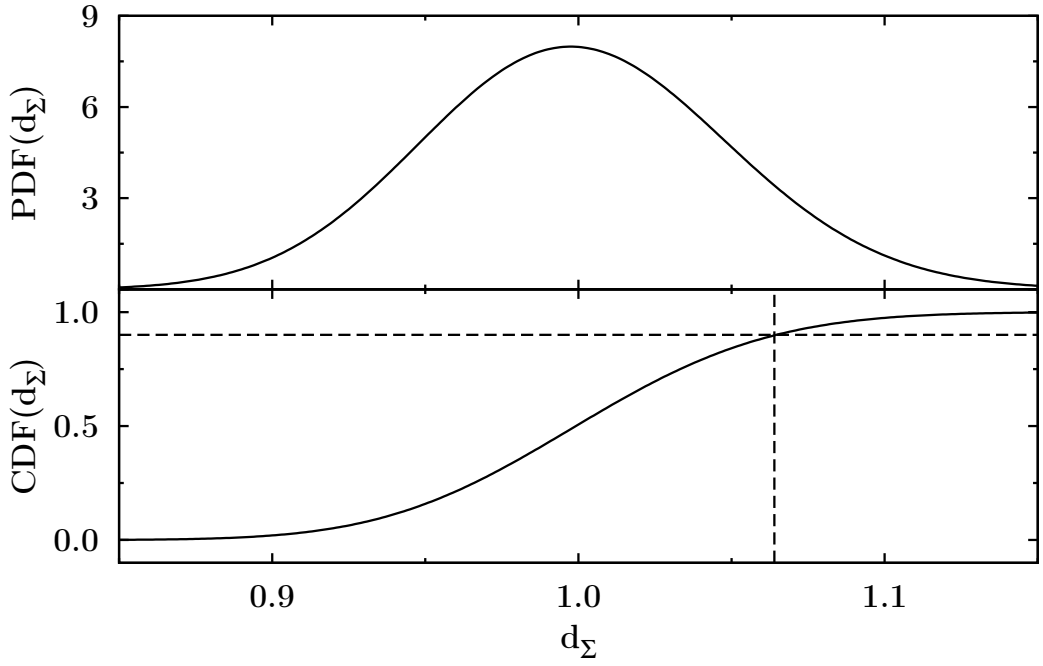

Fig. 5.14: The probability distribution function (PDF, upper panel), see Eq. (5.22), and the cumulative distribution function (CDF, lower panel) of the distance value d_Σ for $m = 800$ data points. For a threshold of 0.9 the CDF imposes a limit (dashed lines) of 1.064 on d_Σ which may not be exceeded if the GOF test is to accept the model.

The probability density function (PDF) of d_Σ is derived in App. C.3. Its exact expression (C.27) cannot be evaluated analytically. However, a χ^2-distribution with m degrees of freedom

$$\chi^2_m(\xi) = \frac{1}{(\frac{m}{2}-1)!}\left(\frac{m}{2}\right)^{\frac{m}{2}}\,\xi^{\frac{m}{2}-1}\,e^{-\frac{m}{2}\,\xi}\,, \tag{5.21}$$

serves as a reasonable approximation. The agreement between

$$\mathrm{PDF}(d_\Sigma) \simeq \chi^2_m(d_\Sigma) \tag{5.22}$$

and Eq. (C.27) is better than 2 %. Numerical simulations confirm the applicability of Eq. (5.22). Figure 5.14 shows for $m = 800$ the PDF and the cumulative distribution function (CDF) of d_Σ.

The above derivation of d_Σ holds for the analysis of single realizations as reported in [49, 102]. However, the analysis in Sec. 5.8 will show that the data of a single realization do not allow to distinguish between the fluctuations of $\mathcal{T}$ invariant and $\mathcal{T}$ broken systems. To this end the ensemble measurements introduced in Sec. 5.1 have to be performed and analyzed. Accordingly, the ensemble average of the basic quantity to be analyzed, $\tilde{C}(t) = |\tilde{S}(t)|^2$, is performed. New average Fourier coefficients

$$x_k^{(n)} = \overline{|\tilde{S}_{ab}(t_k)|^2}^{(n)}\,, \tag{5.23}$$

where $\bar{\cdot}^{(n)}$ denotes averages over n realizations, are defined. They are accompanied by a modified version of Eq. (5.16) and, in consequence, a new version of d_Σ, Eq. (5.20). The detailed derivations are elaborated in Appendix C.2 and show that the $x_k^{(n)}$ follow a χ^2-distribution (5.21) with $2n$ degrees of freedom

$$\begin{aligned} q^{(n)}(x_k^{(n)}|\bar{x}_k) &= \frac{1}{\bar{x}_k}\,\chi^2_{2n}\left(\frac{x_k^{(n)}}{\bar{x}_k}\right) \\ &= \frac{1}{\bar{x}_k}\,\frac{n^n}{(n-1)!}\left(\frac{x_k^{(n)}}{\bar{x}_k}\right)^{n-1}\,\exp\left(-\frac{n\,x_k^{(n)}}{\bar{x}_k}\right)\,. \end{aligned} \tag{5.24}$$

The factor n in the exponential reduces the variance of the distribution with increasing n, as expected. The distance function, Eq. (5.19), is replaced by

$$d^{(n)}(y_k^{(n)}|\eta_k(\zeta)) = \frac{\exp\left(y_k^{(n)}-\eta_k(\zeta)\right) - \left(y_k^{(n)}-\eta_k(\zeta)\right) - 1}{\ln n - \psi(n)}\,, \tag{5.25}$$

where $y_k^{(n)} = \ln x_k^{(n)}$ and $\psi(n)$ is the logarithmic derivative of the gamma function, $\psi(n) = \Gamma'(n)/\Gamma(n)$. The summation of $d^{(n)}$ over m data points leads to

$$d_\Sigma^{(n)} = \frac{1}{m} \sum_{k=0}^{m-1} d^{(n)}(y_k^{(n)}|\eta_k(\zeta)) \,. \tag{5.26}$$

The PDF of $d_\Sigma^{(n)}$ is again given to very good approximation by Eq. (5.22). This distribution does *not* depend on the number of realizations n, the only dependence is the number of data points m. Thus the graphs shown in Fig. 5.14 are valid for a GOF test with any number of realizations, as long as it includes 800 data points. This does not contradict an increased discriminatory power of the GOF test for higher n. In Eq. (5.25) for equal differences $y_k^{(n)} - \eta_k(\zeta)$ the denominator decreases for higher n and thus increases the distance $d^{(n)}$. This leads to a "quicker" rejection of the test.

The applicability of the GOF test stands and falls with the assumption that the Fourier coefficients $\tilde{S}$ have a Gaussian distribution in the sense that both, $\mathrm{Re}\{\tilde{S}\}$ and $\mathrm{Im}\{\tilde{S}\}$, follow this distribution. This is by no means trivial and will be further discussed in Sec. 5.8.1.

5.8 Analysis

The analysis of the data of Sec. 5.1 has been a three-step process. First, the assumption of Gaussian distributed, statistically independent Fourier coefficients $\tilde{S}$ is verified in Sec. 5.8.1. Second, details of the fit and the GOF test for the analysis of single and multiple realizations are elaborated in Sec. 5.8.2. Finally, the GOF test is applied in Sec. 5.8.3 in order to judge the applicability of the VWZ and FSS models.

5.8.1 Distribution of Fourier coefficients

This section shall establish that (i) the x_k follow an exponential distribution as assumed in Eq. (5.16), which is equivalent to a Gaussian distribution of $\mathrm{Re}\{\tilde{S}_{ab}\}$ and $\mathrm{Im}\{\tilde{S}_{ab}\}$, and that (ii) they are statistically independent.

Both tasks deal with the scatter of the data with respect to the expectation value. The time dependence of the expectation value has to be eliminated in order to get a sample of comparable data points. Looking at Fig. 5.13 one possibility to make x_k stationary is to take the VWZ or FSS model curves as the mean values and to remove these. However, the models were fitted to the data, using a fitting procedure that takes the distribution (5.16) of x_k already for granted; a circular argument. The global time dependence needs to be removed without imposing any restrictions on the data. A natural way to achieve this is to derive the mean from the data themselves. A sliding average over 45 data points (that is 45 ns) determines the mean $\overline{x}_k$ which is then removed from the data by considering the ratio $x_k/\overline{x}_k$. While this method is not completely devoid of assumptions—a smooth secular variation is presupposed—it is not biased toward VWZ.

The result is exemplified in Fig. 5.15. Part (c) demonstrates that the absolute squares $|\tilde{S}_{12}|^2$ scatter according to the distribution $P(x) = e^{-x}$ around their mean. The same holds for the data from reflection measurements, $|\tilde{S}_{11}|^2$ and $|\tilde{S}_{22}|^2$. The agreement seen in Fig. 5.15c can be further substantiated by the statistical test [140] described in Appendix D. Given N events x_k that follow an exponential distribution

$$p(x_k) = e^{-x_k}\,, \tag{5.27}$$

the ratio of the second moment to the square of the first moment is

$$\frac{\overline{x_k^2}}{\overline{x_k}^2} = 2\,. \tag{5.28}$$

Due to the finite data set, the averages in Eq. (5.28) are not directly accessible; instead on estimates them with

$$M_1 = \frac{1}{N}\sum_{k=1}^{N} x_k, \quad M_2 = \frac{1}{N}\sum_{k=1}^{N} x_k^2 \tag{5.29}$$

The variance of the ratio M_2/M_1^2 is then

$$\overline{\left(\frac{M_2}{M_1^2} - 2\right)^2} = \frac{9}{N}\,. \tag{5.30}$$

Evaluation of the ratio for the data $|\tilde{S}_{12}|^2$ in the range 16–17 GHz (see Fig. 5.15) with 6 realizations gives $M_2/M_1^2 = 1.97$, which is within the defined error limits

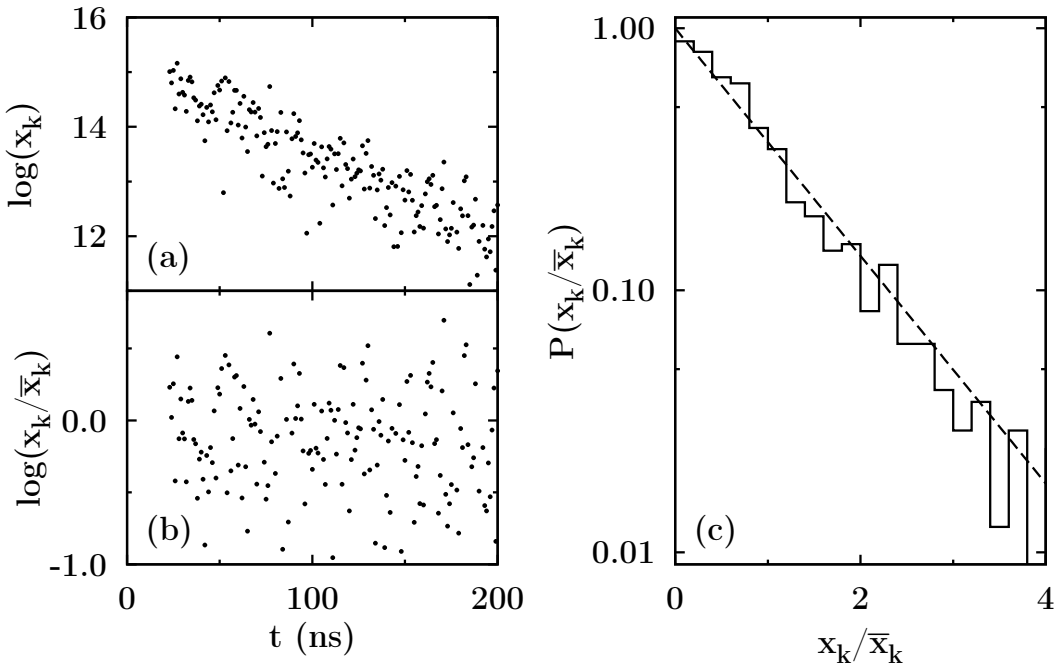

Fig. 5.15: Distribution of Fourier coefficients $x_k = |\tilde{S}_{12}|^2$ in the range 16–17 GHz. Figure (a) displays the data of Fig. 5.13. The x_k are made stationary in (b) by division through the mean as determined by a sliding average over 45 ns (which is why the first data point is at 23 ns). In this logarithmic scale, they scatter around zero. Figure (c) shows the distribution of the stationary coefficients on a logarithmic scale, now including the data from all 6 available realizations. One observes an exponential distribution (dashed line). The phases of $\tilde{S}_{12}$ are uniformly distributed (not shown).

(2 ± 0.09) for the $N = 6 \cdot 200 = 1200$ contributing data points. A systematic analysis of all available frequency ranges (1–25 GHz, i.e. 24 intervals) of this data ensemble yields 13 accepted and 11 rejected ratios, i.e. 54 % of all frequency ranges are within the 1-σ range defined by Eq. (5.30). In the range 10–25 GHz the acceptance ratio increases to 80 %, which is well above the expected 1-σ value of approximately 68 %. Finally, it has been checked that the phases of $\tilde{S}_{ab}$ are equally distributed, the final ingredient needed for a confirmation of the Gaussian distribution of the scattering matrix elements.

To check whether the x_k are uncorrelated, the autocorrelation coefficients of the stationary x_k have been calculated. If the autocorrelation is normalized

in such a way as to yield 1 for completely correlated data, the autocorrelation coefficients of x_k scatter evenly in the range 0.00 ± 0.05. This is in accordance with the assumption of uncorrelated Fourier coefficients.

In summary, it could be demonstrated that the Fourier coefficients x_k are indeed statistically independent "random" variables and follow an exponential distribution with high precision—or at least that the actual distribution cannot be discerned from an exponential one, a topic to be treated in more detail in Sec. 6.4.1. These results legitimate the application of the maximum likelihood fit presented in Sec. 5.6 and ensure the significance of the GOF test developed in Sec. 5.7.

5.8.2 Details on the fit and test procedures

The previous section established the validity of the developed fitting and testing procedures. The present section starts from the earlier considerations on the maximum likelihood fit and the GOF test, see Sec. 5.6 and Sec. 5.7, respectively and explains how measurements of different realizations are to be treated to test the VWZ and FSS models.

Maximizing the likelihood Eq. (5.18) is identical to minimizing the distance Eq. (5.20). For analyses of ensemble measurements, Eq. (5.26) is needed. The distance value depends on the Fourier coefficients from the experiment y_k and their predicted values from theory $\eta_k(\zeta)$, where ζ represents the model parameters. To be more precise, all evaluations solely depend on the difference $y_k - \eta_k(\zeta)$. Accordingly, the fitting method developed in Ref. [49] calculates for each y_k and for a trial parameter set ζ_{try} this difference and evaluates the distance value d_Σ. The computer algebra system *Mathematica* is used to minimize d_Σ and to return the optimal ζ_{fit}. The minimization method is a derivative-free algorithm (the principal axis method of Brent [141]) which determines a local minimum; a more effective method relying on the evaluation of derivatives cannot be applied since $\eta_k(\zeta)$ involves the full VWZ or FSS expressions. The y_k comprise the Fourier transformed data of the full 2×2 S-matrix, as the models make imperative predictions for all 4 accessible matrix elements. The time range is determined by the losses of the system. While Friedrich [49] could use the Fourier coefficients up to 800 ns, the present analyses go only up to 200 ns due to increased losses by

a thinner cavity and the presence of the ferrite. Additionally, the first 4 ns are dropped. They include secular variations of the data on large frequency scales that could not be corrected by the applied recalibration procedures and differ in their behavior significantly from the model predictions. The size of the initial frequency windows of 1 GHz sets the time resolution to $t_{k+1} - t_k = 1$ ns. Thus, the four S-matrix elements of a single realization contribute $4 \cdot 196 = 784$ data points to d_Σ. This number determines, for a single realization, on the discriminatory power of the GOF test. For the test a threshold of 0.9 is defined and the acceptance limit of d_Σ determined, see Fig 5.14. A comparison of d_Σ for the fitted parameter set ζ_{fit} to the threshold value finally decides upon acceptance or rejection of the chosen model.

In a first run each realization of the ensemble measurement has been analyzed independently, using Eq. (5.20) for the GOF test, with τ_{abs} as a single fit parameter. However, due to the similarity of the VWZ and FSS predictions (see Fig. 5.13) both models were accepted and no conclusions could be drawn. Of course, in measurements without a ferrite the VWZ model usually resulted in lower d_Σ values, but as long as the FSS model does not yield values above the rejection threshold, no judgment in favor of VWZ can be rendered.

Thus for the investigation of the impact of TRSB a single measurement carries too little information about the dynamics of the system. This makes investigations of ensembles of data, see Sec. 5.1, mandatory. For the analysis of these data the obvious method is to construct ensemble averages $x_k^{(n)} = \overline{x_k}$ for each time point[7]. The fitting procedure then tries to find a *single* parameter set ζ_{fit} to describe the averaged data and the GOF test decides on the degree of agreement, both steps utilizing $d_\Sigma^{(n)}$ from Eq. (5.26).

Using this approach, the discriminatory power can be tuned by a variation of n, the number of realizations used in the averaging process. Each additional realization reduces the scatter of the data, in the limit $n \to \infty$ the measurements would yield the expectation value η_k directly without ambiguity. At this stage both models, VWZ and FSS, would be rejected by the GOF test and rightly so; every ever so tiny deviation of the experiment from the preconditions of those

[7]Note that the average is performed in linear scale, i.e. one considers $\overline{x_k}$ and not $\overline{y_k}$, as this is the observable of interest to the theory, while the switchover to the logarithmic scale is purely motivated by the method of analysis.

RMT based models would become evident and, in consequence, the models could not be accepted as a description of the physical reality. This consideration is to demonstrate the power of experimental ensemble measurements—the adjustment of the degree of precision on which a model is to be tested against the experiment.

However, the following discussion will establish, that the method of simply analyzing averages $x_k^{(n)}$, as described above, does not work. Moving the scatterer inside the cavity does not result in a statistically independent realization of *exactly* the same system. Instead, the important parameters, T_1, T_2, τ_{abs} and the $\mathcal{T}$ breaking effect of the ferrite, are slightly altered, too. This is because along with the position of the scatterer the mode structure inside the cavity changes as well, causing small variations of these parameters. In consequence, the $x_k^{(n)}$ cannot precisely be described by a single parameter set ζ. Now, from experience, at about 6 included realizations the analysis becomes sufficiently precise to tell spectra described by VWZ or FSS apart. However, at the same time the GOF test also becomes sensitive to slight changes of the model parameters and, accordingly, rejects all fits.

A solution to this dilemma is a different treatment of the ensemble[8] data. Instead of trying to describe an averaged data set with a *single* parameter set $\zeta = (T_a, T_b, \tau_{\mathrm{abs}})$, a model function is fitted to *each* realization data set, each yielding an adjusted parameter set $\zeta^{(1)}, \ldots, \zeta^{(n)}$. Then, for each realization i, the difference ${y_k}^{(i)} - \eta(\zeta^{(i)})$ is calculated. If the data are described by the model, the result should fluctuate around 0 with a distribution given by Eq. (5.17), with a result similar to Fig. 5.15b. In this stationary representation all realizations should now be equivalent and the ensemble average

$$y'_k = \ln\left(\overline{\exp\left[{y_k}^{(i)} - \eta(\zeta^{(i)})\right]}\right) , \tag{5.31}$$

again the average is done in linear scale, can be performed. The GOF test now checks the compliance of y'_k with the distribution (C.17) centered around zero.

[8] In a strict sense the obtained set of realization measurements does not define an ensemble, because the parameters of a true ensemble may not, but for statistical fluctuations, change. However, the available data are as close to a true ensemble as experimentally possible and will therefore be denoted as such.

5.8.3 GOE and GUE based models under test

First, the case of the tilted stadium billiard *without* a ferrite is addressed. This links the new procedures discussed in the preceding section with known results [102] and provides a basis for the analyses of setups with ferrite and TRSB. The ensemble data comprise 6 realizations and are taken in the frequency range of 1–25 GHz. For the analysis frequency windows of 1 GHz are taken. They are transformed into the time domain where the time range 5–200 ns of S_{11}, S_{22} and S_{12} are considered; without a ferrite, reciprocity holds and S_{21} does not contain new information. In a first step, the fit determines for each realization and for the VWZ and FSS models independently optimal values of the transmission coefficients T_1, T_2 and τ_{abs}, the latter one being divided into 298 absorptive channels. Afterward, for the averages (5.31) the GOF test accepts or rejects the two models with a threshold for the cumulative distribution function $\mathrm{CDF}(d_\Sigma^{(6)}) < 0.9$, that is a 10 % chance of erroneously rejecting a model prediction. The individual results are summarized in Tab. 5.1.

Tab. 5.1: GOF test results of empty billiard. The first row is the *lower* boundary of the 1 GHz frequency interval used for the analysis. The second (third) row indicates an accepted GOF test of the VWZ (FSS) model by a "•". If both models are accepted, no conclusions can be drawn and the column is marked by "∘" signs. Rejected fit results are denoted by "–". In summary, the data are in good agreement with the VWZ model of a $\mathcal{T}$ invariant system.

f (GHz)	1	2	3	4	5	6	7	8	9	10	11	12	13	14	15	16	17	18	19	20	21	22	23	24
VWZ	–	•	∘	•	∘	•	•	•	•	•	•	•	•	•	•	•	–	–	•	•	–	•	•	–
FSS	–	–	∘	–	∘	–	–	–	–	–	–	–	–	–	–	–	–	–	–	–	–	–	–	–

Below 5 GHz the significance of the results is low. There, the level spacing D is more than 40 MHz and, in consequence, the spectra contain less than 25 resonances per GHz. In between these few resonances, the spectra are dominated by the background noise of the VNA which is, of course, not described by RMT models. At 17, 18, 21 and 24 GHz (denoting the lower boundary of the frequency

interval) the VWZ model is barely above the acceptance threshold while the FSS model is always rejected. This is in accordance with the results presented in Ref. [102]. The VWZ model is in very good agreement with the data taken on a fully chaotic, $\mathcal{T}$ invariant microwave resonator. The FSS model is ruled out.

Now, the microwave billiard with ferrite and an external magnetic field is treated. The data were taken with field strengths B of about 170, 190, 220 and 340 mT. In the sequel, only $B = 190$ mT is discussed in detail, the results for the other field strengths are analogous. The analysis of the 6 available realizations is performed in the same way as for the data without ferrite. There is one difference, of course: Now S_{21} differs from S_{12}. Therefore all four S-matrix elements must be considered in the analysis. The results are gathered in Tab. 5.2.

Tab. 5.2: GOF test results of the billiard with ferrite and $B = 190$ mT. The symbols are used as in Tab. 5.1. The intervals starting at 15 and 16 GHz are described by the FSS model for systems with complete TRSB.

f (GHz)	1	2	3	4	5	6	7	8	9	10	11	12	13	14	15	16	17	18	19	20	21	22	23	24
VWZ	–	○	●	○	○	○	○	●	●	●	●	–	●	–	–	–	–	–	–	●	●	–	–	–
FSS	–	○	–	○	○	○	○	–	–	–	–	–	–	–	●	●	–	–	–	–	–	–	–	–

Again, for low frequencies the significance of the analysis is low. Due to large level spacings only a few resonances contribute to the statistical ensemble and no clear picture arises from 6 realizations. However, above 8 GHz the results are reliable: In many frequency intervals the VWZ model provides an acceptable description of the experimental data, in the ranges 15–16 GHz and 16–17 GHz only the FSS model is applicable. In eight intervals (above 8 GHz) both models fail. This behavior is attributed to a variation of the TRSB impact of the ferrite. In the regions described by VWZ, the TRSB effect of the ferrite is so small that VWZ holds. Between 15 and 17 GHz, the induced TRSB is strong enough for the GUE to apply. Where neither VWZ nor FSS describe the data, the degree of TRSB is significant enough to invalidate VWZ but not strong enough to favor FSS. In these cases the chaotic dynamics corresponds neither to a GOE nor to a GUE system, instead it is a *mixed* GOE/GUE one. These results call for a theory of partial $\mathcal{T}$ breaking. This issue is addressed in Sec. 6.

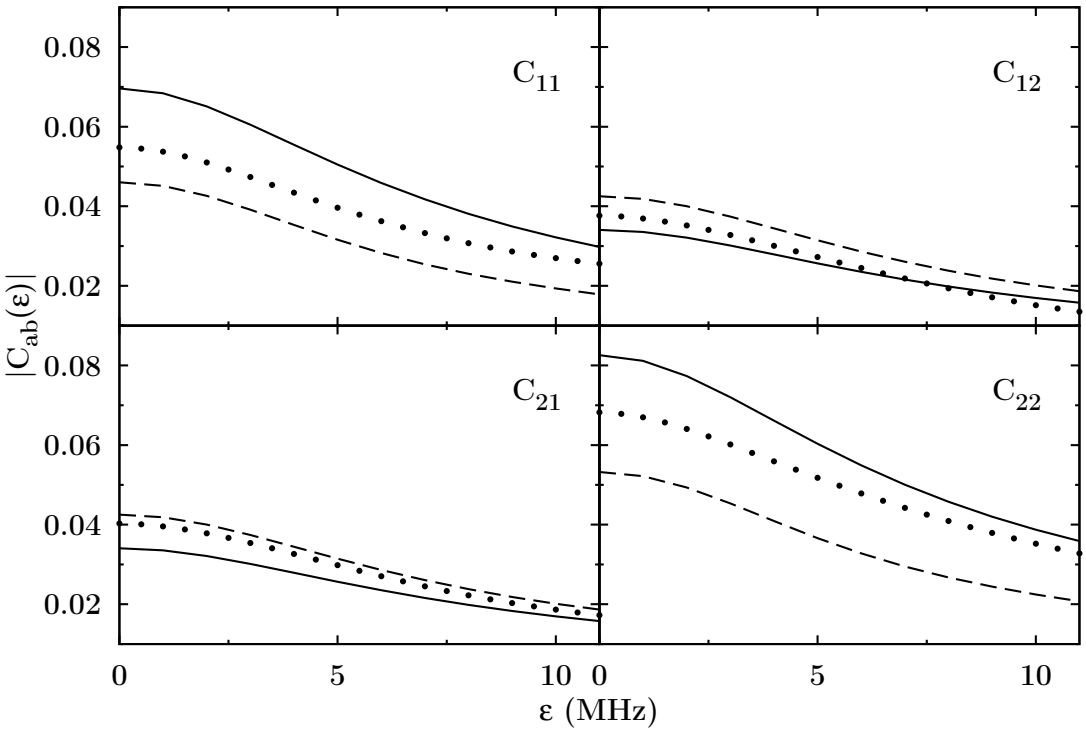

Fig. 5.16: Comparison of autocorrelation functions for a single realization in the frequency range of 16–17 GHz and for $B = 190$ mT. The four panels display the results for C_{11}, C_{12}, C_{21}, C_{22}. The shape of the data (dots) is reasonably approximated by the FSS model (dashed) while the slope predicted by the VWZ model (solid) is wrong.

The situation in the range of 16–17 GHz in the frequency domain is shown in Fig. 5.16. For these data, the GOF test only accepts the FSS model. Indeed, the slope of the data points is much better reproduced by the FSS description than by VWZ. However, both models predict the mean value wrongly. The mean is described by the Fourier coefficient x_0 at $t = 0$, which is within the first Fourier coefficients excluded from the fit. At the same time the mean value is poorly determined by the data. According to Weyl's formula Eq. (5.2) about 116 resonances are in the chosen frequency range. This gives rise to sizable FRD errors that cannot be neglected. Neighboring points of the autocorrelation function in the frequency domain are not independent from each other. As $C_{ab}(0) = \langle |S_{ab}|^2 \rangle$ is also affected by FRD errors, the whole data curve may be either shifted up or down. Therefore the slope of the curves, which is much better described by FSS,

is a more reliable property of the curves than their mean.

In summary, the GOF test presented in Ref. [102] has successfully been extended to be applied to ensemble data, increasing the sensitivity of the analysis as desired. Measurements of microwave billiards without ferrite confirm the earlier agreement with VWZ for time-reversal invariant systems. A magnetized ferrite breaks this symmetry and, accordingly, VWZ does not provide a valid description of the data any more. Instead, agreement between the fluctuating properties of the scattering matrix elements and a model description based on the GUE has been demonstrated for the first time. However, this agreement has only been confirmed in a very small frequency range. Obviously, in most frequency regions the data do not represent a pure GUE system but one corresponding to a mixed GOE/GUE system. Hence, the induced time-reversal non-invariance is not complete and further analyses need to establish the degree of symmetry breaking.

5.9 Cross-correlation function

A first approach towards a determination of the $\mathcal{T}$ breaking strength has been presented in Sec. 5.2 where the contrast function Δ, Eq. (5.3), is introduced. A more elegant and theoretically better understood approach is provided by the cross-correlation function

$$C_{12,21}(\varepsilon) = \langle S_{12}(f)\, S_{21}^*(f+\varepsilon)\rangle - \langle S_{12}(f)\rangle \langle S_{21}^*(f)\rangle \tag{5.32}$$

between S_{12} and S_{21}^*. The two limiting cases of the normalized cross-correlation function at $\varepsilon = 0$

$$C_{\mathrm{cross}} = \left| \frac{\langle S_{12}(f)\, S_{21}^*(f)\rangle \quad - \langle S_{12}(f)\rangle \langle S_{21}^*(f)\rangle}{\sqrt{\langle |S_{12}(f)|^2\rangle \langle |S_{21}(f)|^2\rangle} - \langle S_{12}(f)\rangle \langle S_{21}^*(f)\rangle} \right| \tag{5.33}$$

are

$$C_{\mathrm{cross}} = \begin{cases} 1 & \text{for GOE} \\ 0 & \text{for GUE} \end{cases} \tag{5.34}$$

and readily understood. For a GOE system reciprocity holds, i.e. $S_{12} = S_{21}$. In the case of a GUE system the symmetry breaking is complete and the spectra of

S_{12} and S_{21} are completely unrelated (see Ref. [79] for a treatment of the two-level case).

Figure 5.17 shows C_{cross} for the data with $B = 190$ mT. The data confirm that the induced time-reversal symmetry breaking is not complete as C_{cross} never approaches zero; no values below 0.4 are observed. A comparison of the results for the VWZ and FSS models in Tab. 5.2 to the values obtained for C_{cross} corroborates the significance of the cross-correlation function. The GOF test accepts FSS only in the intervals 15–16 and 16–17 GHz, where C_{cross} has a deep minimum. In addition, the test rejects VWZ for cross-correlations less than about 0.9. A detailed discussion of the positions and the values of the minima visible in Fig. 5.17 is postponed to Sec. 6.2.

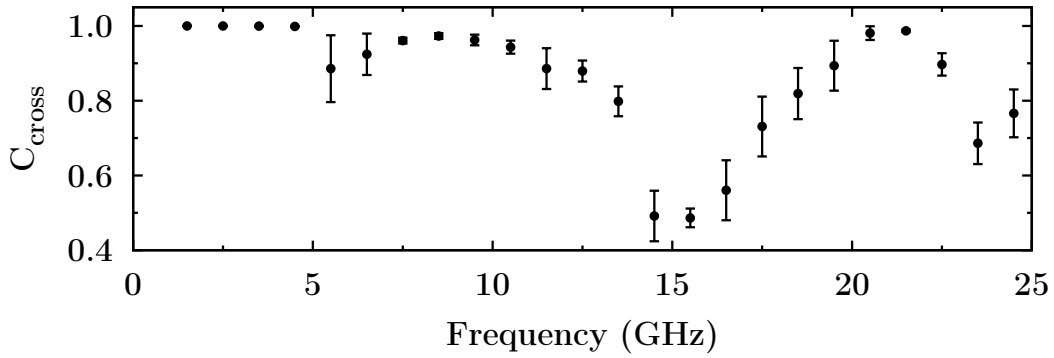

Fig. 5.17: Normalized cross-correlation C_{cross} for the data with ferrite and $B = 190$ mT. In each frequency interval C_{cross} was evaluated for 6 realizations resulting in mean values (points) and a standard deviations (error bars). Note the suppressed-zero scale.

The analysis of the cross-correlation function proves that the induced TRSB is incomplete. The cross-correlation values give, however, only a qualitative understanding of the $\mathcal{T}$ breaking strengths. For a quantitative understanding of the data an extended model, to be introduced in Sec. 6, is required to describe cross- and autocorrelation functions in the regime of partial time-reversal symmetry breaking.

6 Model for partial time-reversal symmetry breaking

The tests of the VWZ and FSS models and the study of the cross-correlation function presented in the preceding section emphasized the need for a model to describe systems with partial TRSB. Partial breaking of symmetries is since long an active field in physics. For example the breaking of isospin symmetry [142–144], the effects of symmetries on resonance strength distributions [89] and spectral properties [88, 145] and, of course, effects of a partially broken time-reversal symmetry [146–149], albeit only theoretically, have already been investigated.

The basic idea to model a partially broken symmetry is always the same. A parameter is introduced into the Hamiltonian of the system to model the transition between a fully conserved and a fully broken symmetry (see, e.g. Ref. [85, 88]). In RMT a suitable approach for the Hamiltonian of a chaotic system with partial TRSB is

$$H = H^s + i\,\alpha\,H^a\,, \quad 0 \leq \alpha \leq 1\,, \tag{6.1}$$

where H^s is a symmetric random matrix taken from the GOE and H^a is fully antisymmetric such that for $\alpha = 1$ the matrix H is a member of the GUE. (That is, ansatz (6.1) follows Eq. (4.5) used in the case of isolated resonances.) The parameter α describes the strength of the $\mathcal{T}$ breaking matrix elements. For $\alpha = 0$ the matrix H models a $\mathcal{T}$ invariant chaotic system, for $\alpha = 1$ a system with fully broken time-reversal symmetry is realized and for intermediate values of α the $\mathcal{T}$ invariance is only partially violated. While α is an essential quantity and of basic interest in theoretical considerations, the parameter of relevance to the experiment is the $\mathcal{T}$ *breaking strength*

$$\lambda = \frac{\alpha\,v}{D}\,. \tag{6.2}$$

Here, D denotes the mean level spacing and v the root-mean-square of the matrix elements of H^a. For simplicity and without loss of generality $v = 1$ is assumed for the further model considerations. The definition of λ is the equivalent to that of ξ given in Eq. (4.6) used to measure the $\mathcal{T}$ breaking strength on pairs of nearly degenerate resonances as presented in Sec. 4.3. The scaling of λ by D in Eq. (6.2) has already been exploited in Sec. 5.2. There, at high excitation

frequencies both, α and D, were small. Thus λ stayed sufficiently large to induce a noticeable violation of reciprocity, cf. Fig. 5.8. The $\mathcal{T}$ breaking strength is connected to the spreading width [128, 142, 144] via $\Gamma^{\downarrow} = 2\pi\,\alpha^2\,v^2/D = 2\pi\,\lambda^2\,D$.

For further analyses of S-matrix fluctuations in the regime of partial TRSB, a newly developed model to describe autocorrelation and cross-correlation functions is introduced in Sec. 6.1. Based on this model, the $\mathcal{T}$ breaking strengths are extracted from the data in Sec. 6.2 and then a comparison of the new model to the established VWZ and FSS models is carried out in Sec. 6.3. In Sec. 6.4 the "elastic enhancement factor" is introduced and the effect of partial TRSB on this enhancement mechanism is investigated.

6.1 Model derivation

In 1984, the seminal work of Verbaarschot *et al.* [48] computed the two-point correlation functions for the elements of the S-matrix modeling chaotic scattering systems with $\mathcal{T}$ invariance. Their calculations were based on the supersymmetry technique due to Efetov [123] from condensed matter theory. About ten years later, in 1995, their methods were extended by Pluhař *et al.* [148] to systems with partial TRSB. Their concern was the study of the conductance. From these computations the autocorrelation function of the off-diagonal elements S_{ab} can be deduced. Using their ideas and the detailed guidance provided in Ref. [148] it is possible to generalize their results to autocorrelation functions for all S-matrix elements and with $\varepsilon \geq 0$. Additionally, even cross-correlation functions can be evaluated which will be essential in the determination of the $\mathcal{T}$ breaking strength.

In this section only the result of the calculations carried out by Dietz [150] will be given. To clarify the notation a couple of auxiliary definitions

$$\begin{aligned} \mathfrak{t} &= \pi^2\,\lambda^2 \\ \mathcal{R} &= 4\,(\mu+\mu_1)\,(\mu+\mu_2) \\ \mathcal{F} &= 4\,\mu\,(1-\mu) \\ \mathcal{U} &= 2\,\sqrt{\mu_1(1+\mu_1)\,\mu_2(1+\mu_2)} \end{aligned}$$

$$
\begin{aligned}
\mathcal{G} &= 2\mu_1\mu_2 + \mu_1 + \mu_2 + \mathcal{U} \\
\mathcal{H} &= 2\mu_1\mu_2 + \mu_1 + \mu_2 - \mathcal{U} \\
\tilde{A}_a &= \frac{(2 - T_a)\,\lambda_2 + T_a\,\lambda_1}{4\,(1 + T_a\mu_1)\,(1 + T_a\mu_2)} \\
\tilde{B}_a &= \frac{(2 - T_a)\,\lambda_1 + T_a\,\lambda_2}{4\,(1 + T_a\mu_1)\,(1 + T_a\mu_2)} \\
\tilde{C}_a &= \frac{1}{2}\,\frac{1}{1 - T_a\mu} \\
C_2 &= \frac{\mathcal{U}}{4}\left(\frac{1}{1 + T_a\mu_2}\,\frac{1}{1 + T_b\mu_1} + \frac{1}{1 + T_a\mu_1}\,\frac{1}{1 + T_b\mu_2}\right) \\
C_3 &= \frac{\mu\,(1 - \mu)}{(1 - T_a\mu)\,(1 - T_b\mu)} \\
\varepsilon_\pm &= 1 \pm \exp(-2\,\mathfrak{t}\,\mathcal{F}) \\
\lambda_0 &= 1 - 2\mu \\
\lambda_1 &= \sqrt{(1 + \mu_1)\,(1 + \mu_2) + \mu_1\mu_2 + \mathcal{U}} \\
\lambda_2 &= \sqrt{(1 + \mu_1)\,(1 + \mu_2) + \mu_1\mu_2 - \mathcal{U}}
\end{aligned}
\tag{6.3}
$$

are introduced. The parameter $\mathfrak{t}$ provides a rescaled measure of the $\mathcal{T}$ breaking strength. The definitions of $\lambda_{0,1,2}$ were introduced by Pluhař *et al.* as new integration variables for the recovery of the GOE result at $\mathfrak{t} = 0$. In the present work they are used throughout the whole range of $\mathfrak{t}$ values. The quantity λ_0 is not needed for the final result but is given for the sake of completeness. With these definitions the autocorrelation and cross-correlation functions can be written as

$$
\begin{aligned}
C_{ab}(\epsilon) &= \frac{T_a\,T_b}{16}\int_0^\infty \mathrm{d}\mu_1 \int_0^\infty \mathrm{d}\mu_2 \int_0^1 \mathrm{d}\mu\,\frac{|\mu_1 - \mu_2|}{\mathcal{U}} \\
&\quad \times \frac{1}{(\mu + \mu_1)^2}\,\frac{1}{(\mu + \mu_2)^2}\exp\left(-\frac{i\pi\epsilon}{D}(\mu_1 + \mu_2 + 2\mu)\right) \\
&\quad \times J_{ab}\cdot\prod_c \frac{1 - T_c\,\mu}{\sqrt{(1 + T_c\,\mu_1)\,(1 + T_c\,\mu_2)}}\,\exp\left(-2\,\mathfrak{t}\,\mathcal{H}\right)\,,
\end{aligned}
\tag{6.4}
$$

with

$$
\begin{aligned}
J_{ab} &= \Bigg\{\Bigg[\Bigg(\frac{1}{2}\,\frac{\mu_1(1 + \mu_1)}{(1 + T_a\mu_1)\,(1 + T_b\mu_1)} + \frac{1}{2}\,\frac{\mu_2(1 + \mu_2)}{(1 + T_a\mu_2)\,(1 + T_b\mu_2)} \\
&\quad + \frac{\mu(1 - \mu)}{(1 - T_a\mu)\,(1 - T_b\mu)}\Bigg)(1 + \delta_{ab}) \\
&\quad + 2\,\delta_{ab}\,\overline{S_{aa}}^2\left(\frac{\mu_1}{2(1 + T_a\mu_1)} + \frac{\mu_2}{2(1 + T_a\mu_2)} + \frac{\mu}{1 - T_a\mu}\right)^2\Bigg]
\end{aligned}
$$

$$\times \left[\mathcal{F}\,\varepsilon_+ + (\lambda_2^2 - \lambda_1^2)\,\varepsilon_- + 4\,\mathfrak{t}\,\mathcal{R}\,(\lambda_2^2\,\varepsilon_- + \mathcal{F}\,(\varepsilon_+ - 1))\right]$$
$$\pm\,(1-\delta_{ab})\,K_{ab}\Big\} + \{\lambda_1 \rightleftharpoons \lambda_2\} \tag{6.5}$$

and

$$\begin{aligned} K_{ab} \;=\; & \varepsilon_- \Big[2\,\mathcal{F}\Big\{(\tilde{A}_a\tilde{C}_b + \tilde{A}_b\tilde{C}_a)\,\mathcal{G}\lambda_2 + (\tilde{B}_a\tilde{C}_b + \tilde{B}_b\tilde{C}_a)\,\mathcal{H}\lambda_1\Big\} \\ & + 3\,C_3\,\mathcal{F} - C_2\,(\lambda_2^2 - \lambda_1^2) + C_2\,\mathfrak{t}\,\mathcal{R}\,(4\,\lambda_2^2 - 2\,\mathcal{F}) \\ & + 2\,\mathfrak{t}\,\mathcal{R}\,C_3\,\mathcal{F}\Big] \\ & + \left(\varepsilon_+ - \frac{\varepsilon_-}{\mathfrak{t}\,\mathcal{F}}\right)\Big[3\,C_3\,(\lambda_2^2 - \lambda_1^2) + \mathfrak{t}\,\mathcal{R}\,C_3\,(4\,\lambda_2^2 - 2\,\mathcal{F}) \\ & + 2\,\mathcal{F}\,\Big\{(\tilde{A}_a\tilde{C}_b + \tilde{A}_b\tilde{C}_a)\,\mathcal{G}\,\lambda_2 - (\tilde{B}_a\tilde{C}_b + \tilde{B}_b\tilde{C}_a)\,\mathcal{H}\,\lambda_1\Big\} \\ & + (2\,\mathfrak{t}\,\mathcal{R} - 1)\,C_2\,\mathcal{F}\Big]\,. \end{aligned} \tag{6.6}$$

The second term $\{\lambda_1 \rightleftharpoons \lambda_2\}$ in Eq. (6.5) is obtained by exchanging λ_1 and λ_2 in the first one. The "$\pm$" sign in the last row of Eq. (6.5) is to be understood as follows: The plus sign yields the autocorrelation function for $\varepsilon \geq 0$. The cross-correlation function $C_{12,21}(\epsilon = 0)$, see Eq. (5.32), is obtained by using the negative sign. The results have been verified to coincide with the known results for the cases of the GOE, $\alpha = 0$, and the GUE, $\alpha = 1$. For intermediate values, $0 < \alpha < 1$, numerical simulations confirmed the findings.

6.2 Time-reversal symmetry breaking strength

The analysis of the normalized cross-correlation function Eq. (5.33) in Sec. 5.9 established that $\mathcal{T}$ breaking is incomplete. The values of C_{cross} gave, however, only a qualitative understanding of the degree of TRSB. In contradistinction, the extended model allows for a quantitative understanding; it connects C_{cross} to the $\mathcal{T}$ breaking strength λ. With the ansatz Eqs. (6.1, 6.2) the analytic expression of C_{cross} obtained from Eq. (6.4) essentially depends only on the parameter λ. The dependence on $T_1, T_2, \tau_{\text{abs}}$ is negligible in the parameter range of relevance to the experiment. Figure 6.1 shows $C_{\text{cross}}(\lambda)$. At $\lambda \approx 1$, that is $\alpha \approx D$, TRSB is nearly complete and $C_{\text{cross}}(\lambda)$ is vanishingly small. Due to the slope of the curve

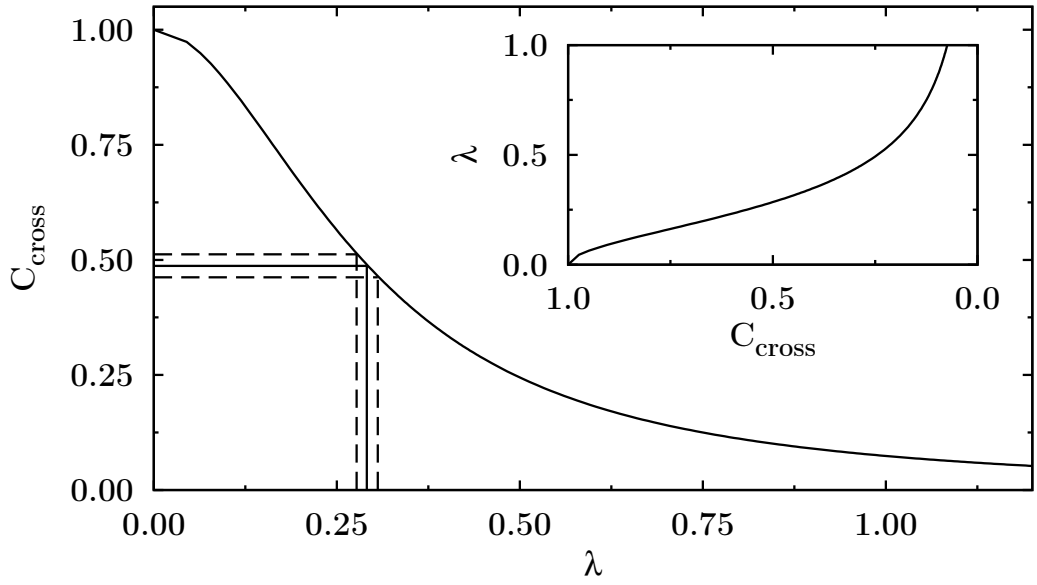

Fig. 6.1: Normalized cross-correlation (solid curve) as a function of λ. It starts at $C_{\rm cross}(0) = 1$ for a $\mathcal{T}$ invariant system and decreases for $\lambda > 0$. At $\lambda \approx 1$ the cross-correlation is nearly 0 and $\mathcal{T}$ symmetry breaking is mostly complete. The straight lines illustrate how $C_{\rm cross} = 0.49 \pm 0.07$, see Fig. 5.17 at 15–16 GHz, translates into $\lambda = 0.29 \pm 0.04$. The inset shows the inverted function, $\lambda(C_{\rm cross})$.

for $\lambda \lesssim 0.5$ a precise estimation of λ, given an experimental value of $C_{\rm cross}$, is possible (see the straight lines and the inset in Fig. 6.1).

For an external field of 190 mT the experimentally determined cross-correlation values and the extracted values of λ are presented in Fig. 6.2. With the mean level spacings D, obtained from Weyl's formula Eq. (5.2), the strengths of the $\mathcal{T}$ breaking matrix element α are given in units of the rms matrix element v of H^a. The graphs reveal a rich structure of the $\mathcal{T}$ breaking strength with three resonance like maxima. The first maximum with $\lambda \approx 0.08$ at 5–7 GHz can be directly attributed to the ferromagnetic resonance. At 190 mT it is located around 6.6 GHz, see Eq. (3.10). A strong and broad maximum at 14–16 GHz yields $\lambda = 0.29 \pm 0.04$. Interestingly, this value of λ is comparable to the maximum value of ξ observed for the second doublet (see Fig. 4.7) investigated in Sec. 4.3. In the measured frequency range there is a third maximum at 23–24 GHz, where $\lambda = 0.19 \pm 0.03$. The occurrence and positions of the second and third maxi-

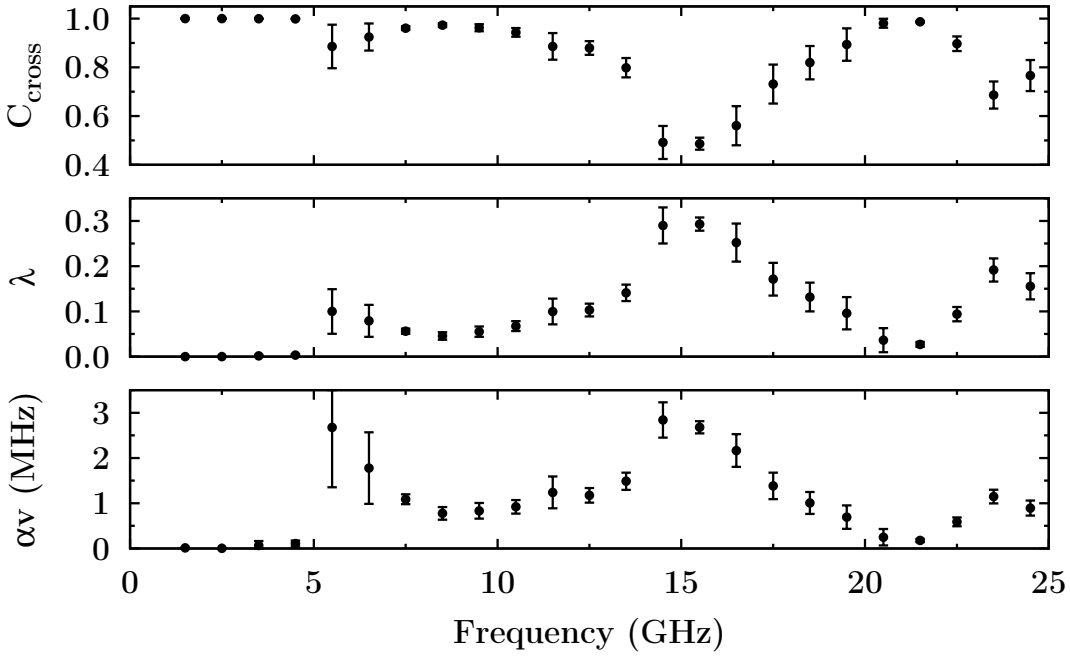

Fig. 6.2: Induced $\mathcal{T}$ breaking strength of the ferrite at 190 mT. The cross-correlation values are evaluated for intervals 1 GHz in size. The error bars indicate the variation of the obtained values over the 6 realizations, the points give their means. The top panel gives the experimentally determined C_{cross} values that are converted into λ in the middle panel. The bottom panel displays $\alpha\, v = \lambda\, D$.

mum cannot currently be explained. They are believed to be regions where the diminished influence of the ferromagnetic resonance is enhanced by standing rf magnetic fields inside the ferrite. However, hitherto this could not be confirmed. A further, more detailed discussion of this topic is postponed to Sec. 6.2.1.

It is interesting to note that at 5–6 GHz and at 14–15 GHz the values of $\alpha\, v$ are approximately of equal size, $\alpha\, v \approx 3$ MHz. In contradistinction, λ increases in the same frequency ranges threefold and goes from $\lambda \approx 0.1$ to $\lambda \approx 0.3$. Thereby, it is demonstrated that for a given size of the symmetry breaking matrix element the symmetry breaking effect increases with the level density. As a consequence the region of overlapping resonances is especially suitable for the investigation of $\mathcal{T}$ breaking effects.

6.2.1 Influence of ferrite position and size

The preceding section established $\mathcal{T}$ breaking strengths of $\lambda \lesssim 0.3$ for the experimental setup as presented in Sec. 5.1. The analysis suggests especially strong effects of TRSB induced by the ferrite in the frequency region around 6, 15 and 23 GHz. While the effect at 5–7 GHz can be understood in terms of the ferromagnetic resonance, the presence and positions of the other peaks is unexpected. The following discussion sheds some light on the connection between the properties of the ferrite and the resulting $\mathcal{T}$ breaking strengths λ.

With respect to the ferrite there are four parameters that can be changed in order to probe their influences on λ: The external magnetic field strength can be varied, the position of the ferrite within the cavity can be shifted, the geometry of the ferrite can be altered and its material can be replaced. All four options have been investigated experimentally, the results will be discussed in the following.

Variation of external magnetic field strength. The experiments with the cylindrical ferrite (4 mm in diameter) have been conducted at four field strengths $B = 170,\ 190,\ 220,\ 340$ mT. The results discussed in the preceding section are based on the data obtained for $B = 190$ mT. The field strength affects the position of the ferromagnetic resonance and, accordingly, the position of the first peak in λ (see Fig. 6.2) varies between roughly 5 and 9 GHz. Above approximately 11 GHz the values of λ are nearly independent of B. Most importantly, the maximal achievable value of λ is unaffected within this range of external magnetic field strengths.

Variation of ferrite position. The ferrite with a diameter of 4 mm, is placed at four different positions inside the resonator, $(x, y) = (215, 60)$, $(225, 80)$, $(375, 60)$, $(245, 190)$ mm, see Fig. 5.1 for the definition of the coordinate system. The analysis of the $\mathcal{T}$ breaking strengths induced by the ferrite located at the four positions reveals that λ is independent of the position of the ferrite. This demonstrates the irregular structure of the electromagnetic field patterns inside the cavity, whose underlying classical dynamics is chaotic. In the remainder of the present work, the ferrite was always placed at the first position.

Variation of ferrite geometry. Keeping the field fixed at $B = 190$ mT, the diameter d of the ferrite is gradually increased from 4 mm to $d = 6,\ 8,\ 10$ mm.

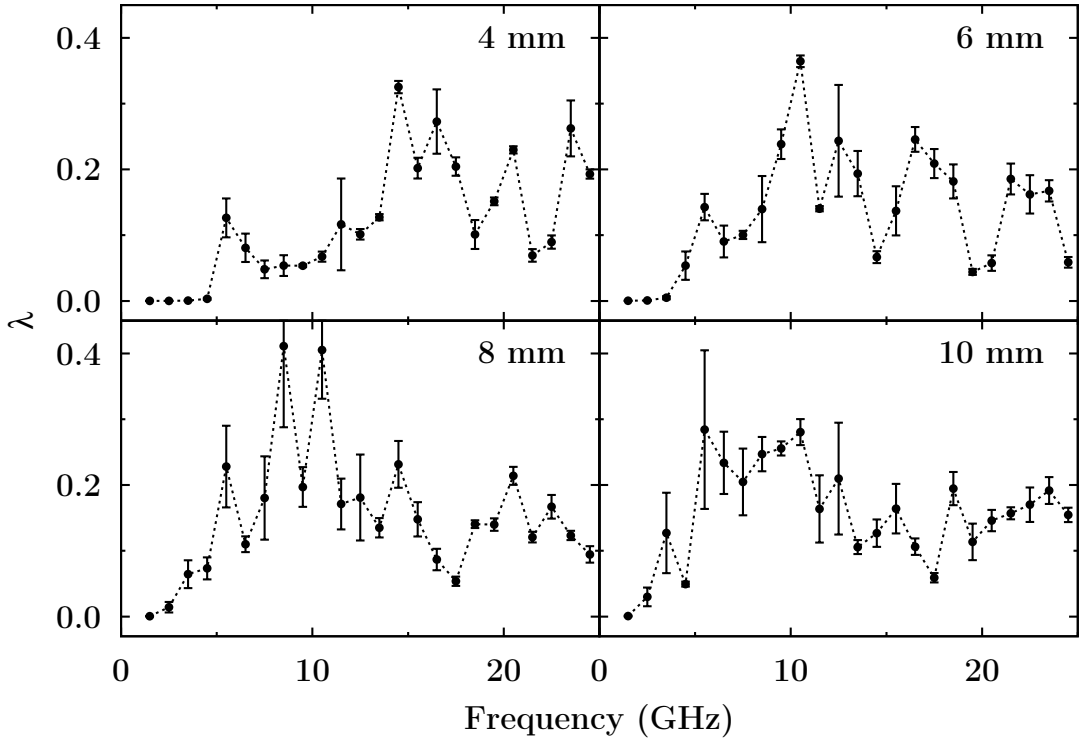

Fig. 6.3: Dependence of $\mathcal{T}$ breaking strength λ on ferrite diameter. The four panels display λ as a function of the excitation frequency window for ferrites with diameters $d = 4,\ 6,\ 8,\ 10$ mm and $B = 190$ mT. For each geometry three realizations were measured resulting in means (points) and variations (error bars) of λ. The dashed lines connecting the data points serve to guide the eye.

The result is shown in Fig. 6.3. While at 4 mm two peaks around 15 and 23 GHz are observed, at 6 mm a third is prominent at about 10 GHz with $\lambda \approx 0.35$. At $d = 8$ mm there are two peaks close to 9 and 11 GHz with $\lambda \approx 0.4$ while the $\mathcal{T}$ breaking effects at higher frequencies are diminished. Finally, at 10 mm the structures are broad and between 5 and 11 GHz a plateau at $\lambda \approx 0.25$ is formed. Thus, while the details of the size of the $\mathcal{T}$ breaking induced by the ferrite is very sensitive to its geometry, the maximally attainable λ is in all cases between 0.3 and 0.4. Ferrites of larger diameter feature broader structures, as the magnetization becomes inhomogeneous due to the limited size of the outer permanent magnets. These are 20 mm in diameter.

Variation of ferrite material. The only other ferrites available for the experiments were small rectangular sheets ($25.4 \times 50.8 \times 0.5$ mm^3) of "RG11", also courtesy of AFT GmbH. Its parameters are $4\pi M_\mathrm{s} = 1850$ Oe, $\varepsilon = 14.9$ and $\Delta H_{-3\ \mathrm{dB}} = 25$ Oe, see Sec. 3.4 for the corresponding parameters of CV19. Two of these sheets were brought into the resonator at $(x, y) = (215, 60)$ mm, one glued to the bottom plate and the other one glued to the top plate of the cavity, and exposed to a magnetic field $B = 210$ mT. The results were disappointing; over the measured frequency range 4–20 GHz, the degree of $\mathcal{T}$ breaking assumes an approximately constant value of $\lambda \approx 0.05$, which is supposedly due to the unfavorable shape of the ferrite pieces.

In conclusion, the $\mathcal{T}$ breaking induced by the ferrite sensitively depends on the geometry of the ferrite. Concerning the influence of the ferrite material no final judgment is possible as the shape of the RG11 differs too much from that of the other samples used. The position of the ferrite is irrelevant, at least for the chaotic cavity used in the present experiments. This result is to be expected in the light of Berry's random plane wave model for chaotic billiards [151] and in the regime of partially overlapping resonances. The surprise lies in the independence of λ on the strength of the external magnetic field B. While the $\mathcal{T}$ breaking at the frequency of the ferromagnetic resonance depends on B, at higher frequencies it does not. This rules out the possibility of second and third harmonics of the ferromagnetic resonance at 15 and 23 GHz. Together with the sensitivity to changes in the geometry of the ferrite it can be surmised that these peaks are either enhanced effects on the tail of the ferromagnetic resonance due to standing rf magnetic modes inside the ferrite, or that the mechanism of $\mathcal{T}$ breaking at these frequencies is altogether different.

6.3 Application of model to fluctuations

The preceding discussions established that neither the VWZ description nor the FSS model can truly be applied to the data of the present work. They can, however, serve as good approximations for frequency regions with exceptionally weak or strong time-reversal symmetry breaking. Figure 6.4 gives a comparison of the VWZ and FSS analysis results from Tab. 5.2 to the values of λ from Fig. 6.2. It roughly shows that while for $\lambda \lesssim 0.1$ the VWZ model is favored, an acceptance of the FSS model requires $\lambda \gtrsim 0.2$. These restrictions should be weakened when less realizations are included (the current analysis is based on 6 realizations) and more stringent for larger ensembles. This demonstrates that models based on a pure GOE or pure GUE assumption cannot describe the experiment in all its aspects.

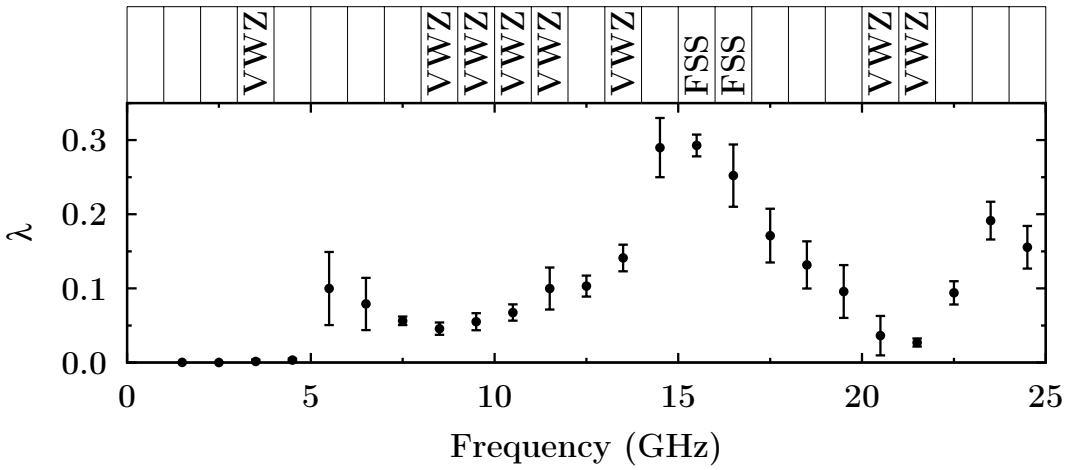

Fig. 6.4: Comparison of VWZ and FSS analysis results to the $\mathcal{T}$ breaking strengths. The graph shows λ for data obtained with $B = 190$ mT. It is identical to the one shown in the middle panel of Fig. 6.2. The cells above read "VWZ" or "FSS" if the GOF test unambiguously accepted the corresponding model in the associated frequency range. This information is taken from Tab. 5.2.

An application of the extended model for partial TRSB is straightforward. A Fourier transform of Eq. (6.4) brings the autocorrelation function into the time domain and eliminates one of the three integrations. The resulting expression can

be evaluated using the same numerical integration methods as implemented for the VWZ and FSS models. The new model depends on one additional parameter, the $\mathcal{T}$ breaking strength λ. The fitting procedure and the subsequent GOF test are exactly the same as for the FSS model and described in detail in Sec. 5.8.2. Even though λ can independently be determined from the cross-correlation function, it is treated—paying tribute to FRD uncertainties—as a free parameter, too. The value obtained from the cross-correlation function serves as a starting value for the fit. Especially for frequencies below 8 GHz the acceptance ratio is thereby considerably increased. At higher frequencies the differences between the initial values of λ and the refined ones are only marginal. A graphical representation of the GOF test results for the $B = 190$ mT situation is shown in Fig. 6.5.

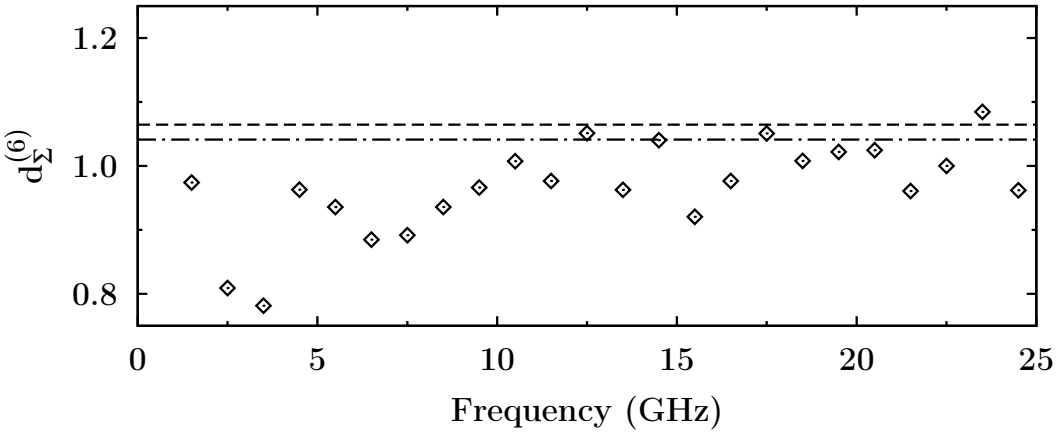

Fig. 6.5: GOF test result of the model for autocorrelation functions with partial TRSB for data with $B = 190$ mT. The final distance value $d_\Sigma^{(6)}$ as a function of the frequency interval is shown (diamonds). The acceptance threshold for a 10 % (20 %) chance of an erroneous fit rejection is at 1.064 (1.041) and included as a dashed (dash-dotted) line. Test results with $d_\Sigma^{(6)}$ values below this line are accepted.

Between 1 and 25 GHz the model is accepted in all but one frequency interval at 23–24 GHz. This rejection rate is based on a threshold of 0.9, allowing for 10 % erroneous test rejection. Thus in 24 test intervals two or three wrongly rejected fits do not contradict the model, but are even expected. Even for a stricter confidence limit of 0.8, thereby raising the erroneous rejection ratio to 20 %, only

3 tests fail while about 5 test rejections are acceptable. These convincing results are corroborated by the analysis of the data at 170 mT and 340 mT with the extended model, where in each case 5 tests are rejected at a confidence level of 0.9. Many of these rejected tests lie in frequency regions where λ changes rapidly with the excitation frequency. However, for the application of the model a constant value of λ over the considered frequency interval is assumed and, consequently, the GOF test rejects the model in cases where λ varies too much rightly.

A comparison in the frequency domain of the autocorrelation functions obtained for the three models with the experimental autocorrelations is shown in Fig. 6.6. Except for the curve derived from the model for partial TRSB (dash-dotted) with $\lambda = 0.246$ the figure is identical to Fig. 5.16. The agreement with the data is impressive. Even though in this frequency range (16–17 GHz) the FSS model (dashed) is accepted by the GOF test, the new model obviously does a much better job at describing the data.

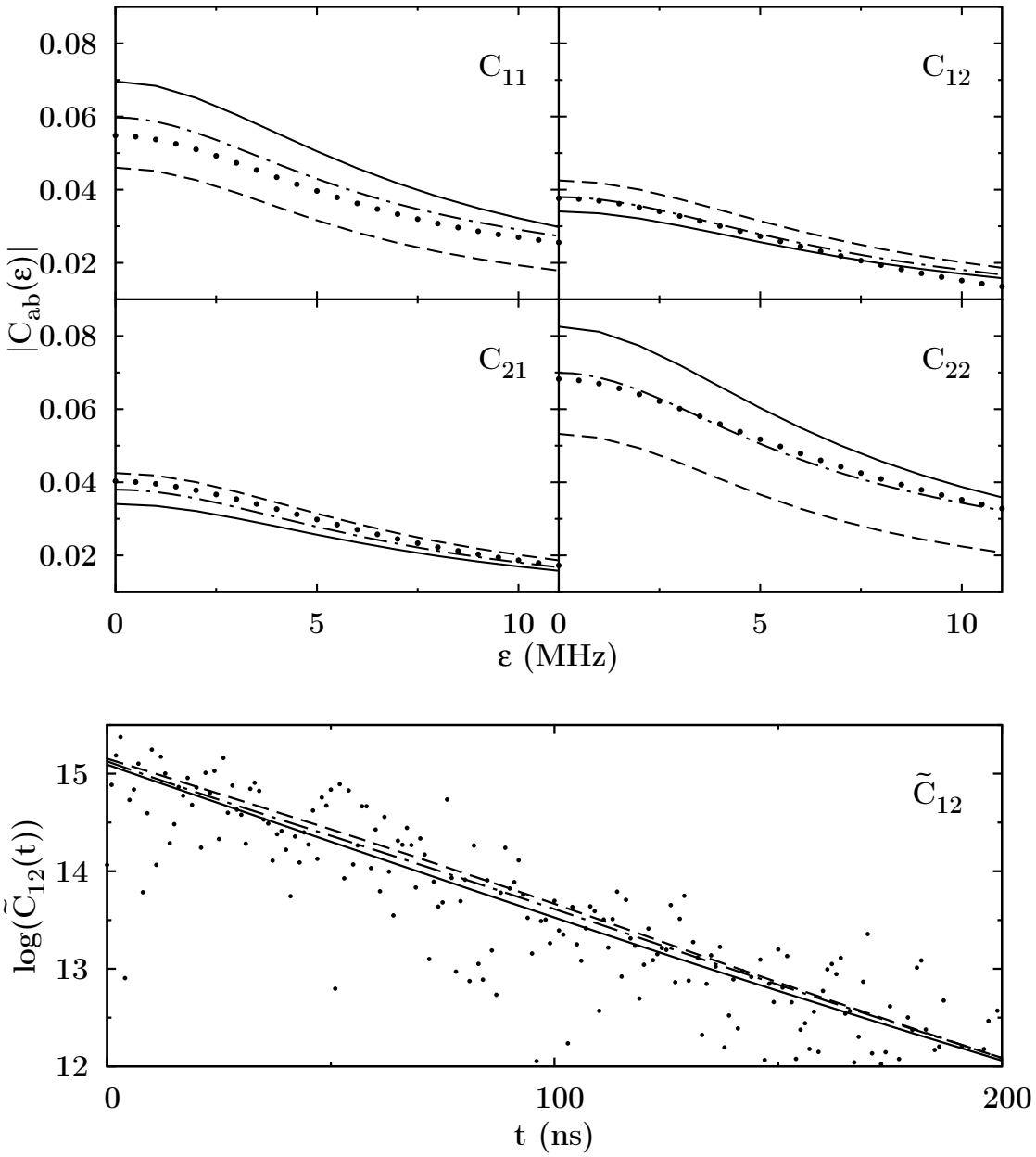

Fig. 6.6: Top: Comparison of autocorrelation functions in the frequency domain for a single realization in the range 16–17 GHz and for $B = 190$ mT. The four panels display the results for C_{11}, C_{12}, C_{21}, C_{22}. The discrepancy between data (dots) and VWZ (solid) or FSS (dashed) is large. The model for partial TRSB (dash-dotted) with $\lambda = 0.246$ follows the data closely. Bottom: C_{12} in the time domain (same key). The curve corresponding to the model for partial TRSB lies in-between those for the FSS and VWZ model.

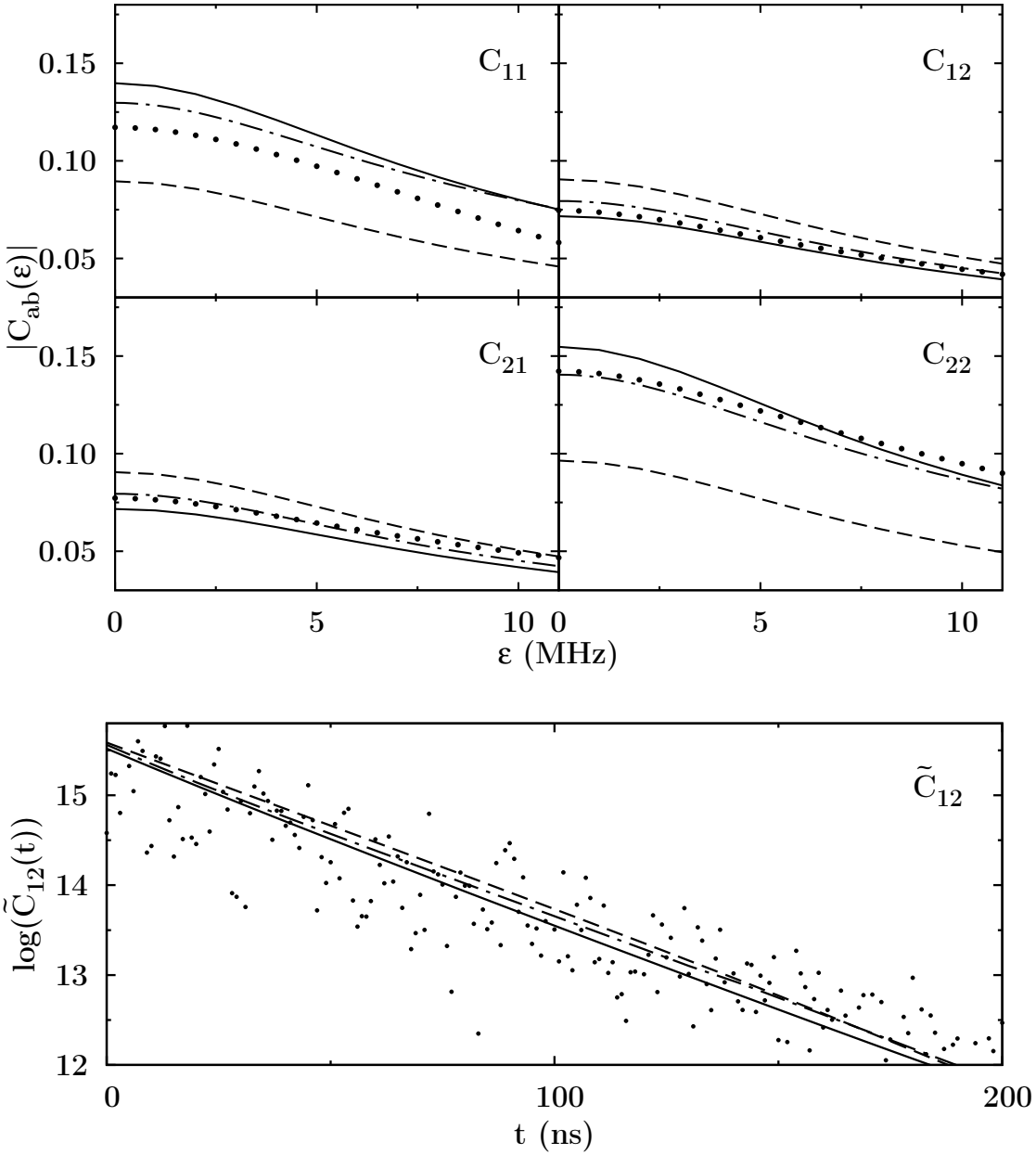

Fig. 6.7: Comparison of autocorrelation functions for a single realization in the frequency range 24–25 GHz and for $B = 190$ mT. The construction is as in Fig. 6.6 but with $\lambda = 0.224$.

A further exemplary result for the interval 24–25 GHz is depicted in Fig. 6.7. In this case neither VWZ nor FSS provided an adequate description of the data. The model for partial TRSB with $\lambda = 0.224$ is again in good agreement with the data.

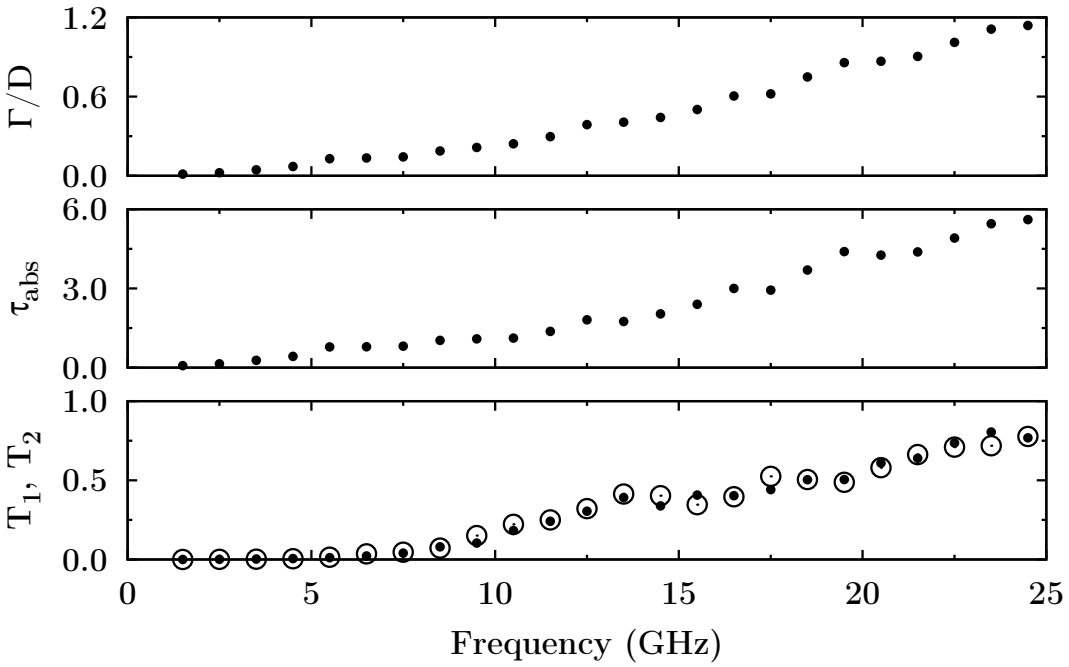

Fig. 6.8: Development of the transmission coefficients and Γ/D in the tilted stadium billiard with $B = 190$ mT as determined by the fit of the model for partial TRSB. Shown are the ensemble mean values of T_1 (T_2) as filled circles (open circles) in the bottom panel, $\tau_{\rm abs}$ in the middle panel and Γ/D, calculated according to Eq. (5.12), in the top panel as a function of the frequency interval. The variability of the values for different realizations is typically in the order of the symbol size. It is $T_1 \simeq T_2$ and $T_{1,2} \ll \tau_{\rm abs}$.

The parameters of the model are shown in Fig. 6.8. The transmission coefficients obtained from the extended model are very close to those determined by help of the VWZ and FSS models (see Fig. 5.11). However, only the values given in Fig. 6.8 are reliable as they are the parameters of a model that really describes the data. The analysis reveals that data in the whole range $0.01 < \Gamma/D < 1.2$ has been investigated. Thus the extended model holds for isolated as well as for overlapping resonances.

To conclude the discussion of the model for partial TRSB and its comparison to the experiment, the ensemble averaged values of λ obtained from the evaluation of the cross-correlation function (see Fig. 6.2) are compared to those obtained from the fit of the autocorrelation function to the data. The results are shown in

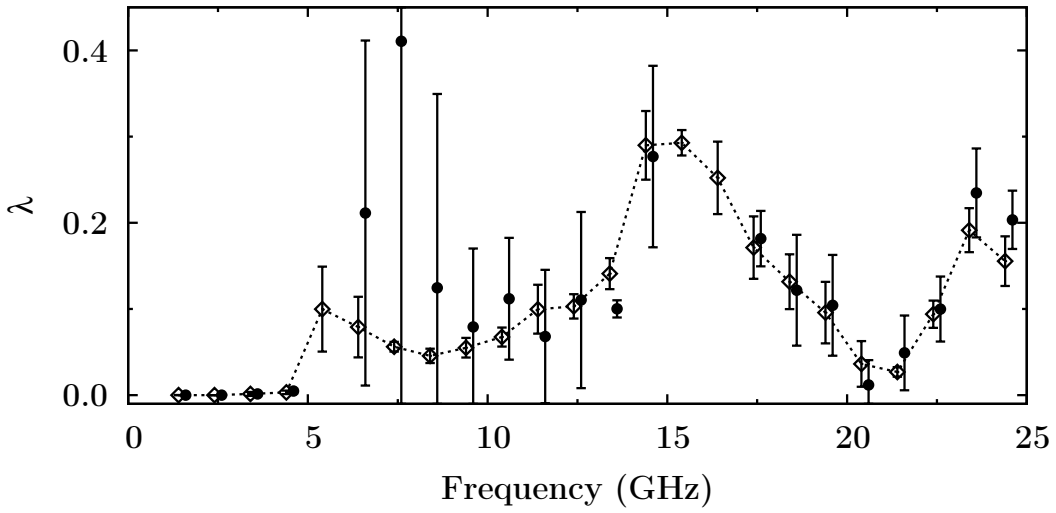

Fig. 6.9: Comparison of $\mathcal{T}$ breaking strengths λ obtained from the analysis of the cross-correlation function (diamonds, connected by dashed lines as guidance) to those values resulting from the fit to the autocorrelation function (dots) for $B = 190$ mT. The error bars indicate the ensemble variations. At 5–6 and 15–17 GHz the fit determined $\lambda > 1$.

Fig. 6.9. The values deduced from the autocorrelation function (dots) exhibit a large variability for different realizations (error bars in the figure). This spread is a consequence of the small differences in the shape of the autocorrelation function for different λ values in the time domain representation, see the bottom panel of Fig. 6.6. Keeping this additional difficulty in mind, the agreement of those two independent methods to determine λ is surprisingly good.

6.4 Elastic enhancement factor

In 1963, Satchler pointed out [152] that the Hauser-Feshbach expression in its *original* version $\sigma_{\alpha\beta} = T_\alpha T_\beta / \sum_c T_c$

> "is correct for the inelastic transitions [...], while the compound-elastic cross section $\sigma_{\alpha\alpha}$ is *underestimated* by a factor 2. [...] Even though the correction for compound elastic [...] is somewhat academic (since the direct interaction, or shape elastic, contribution will

generally dominate), [this] reveals the origin of the breakdown of the Hauser-Feshbach theory in a very clear way."

This statement turned out to be anything but academic—the factor of 2 was experimentally confirmed in 1978 by Kretschmer and Wangler [153]. Indeed Eq. (5.8) already includes this correction in $C_{\alpha\alpha}$. In the following years it was shown that this *elastic enhancement factor* (originally called *width fluctuation correction*) is not always necessarily exactly 2 but depends on the transmission coefficients and the symmetry properties of the scattering system. In Ref. [120] the limit of many, equally large transmission coefficients was investigated. An enhancement of 2 in the limit of strong absorption and, in contrast, a correction factor of 3 for isolated resonances was found. In Refs. [125, 154] these results have been confirmed numerically. Additionally, it was pointed out in Ref. [155] that in compound nucleus reactions with strong isospin mixing the elastic enhancement factor approaches unity[9]. In systems with complete TRSB the elastic enhancement factor has been predicted to also approach unity in the limit of strong absorption [156].

The explanation of this effect is illustrated in Fig. 6.10. A ray trajectory emitted from channel a is scattered inside the resonator (solid line) until it eventually returns to channel a, giving rise to a contribution to the reflection coefficient with a complex amplitude A'. In a $\mathcal{T}$ invariant system there always exists a complementary trajectory retracing the path in the opposite direction (dashed line) with final amplitude A'' which equals A' in magnitude and phase $A' = A'' = A$. Both add up coherently $|A' + A''|^2 = |A'|^2 + |A''|^2 + A'^* A'' + A' A''^* = 4|A|^2$. In systems with TRSB phase coherence for reciprocal paths is lost and the total scattering reduces to $2|A|^2$. Thus the reflected intensity is reduced by a factor of 2. The effect of elastic enhancement and its suppression due to TRSB is intimately connected to weak localization effects in the conductance properties of mesoscopic systems with magnetic fields, where the same mechanism can be applied to wave functions of scattered electrons. It is a field of active research since several decades [51, 91, 147]. In the explained sense elastic enhancement and weak localization may be considered as special cases of the Aharonov-Bohm

[9]However, in nature isospin mixing is never strong enough, so that still enhancement factors greater than 1.5 were predicted by the authors.

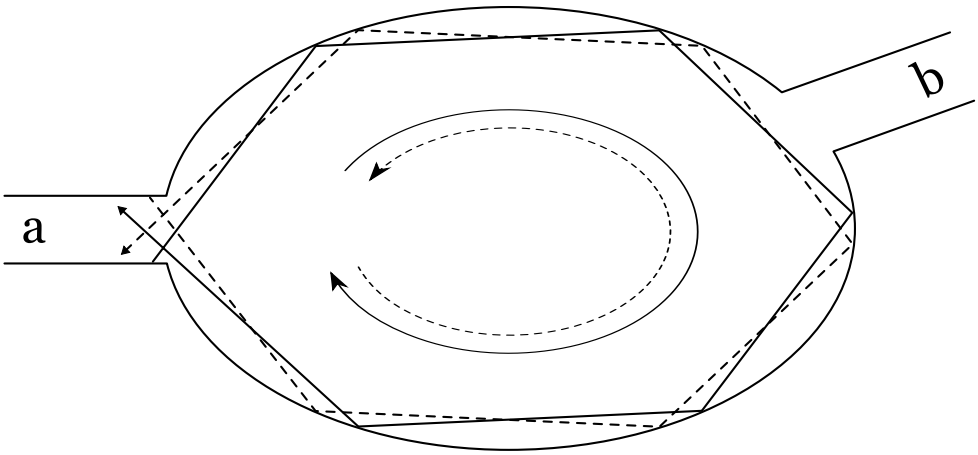

Fig. 6.10: Schematic explanation of elastic enhancement effect. The solid and dashed lines correspond to trajectories that start and end at channel a but circle the resonator boundary in opposing directions. The slight shift between both paths is for clarification only, in the model the dashed path identically retraces the solid one. In $\mathcal{T}$ invariant systems the trajectories add up coherently and increase the flux scattered back into channel a by a factor of 2 with respect to an incoherent sum.

effect. A very instructive realization of the situation shown in Fig. 6.10 has been demonstrated in acoustic experiments on rotational flows [71].

Applied to microwave billiards, the elastic enhancement factors $W_1,\ W_2$ for two antennas $1,\ 2$ can be defined, utilizing the Hauser-Feshbach formalism, as

$$\langle \sigma_{12} \rangle = C_{12}(0) \quad = \quad \frac{T_1\, T_2}{T_1 + T_2 + \tau_{\rm abs}}\,, \tag{6.7}$$

$$\langle \sigma_{11} \rangle = C_{11}(0) \quad = \quad W_1\, \frac{T_1\, T_1}{T_1 + T_2 + \tau_{\rm abs}}\,, \tag{6.8}$$

$$\langle \sigma_{22} \rangle = C_{22}(0) \quad = \quad W_2\, \frac{T_2\, T_2}{T_1 + T_2 + \tau_{\rm abs}}\,, \tag{6.9}$$

where C_{ab} denotes the autocorrelation function Eq. (5.6). Considering the geometric mean eliminates the transmission coefficients [102] and yields

$$W_{\rm enh} = \sqrt{W_1\, W_2} = \frac{\sqrt{C_{11}(0)\, C_{22}(0)}}{C_{12}(0)}\,. \tag{6.10}$$

In the limits of weak and strong absorption the enhancement W_{enh} is given as

$$W_{\mathrm{enh}} = \begin{cases} 1 + 2/\beta & \text{for } \Gamma/D \ll 1 \\ 2/\beta & \text{for } \Gamma/D \gg 1 \end{cases}, \tag{6.11}$$

for GOE ($\beta = 1$) and GUE ($\beta = 2$) systems [156]. The experiments in the regime of (weakly) overlapping resonances reported in the present work allow an estimation of W_{enh}. A systematic study of the elastic enhancement factor in microwave billiards in the regime of partial TRSB and its dependence on Γ/D has not been done before. Furthermore, unlike in nuclear physics, in the present work T_1 and T_2 usually dominate over the strength of each absorptive channel as shown in Fig. 6.8.

The elastic enhancement factor can be determined either directly by evaluating $C_{12}(0)$, $C_{11}(0)$ and $C_{22}(0)$, or from the widths of the distributions of the scattering matrix [102]. A determination from the widths is possible due to $C_{ab}(0) = \langle |S_{ab}(f) - \langle S_{ab}(f)\rangle|^2\rangle$, if $\langle S_{ab}(f)\rangle = 0$. Additionally, W_{enh} can be calculated from the extended model for partial TRSB in conjunction with the model parameters presented in Sec. 6.3.

First, in section Sec. 6.4.1 the distribution of the scattering matrix elements is studied and suitable widths for the extraction of the elastic enhancement factor are defined. Second, these factors, together with those obtained from the autocorrelation functions, are presented and discussed in Sec. 6.4.2.

6.4.1 Distribution of S-matrix elements

Figure 6.11 displays in logarithmic scale the probability distribution functions (PDFs) of the real and imaginary parts of S_{11} and S_{12} at 4–5 GHz (where $\Gamma/D \approx 0.1$), 14–15 GHz (where $\Gamma/D \approx 0.4$) and 24–25 GHz (where $\Gamma/D \approx 1.1$). All distributions are peaked and, except for $P(\mathrm{Re}\{S_{11}\})$, centered around 0. The reason for this special behavior of $\mathrm{Re}\{S_{11}\}$ lies within the structure of the scattering matrix. At isolated resonances (e.g. 4–5 GHz) it is mostly $S_{11} \approx 1$, that is close to the real axis at +1, whereas S_{12} mostly remains close to 0. This explains the narrow distributions at 4–5 GHz. At higher frequencies the S-matrix elements exhibit broader distributions due to the contributions of more and more

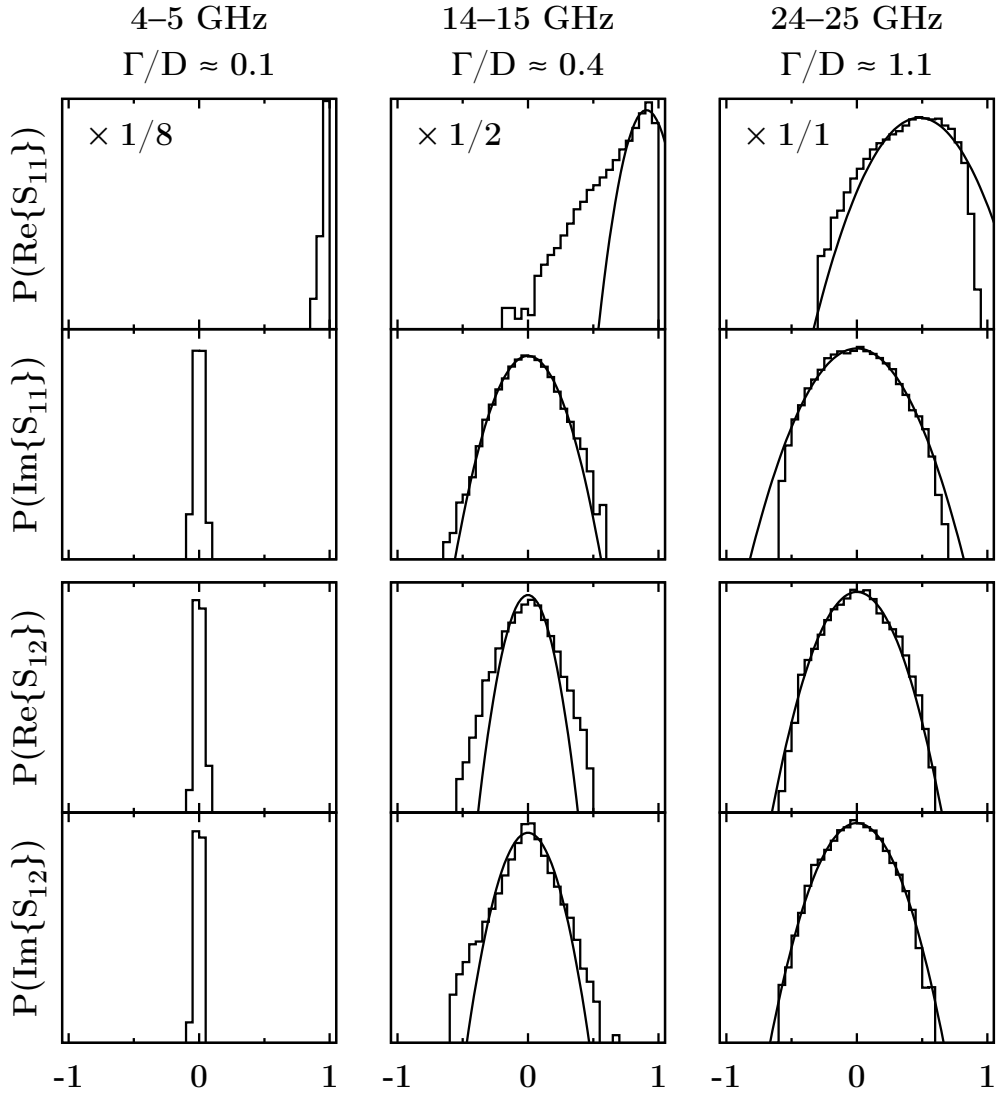

Fig. 6.11: Distribution of real and imaginary parts of scattering matrix elements in the ranges 4–5 GHz (left column), 14–15 GHz (center column) and 24–25 GHz (right column). The rows display (from top to bottom) the PDFs of $\mathrm{Re}\{S_{11}\}$, $\mathrm{Im}\{S_{11}\}$, $\mathrm{Re}\{S_{12}\}$ and $\mathrm{Im}\{S_{12}\}$. The ordinates are in logarithmic scale. The scaling of the histograms for each column with respect to the right column is given in the top panel. The histograms show the experimental data including 6 realizations, i.e. 60 000 data points per histogram, at $B = 190$ mT. Additionally, the center and right columns include fits of Gaussian distributions to the data.

resonances. The PDF of $\mathrm{Re}\{S_{11}\}$ slowly looses its special behavior. In the regime $\Gamma/D \gg 1$, all distributions should follow Gaussian distributions with mean 0 and equally distributed phases[10]. At 14–15 GHz especially the tails of the distributions do not agree with a Gaussian distribution. Even at 24–25 GHz this limit is not yet reached.

Still, the PDF of $\mathrm{Im}\{S_{11}\}$ assumes a shape with a well defined width at moderate values of $\Gamma/D \gtrsim 0.2$. Hence, the width of $\mathrm{Im}\{S_{11}\}$ is taken for the evaluation of the elastic enhancement factor. For consistency, only the widths of the distribution of the imaginary part of S_{12} has been used to determine the latter. It should be noted, that the widths of the PDFs of $\mathrm{Im}\{S_{12}\}$ and $\mathrm{Re}\{S_{12}\}$ typically agree within less than 1 %.

The nearly perfect agreement of the distributions of the scattering matrix elements $\tilde{S}_{ab}$ in the time domain with Gaussian distributions highlighted in Sec. 5.8.1 is in stark contrast to the non-Gaussian distribution of the S-matrix elements in the frequency domain, shown here. If the $\tilde{S}_{ab}$ were to truly follow a Gaussian distribution, the same would be expected for S_{ab}, as the two are connected by a Fourier transform. This means that S_{ab} can be represented as a linear combination of the $\tilde{S}_{ab}$. If the S_{ab} are non-Gaussian distributed (which is especially true for $\mathrm{Re}\{S_{11}\}$) so should be the $\tilde{S}_{ab}$. Yet the fact remains that with the applicable statistical methods the distribution of $\tilde{S}_{ab}$ is indistinguishable from a Gaussian one, see Sec. 5.8.1. The reason for this puzzling resemblance is yet to be found. A test for higher moments cannot provide new insight as the uncertainties grow faster than expected deviations from a Gaussian behavior [157].

6.4.2 Experimental results

The last section established that the distributions of the scattering matrix elements are peaked and have well defined widths. Especially the PDFs of the imaginary parts are centered around zero and their variances are defined as

$$\langle(\mathrm{Im}\{S_{ab}\} - \langle\mathrm{Im}\{S_{ab}\}\rangle)^2\rangle = \langle(\mathrm{Im}\{S_{ab}\} - 0)^2\rangle = \langle\mathrm{Im}\{S_{ab}\}^2\rangle\,. \tag{6.12}$$

[10] In the regime of overlapping resonances at a given frequency many resonances contribute to the sum of poles in Eq. (2.7). Thus, by virtue of the central limit theorem, the distribution of S-matrix elements follows a Gaussian distribution. The phases of S are equally distributed as due to the coupling W the wave functions of the resonator decay and are complex with essentially random phases.

Following the arguments of the introduction to Sec. 6.4, there are three ways to estimate the elastic enhancement factor W_{enh},

$$W_{\mathrm{enh}} = \frac{\sqrt{\langle \mathrm{Im}\{S_{11}\}^2\rangle \, \langle \mathrm{Im}\{S_{22}\}^2\rangle}}{\langle \mathrm{Im}\{S_{12}\}^2\rangle}\,, \tag{6.13}$$

$$W_{\mathrm{enh}} = \frac{\sqrt{C_{11}(0)\, C_{22}(0)}}{C_{12}(0)}\,, \tag{6.14}$$

$$W_{\mathrm{enh}} = \frac{\sqrt{C_{11}(0,\zeta)\, C_{22}(0,\zeta)}}{C_{12}(0,\zeta)}\,. \tag{6.15}$$

While the first two methods directly exploit the experimental data, the third one relies on the model for partial TRSB and the determined parameter sets ζ.

Figure 6.12 shows the analysis results from the measurements with an exter-

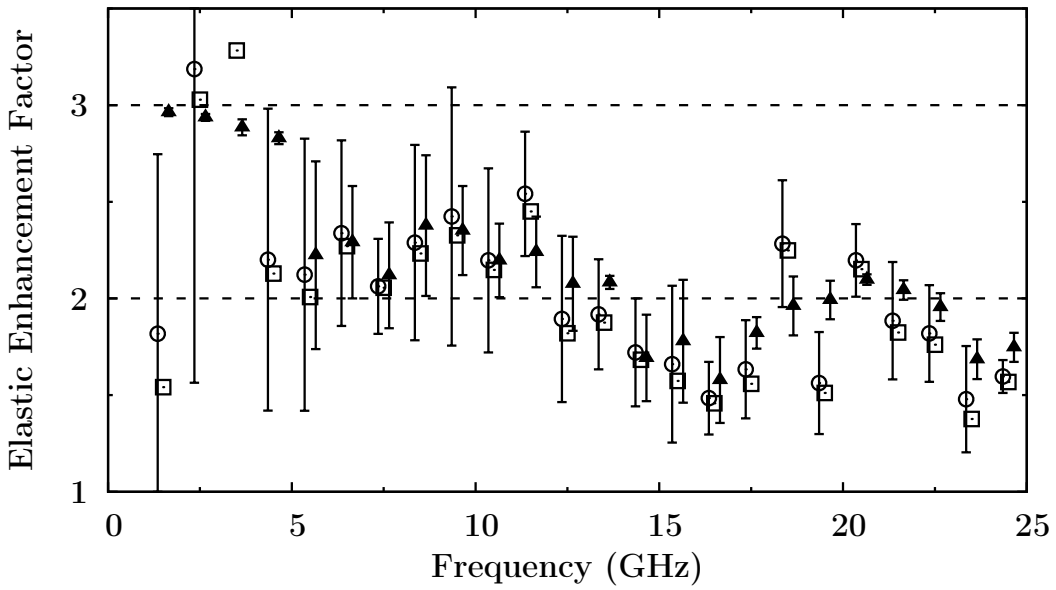

Fig. 6.12: Elastic enhancement factor W_{enh} for the microwave billiard with $B =$ 190 mT. The estimates of W_{enh} are based on the widths of the scattering matrix element distributions (open squares), the experimentally determined autocorrelation coefficients (open circles with error bars) and the autocorrelation coefficients calculated with the model for partial TRSB (triangles with error bars). The error bars represent the standard deviation within the 6 realizations from the ensemble mean values. The dashed vertical lines are at $W_{\mathrm{enh}} = 3$ and 2 and represent the GOE limit of isolated and overlapping resonances, respectively.

nal magnetic field of 190 mT. The data set comprises 6 realizations resulting in 60 000 data points per frequency interval and S-matrix element. From these data the widths of the PDFs of $\mathrm{Im}\{S_{ab}\}$ are determined (see Fig. 6.11). With the help of Eq. (6.13) the elastic enhancement factor is calculated (open squares in Fig. 6.12). From the experimental autocorrelation functions the elastic enhancement factor is calculated for each realization separately. Using the 6 realizations the mean of W_{enh} and its ensemble standard deviation are determined from the experimental autocorrelation functions (open circles with error bars) and from the autocorrelation functions as predicted by the model for partial TRSB (triangles with error bars). Above 5 GHz all three methods agree very well. Below, only few resonances contribute to the data. Thus due to FRD errors the elastic enhancement factors fluctuate strongly. In general, the enhancement factors determined from the autocorrelation function model should yield the most reliable results, as its data basis consists—by virtue of the fit—not just of the first autocorrelation coefficient, but of all coefficients. Indeed, at frequencies below 5 GHz the triangles in Fig. 6.12 are close to 3, as expected for isolated resonances. Around 15 and 23 GHz the values of W_{enh} are considerably below 2. This is a clear indication of TRSB and is in agreement with earlier results that showed relatively strong $\mathcal{T}$ breaking in the same frequency regions, see Fig. 6.2. Furthermore, at 5–6 GHz a sudden decrease of W_{enh} is be observed which is directly connected to the $\mathcal{T}$ breaking effects of the ferromagnetic resonance.

For comparison, the data of the billiard without ferrite have been analyzed in the same way. The outcome of the evaluation of W_{enh} with Eqs. (6.13)–(6.15) is shown in Fig. 6.13. The overall tendency is similar; at low frequencies the resonances are isolated and the elastic enhancement factors are close to 3. With the frequency the transmission coefficients increase. Consequently, W_{enh} approaches 2. However, in no frequency region the elastic enhancement factor is unequivocally less than 2. This is consistent with $\mathcal{T}$ invariant dynamics.

In summary, the work presented here described three different approaches to determine elastic enhancement factors: (i) the widths of the S-matrix element distributions, and (ii) autocorrelation functions at $\varepsilon = 0$ either directly from the experiment or (iii) indirectly from appropriate models fitted to the data. In general, methods (i) and (ii) give very similar results but suffer, especially for low frequencies, from FRD errors. Method (iii) is numerically demanding and time

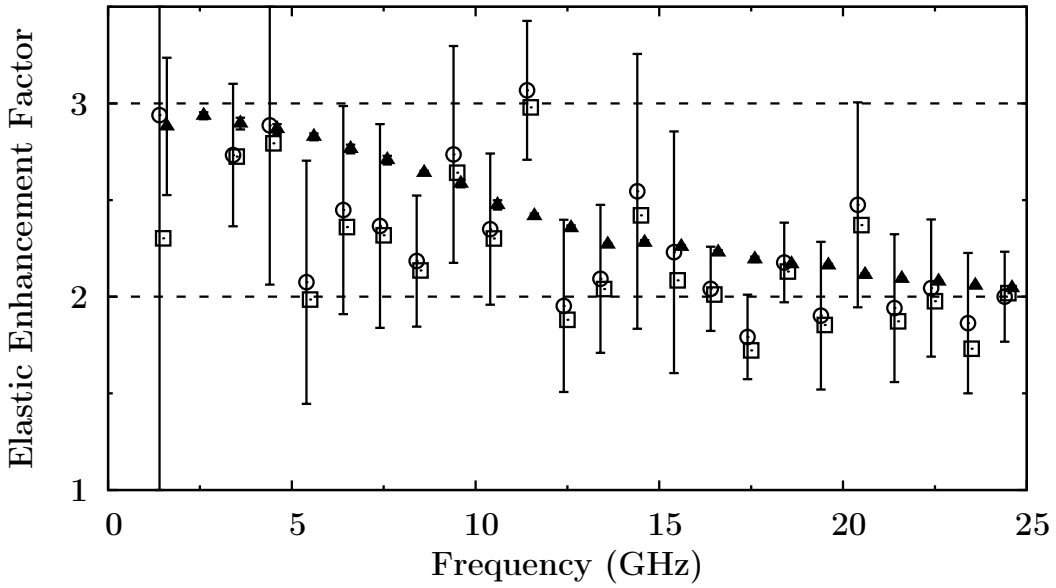

Fig. 6.13: Elastic enhancement factor W_{enh} for the microwave billiard without ferrite. Data basis is an ensemble measurement consisting of 6 realization. The layout and key of the figure is as in Fig. 6.12.

consuming but permits a most precise determination of the elastic enhancement factor as it probes the complete autocorrelation function. In $\mathcal{T}$ invariant billiards, W_{enh} is found to be between 3 for $\Gamma/D \ll 1$ and 2 for $\Gamma/D \approx 1$ despite the fact that not all transmission coefficients are equal. A magnetized ferrite breaks $\mathcal{T}$ invariance, especially efficiently around 15 and 23 GHz, which is expressed in reduced elastic enhancement factors, values as low as 1.5 have been observed.

To the best knowledge of the author, this is the first time that the effect of elastic enhancement has been studied experimentally in systems with (partial) TRSB and is complementary to the insight gained on weak localization in electron transport properties in the presence of magnetic fields. Especially method (ii) may prove to be a useful tool to study time-reversal symmetry in the common scenario $\Gamma/D \gg 1$ (where only little information is to be gained by "standard" approaches) as it only relies on averages of cross sections. Besides the obvious application of these results to nuclear physics, a transfer to atomic spectroscopy, to mesoscopic electronic devices or to complex optical and acoustical systems seems feasible and desirable.

7 Final considerations

The present work gives results of the investigation of properties of scattering systems with partially broken time-reversal symmetry. Even though the related questions were originally posed in nuclear physics, microwave billiards provide ideal devices for the study of scattering systems in general and for the modeling of generic features of compound nucleus reactions. In this analogy the scattering channels are replaced by metallic leads that are connected to the microwave resonator. The quasi bound states of the compound nucleus are in turn modeled by the resonator modes. However, the breaking of time-reversal invariance poses a fundamental difference in this analogy. To observe $\mathcal{T}$ breaking in a compound nucleus is only possible if the underlying nuclear force has time-reversal non-invariant components. To the contrary, in a microwave billiard $\mathcal{T}$ breaking is induced by a magnetized ferrite. Especially, the time-reversal symmetry breaking strength can be tuned to much larger magnitudes than the one in a nucleus (if it should exist there at all).

The high precision of the measurements allowed for a detailed study of pairs of nearly degenerate resonances. The description of these data by the scattering matrix formalism adopted from nuclear physics allowed a precise determination of the effective Hamiltonian. What is more, the $\mathcal{T}$ breaking matrix element obtained from the Hamiltonian could be traced back to the magnetic structure of the ferrite. Equipped with this confidence in both, experiment and theory, the problem of overlapping resonances was addressed. The presented experiments confirmed that weak $\mathcal{T}$ breaking is enhanced in valleys of the cross section, an effect that was already exploited in the search for a violation of $\mathcal{T}$ invariance in compound nucleus reactions. Additionally, fluctuations of the scattering matrix were investigated. These are encountered for example in mesoscopic devices, in acoustics, in Rydberg atoms, in nuclear physics and in quantum billiards. Correlation functions of the fluctuations were compared to RMT model predictions using a goodness of fit (GOF) test. This test relies on an analysis in the time domain and a Gaussian distribution of the Fourier coefficients. Surprisingly, even though the distributions of the measured scattering matrix elements are not Gaussian ones, those of their Fourier coefficients are indistinguishable from the latter. The analyses showed that the models by Verbaarschot, Weidenmüller and Zirnbauer

(for the GOE) and by Fyodorov, Savin, Sommers and Verbaarschot (for the GUE) only partially describe the data. This motivated the development of an extended model incorporating an Hamiltonian for the crossover between GOE and GUE. The extended model describes correlation functions in the regime of partially broken time-reversal symmetry. A good agreement of the data with this model was found. Furthermore, it provided direct access to the $\mathcal{T}$ breaking strengths, values up to a third of a mean level spacing were observed. Finally, elastic enhancement factors were estimated using three different approaches and yielding consistent results. Observed values of less than two are a clear indication of time-reversal symmetry breaking. This is the first time that effects of $\mathcal{T}$ breaking on spectra of overlapping resonances were actually experimentally observed and quantified.

Still, some unsolved problems remain. Especially analyses of data in the frequency domain suffer from the inevitable finiteness of the data samples. These finite range of data (FRD) errors could partially be avoided by a switchover to the time domain. It is not yet clear how the GOF test is affected by those FRD contributions, and how to account for them in the measured correlation functions and the derived quantities such as transmission coefficients. Another puzzle is the distribution of the Fourier coefficients of the scattering matrix elements. The empirically found agreement with the Gaussian distribution is fortunate for the analysis but not understood and further theoretical insight is required.

The consequences of the present work are manifold. The results on singlets and doublets are, if nothing else, beautiful manifestations of quantum mechanics at work. They allow an insight into the scattering formalism and the principle of $\mathcal{T}$ invariance while keeping the mathematical effort at a feasible level. In the regime of weakly overlapping resonances the earlier development of a test for VWZ provided a completely new tool to probe the chaotic dynamics of an open scattering system. Even small deviations from a GOE behavior could be detected. The present work increased the analyzing power of the statistical test and made its sensitivity adjustable by combining the available GOF test with the known technique of ensemble measurements. Now three new tools—cross-correlations, autocorrelations and elastic enhancement factors—are available to distinguish between GOE, GUE and systems with partially broken time-reversal symmetry and to classify them quantitatively, just by looking at the scattering matrix and its seemingly erratic fluctuations.

A Connection between ferrite and effective Hamiltonian

For isolated doublet modes the TRSB matrix element H_{12}^a can be understood in terms of properties of the ferrite and the mode structure at the position of the ferrite. In this section the calculations leading to Eq. (4.11) are elucidated.

The derivation is based on the following model: Inside a resonator two modes $|1\rangle$ and $|2\rangle$ are excited which couple to three channels; the two antennas connected to the VNA and a channel connecting the magnetic rf component of the resonator modes to the ferromagnetic resonance of the ferrite. An appropriate ansatz for this model is Eq. (4.8),

$$H_{\mu\nu}^{\text{eff}} = W_{\mu\nu} + \sum_{i=a,b,f} \int_{-\infty}^{\infty} \mathrm{d}\omega' \frac{W_{\mu i}(\omega') W_{\nu i}^*(\omega')}{\bar{\omega}^+ - \omega'} \,, \tag{A.1}$$

with $\bar{\omega}^+ = \bar{\omega} + i\,\epsilon,\ \epsilon > 0$ and $W_{\mu\nu}$, $\{\mu, \nu\} \in \{1, 2\}$ describing the internal dynamics of the system; the coupling to the three channels (a, b to antennas, f to ferrite) is modeled by $W_{\mu i}$.

As stated in Sec. 3.3 it is known that magnetized ferrites couple differently to circular polarized rf magnetic fields. Therefore the coupling to the ferrite is expressed in terms of a circular basis by a unitary transformation

$$|\tilde{x}\rangle = U|x\rangle \quad \text{with} \quad U = \frac{1}{\sqrt{2}} \begin{pmatrix} 1 & i \\ 1 & -i \end{pmatrix} \,, \tag{A.2}$$

where $|x\rangle$ is an element of the real basis. Here and in the sequel a tilde denotes quantities in the circular basis. It thus follows for the two circular modes $|\pm\rangle$

$$\begin{pmatrix} |+\rangle \\ |-\rangle \end{pmatrix} = U \begin{pmatrix} |1\rangle \\ |2\rangle \end{pmatrix} = \frac{1}{\sqrt{2}} \begin{pmatrix} |1\rangle + i|2\rangle \\ |1\rangle - i|2\rangle \end{pmatrix} \,. \tag{A.3}$$

The couplings W to the ferrite (subscript f) transform as

$$\tilde{W} = U\,W \quad \Rightarrow \quad \tilde{W}_{\mu f} = \sum_{i=1,2} U_{\mu i}\, W_{if} \,, \tag{A.4}$$

$$W = U^\dagger\, \tilde{W} \quad \Rightarrow \quad W_{\mu f} = \sum_{i=1,2} U_{i\mu}^*\, \tilde{W}_{if} \,. \tag{A.5}$$

As the ferrite couples only to, say $|+\rangle$, it is $\tilde{W}_{2f} = 0$ and $W_{\mu f}$ reduces to

$$W_{\mu f} = U_{1\mu}^{*}\, \tilde{W}_{1f}\,. \tag{A.6}$$

The remaining coupling $\tilde{W}_{1f}$ is taken to be proportional to the magnetic susceptibility $\chi_{+}(\omega')$, see Eq. (3.9), of the ferrite described by the ferromagnetic resonance

$$\tilde{W}_{1f}(\omega') = A\frac{\omega_M}{\omega_0(B) - \omega' - i/T} \propto \chi_{+}(\omega')\,, \tag{A.7}$$

where A is an as of yet undetermined proportionality factor. Inserting Eq. (A.6) into Eq. (A.1) gives

$$\begin{aligned} H^{\text{eff}}_{\mu\nu} = W_{\mu\nu} \quad &+ \quad \sum_{i=a,b}\int_{-\infty}^{\infty} \mathrm{d}\omega' \frac{W_{\mu i}(\omega')W^{*}_{\nu i}(\omega')}{\bar{\omega}^{+} - \omega'} \\ &+ \quad \underbrace{\int_{-\infty}^{\infty} \mathrm{d}\omega' \frac{(U^{*}_{1\mu}\tilde{W}_{1f}(\omega'))\,(U_{1\nu}\tilde{W}^{*}_{1f}(\omega'))}{\bar{\omega}^{+} - \omega'}}_{H^f}\,. \end{aligned} \tag{A.8}$$

Only the last term, H^f, breaks $\mathcal{T}$ invariance and gives rise to H^a_{12}. Hence just the evaluation of H^f will be further pursued. To this end the product

$$U^{*}_{1\mu}\, U_{1\nu} = \frac{1}{2}\begin{pmatrix} 1 & i \\ -i & 1 \end{pmatrix} \tag{A.9}$$

and the integral

$$\int_{-\infty}^{\infty} \mathrm{d}\omega' \frac{1}{\bar{\omega}^{+} - \omega'}\left(\frac{|A|\omega_M}{\omega_0(B) - \omega' - i/T}\right)^2 = \pi\, T\, |A|^2\, \frac{\omega_M^2}{\omega_0(B) - \bar{\omega} - i/T} \tag{A.10}$$

are required. Collecting these results yields

$$H^f = \frac{\pi}{2}\, T\, |A|^2 \frac{\omega_M^2}{\omega_0(B) - \bar{\omega} - i/T}\begin{pmatrix} 1 & i \\ -i & 1 \end{pmatrix} \tag{A.11}$$

as the contribution of the ferrite to H^{eff}. Therefore, the $\mathcal{T}$ breaking antisymmetric part, defined in Eq. (4.5), is

$$H^a(B) = \frac{\pi}{2}\, \zeta\, B\, T\, \frac{\omega_M^2}{\omega_0(B) - \bar{\omega} - i/T}\begin{pmatrix} 0 & 1 \\ -1 & 0 \end{pmatrix}\,, \tag{A.12}$$

where the proportionality factor $|A|^2$ has been replaced by $\zeta\, B$. The coupling strength to the local mode structure is given by ζ and the $\mathcal{T}$ breaking strength scales linearly in B. This reproduces the result Eq. (4.11).

B Discrete Fourier transform

The complex Fourier transform $\tilde{S}(t)$ of a continuously known scattering matrix element $S(f)$ is defined as

$$\tilde{S}(t) = \int_{-\infty}^{\infty} S(f)\, e^{-2\pi i\, t\, f}\, \mathrm{d}f\,. \tag{B.1}$$

Experimentally, the VNA can take data only in a finite frequency range at m equidistant discrete frequencies f_ν, $\nu = 0, \ldots, m-1$, separated by $\Delta f = f_{\nu+1} - f_\nu$. For odd m, the discrete Fourier transform of the measured S_ν is

$$\tilde{S}_k = \Delta f \sum_{\nu=0}^{m-1} S_\nu\, e^{-2\pi i\, t_k\, f_v} \tag{B.2}$$

$$= \Delta f \sum_{\nu=0}^{m-1} S_\nu\, e^{-2\pi i\, \nu\, k/m}\,, \tag{B.3}$$

where $f_\nu = \nu\, \Delta f$ and

$$t_k = \frac{k}{m\, \Delta f}, \quad k = -\frac{m-1}{2}, \ldots, \frac{m-1}{2} \tag{B.4}$$

as the corresponding times have been exploited.

A numerical implementation of the discrete Fourier transform needs, for data including m data points, to evaluate $\mathcal{O}(m^2)$ mathematical operations[11]. Hence the discrete Fourier transform is computationally expensive; the required time scales quadratically with the number of data points. Using fast Fourier transform algorithms the required number of operations could be reduced to $\mathcal{O}(m \log m)$, a substantial gain in speed for large spectra. However, the fast Fourier transform only works on power-of-two sized data samples. That is, either valuable data need to be discarded or the data block has to be zero padded. The first solution would result in a loss of precision while the second one shams a better time resolution than available. Both outcomes are not desired for the precise tests the time domain data will be subjected to. Hence, the discrete Fourier transform Eq. (B.3) is chosen which on intervals of 1 GHz can still be calculated in an acceptable time.

[11] In computer science the notation $\mathcal{O}(m^2)$ means that the number of mathematical operations an algorithm requires is proportional to m^2.

C Derivation of distance functions

In order to judge the compatibility of a model description to experimental findings a goodness of fit (GOF) test can be used. For the analysis of the decay of correlations in the time domain standard methods based on Gaussian statistics cannot be applied due to the skewed nature of the distribution of the data points, see Sec. 5.8.1. This appendix addresses this issue and develops a distance function that quantifies the deviations between the data and the model predictions. The derivation presented in Sec. C.1 was started by Friedrich in Ref. [49] and Harney [158], shortly thereafter finalized and the results were used in Ref. [102]. For the present work an extension of the results (which are valid only for data of single realizations) to ensemble measurements was necessary and is addressed in Sec. C.2. The probability distribution of the distance function needed for the definition of acceptance thresholds of the GOF test is derived in Sec. C.3.

C.1 Single realization

The χ^2-distribution with two degrees of freedom, Eq. (5.16),

$$q(x_k|\bar{x}_k) = 1/\bar{x}_k \, \exp\left(-x_k/\bar{x}_k\right) \tag{C.1}$$

gives the probability to measure the event x_k at the time t_k while the actual expected value should be $\bar{x}_k$. The definitions

$$y_k = \ln x_k, \quad \eta_k = \ln \bar{x}_k \tag{C.2}$$

facilitate, obeying conservation of probabilities $q(x_k|\bar{x}_k)\,\mathrm{d}x_k = P(y_k|\eta_k)\,\mathrm{d}y_k$, a transformation of Eq. (C.1) into a logarithmic scale

$$P(y_k|\eta_k) = \exp\left(y_k - \eta_k - e^{y_k-\eta_k}\right) , \tag{C.3}$$

which gives Eq. (5.17). Starting from this intermediate result a distance function d has to be found that can replace the χ^2-test. A general approach [158, 159] is

$$\begin{aligned} d(y_k|\eta_k) &\propto \text{const} - \ln P(y_k|\eta_k) \\ &= \text{const} - (y_k - \eta_k) + e^{y_k-\eta_k} . \end{aligned} \tag{C.4}$$

The constant needs to be chosen to guarantee $d > 0$ for all $\{y_k,\ \eta_k\}$ and $d = 0$ for $y_k = \eta_k$. A simple calculation determines the constant to be -1, i.e.

$$d(y_k|\eta_k) = \frac{1}{N}\left(e^{y_k-\eta_k} - (y_k - \eta_k) - 1\right) . \tag{C.5}$$

The proportionality factor N^{-1} is determined by a normalization of d to an expectation value of 1, as for the reduced χ^2 value. The condition

$$\int_{-\infty}^{\infty} P(y|\eta_k)\, d(y|\eta_k)\, \mathrm{d}y = 1 \tag{C.6}$$

fixes N to equal $\gamma \approx 0.5772$, Euler's constant. This completes the derivation, the result

$$d(y_k|\eta_k) = \frac{1}{\gamma}\left(e^{y_k-\eta_k} - (y_k - \eta_k) - 1\right) \tag{C.7}$$

equals Eq. (5.19) and gives a suitable distance function for a statistically justified GOF test where $\eta_k = \eta_k(\zeta)$ depends on model parameters united in ζ.

C.2 Multiple realizations

In a microwave billiard n independent realizations are measured. These are assumed to yield uncorrelated spectra. For each spectrum the decay of the autocorrelation function in the time domain is calculated, so that for each time t_k there are n statistically independent values of x_k. The distribution of x_k is given by Eq. (C.1). Purpose of an ensemble measurement is the suppression of system specific, non-universal behavior combined with a statistically more significant data base. Hence, for each time t_k an ensemble average of the n experimental x_k values

$$x_k^{(n)} = \overline{x_k}^{(n)} \tag{C.8}$$

is performed. In the following the subscript k will be dropped until further notice, as it is understood that all values are to be taken at same times.

The distribution of $x^{(n)}$ is not yet known and has to be determined. Therefore, in a first step the joint distribution of $z^{(2)} = x_1 + x_2$ with equal probability

distributions $p^{(1)}(x_i)$ with $x_i \geq 0$ is considered. The distribution of the sum $z^{(2)}$ of the two random variables is given by a convolution of its constituents

$$p^{(2)}(z^{(2)}) = \int_0^{z^{(2)}} p^{(1)}(\lambda)\, p^{(1)}(z^{(2)} - \lambda)\, \mathrm{d}\lambda \tag{C.9}$$

and an recursive application of this relation gives

$$p^{(n)}(z^{(n)}) = \int_0^{z^{(n)}} p^{(n-1)}(\lambda)\, p(z^{(n)} - \lambda)\, \mathrm{d}\lambda \tag{C.10}$$

for $z^{(n)} = \sum_{i=1}^{n} x_i$ with identical distributions $p(x_i)$. In the case at hand, $p(x_i)$ is replaced by Eq. (C.1). Starting with the joint probability of two events,

$$\begin{aligned}
\tilde{q}^{(2)}(z^{(2)}|\bar{x}) &= \int_0^{z^{(2)}} q(\lambda|\bar{x})\, q(z^{(2)} - \lambda|\bar{x})\, \mathrm{d}\lambda \\
&= \frac{1}{\bar{x}^2} \int_0^{z^{(2)}} \exp\left(-\frac{\lambda}{\bar{x}}\right) \exp\left(-\frac{z^{(2)}}{\bar{x}} + \frac{\lambda}{\bar{x}}\right) \mathrm{d}\lambda \\
&= \frac{1}{\bar{x}^2} \int_0^{z^{(2)}} \exp\left(-\frac{z^{(2)}}{\bar{x}}\right) \mathrm{d}\lambda \\
&= \frac{1}{\bar{x}^2} \frac{z^{(2)}}{1} \exp\left(-\frac{z^{(2)}}{\bar{x}}\right),
\end{aligned} \tag{C.11}$$

and repeating the process for a further term,

$$\begin{aligned}
\tilde{q}^{(3)}(z^{(3)}|\bar{x}) &= \int_0^{z^{(3)}} \tilde{q}^{(2)}(\lambda|\bar{x})\, q(z^{(3)} - \lambda|\bar{x})\, \mathrm{d}\lambda \\
&= \frac{1}{\bar{x}^3} \int_0^{z^{(3)}} \lambda \exp\left(-\frac{\lambda}{\bar{x}}\right) \exp\left(-\frac{z^{(3)}}{\bar{x}} + \frac{\lambda}{\bar{x}}\right) \mathrm{d}\lambda \\
&= \frac{1}{\bar{x}^3} \frac{\left(z^{(3)}\right)^2}{1 \cdot 2} \exp\left(-\frac{z^{(3)}}{\bar{x}}\right),
\end{aligned} \tag{C.12}$$

unveils the system. The general expression is given by

$$\tilde{q}^{(n)}(z^{(n)}|\bar{x}) = \frac{1}{\bar{x}^n} \frac{\left(z^{(n)}\right)^{n-1}}{(n-1)!} \exp\left(-\frac{z^{(n)}}{\bar{x}}\right), \tag{C.13}$$

as can be shown by induction. This is the distribution of a *sum* of single events. However, the distribution of the *mean*, Eq. (C.8), is needed. The transformation $x^{(n)} = z^{(n)}/n$ of Eq. (C.13), respecting

$$q^{(n)}(x^{(n)}|\bar{x})\, \mathrm{d}x^{(n)} = \tilde{q}^{(n)}(z^{(n)}|\bar{x})\, \mathrm{d}z^{(n)}, \tag{C.14}$$

yields the final result of Eq. (5.24)

$$\begin{aligned} q^{(n)}(x^{(n)}|\bar{x}) &= \frac{1}{\bar{x}^n}\,\frac{\left(x^{(n)}\,n\right)^{n-1}}{(n-1)!}\,\exp\left(-\frac{x^{(n)}\,n}{\bar{x}}\right)\,n \\ &= \frac{1}{\bar{x}}\,\frac{n^n}{(n-1)!}\,\left(\frac{x^{(n)}}{\bar{x}}\right)^{n-1}\,\exp\left(-\frac{x^{(n)}\,n}{\bar{x}}\right) \end{aligned} \tag{C.15}$$

for the distribution of the mean value $x^{(n)}$, Eq. (C.8). A comparison with Eq. (5.21) reveals that this corresponds to a χ^2-distribution with $2n$ degrees of freedom.

The next step is the transformation into logarithmic scale

$$\left.\begin{aligned} y^{(n)} &= \ln x^{(n)} \\ \eta &= \ln \bar{x} \end{aligned}\right\} \quad P^{(n)}(y^{(n)}|\eta)\,\mathrm{d}y^{(n)} = q^{(n)}(x^{(n)}|\bar{x})\,\mathrm{d}x^{(n)}\,, \tag{C.16}$$

which applied to Eq. (C.15) results in

$$\begin{aligned} P^{(n)}(y^{(n)}|\eta) &= e^{-n\,\eta}\,\frac{n^n}{(n-1)!}\,\left(e^{y^{(n)}}\right)^{n-1}\,\exp\left(-\frac{e^{y^{(n)}}\,n}{e^{\eta}}\right)\,e^{y^{(n)}} \\ &= e^{-n\,\eta}\,\frac{n^n}{(n-1)!}\,e^{(n-1)\,y^{(n)}}\,\exp\left(-n\,e^{y^{(n)}-\eta}\right)\,e^{y^{(n)}} \\ &= \frac{n^n}{(n-1)!}\,e^{n\left(y^{(n)}-\eta\right)}\,\exp\left(-n\,e^{y^{(n)}-\eta}\right)\,. \end{aligned} \tag{C.17}$$

The identification of the distance function works along the same lines as in Sec. C.1. An additive constant and a normalization N is introduced. This gives the distance function as

$$\begin{aligned} d^{(n)}(y^{(n)}|\eta) &= \frac{1}{N}\left(\mathrm{const} - \ln P^{(n)}(y^{(n)}|\eta)\right) \\ &= \frac{1}{N}\left(\mathrm{const} - \ln\frac{n^n}{(n-1)!} - n\,(y^{(n)}-\eta) + n\,e^{y^{(n)}-\eta}\right). \end{aligned} \tag{C.18}$$

Again, the constant is chosen to yield a minimum value of 0 for $d^{(n)}(y^{(n)}=\eta|\eta)$. The result is

$$d^{(n)}(y^{(n)}|\eta) = \frac{1}{N}\left(n\,e^{y^{(n)}-\eta} - n\,(y^{(n)}-\eta) - n\right) \tag{C.19}$$

and the normalization in the spirit of Eq. (C.6) fixes N to

$$N = n\,\left(\ln n - \psi(n)\right)\,, \tag{C.20}$$

where $\psi(n)$ is the Digamma function, the logarithmic derivative of the gamma function, given by $\psi(x) = \Gamma'(x)/\Gamma(x)$. This concludes the derivation of the distance function Eq. (5.25),

$$d^{(n)}(y^{(n)}|\eta) = \frac{\exp\left(y^{(n)} - \eta\right) - \left(y^{(n)} - \eta\right) - 1}{\ln n - \psi(n)}\,, \tag{C.21}$$

for averages of an ensemble measurement. In the GOF test η is given by the model and is a function of its parameters ζ.

C.3 Distribution of distances values

A summation of Eq. (C.7) over m data points leads to d_Σ as defined in Eq. (5.20). For the GOF test the probability distribution function of d_Σ is needed and will be derived [150] in the following. It is assumed that, in contrast to the previous section, the data points y_k arise from a single realization but are taken at different times t_k. The result Eq. (C.27) then holds for any number of realizations.

The calculation is based on Eq. (5.17) and Eqs. (5.19, 5.20) and yields

$$\begin{aligned} P(d_\Sigma) &= \int_{-\infty}^{+\infty} \{\mathrm{d}y_k\} \prod_{k=0}^{m-1} \left(\exp\left(-e^{y_k-\eta_k}\right)\, e^{y_k-\eta_k}\right) \\ &\quad \times \delta\left(d_\Sigma - \frac{1}{\gamma\, m} \sum_{l=0}^{m-1} \left(e^{y_l-\eta_l} - (y_l - \eta_l) - 1\right)\right)\,. \end{aligned} \tag{C.22}$$

Here, the integral is over $\{\mathrm{d}y_k\} = \prod_{k=0}^{m-1} \mathrm{d}y_k$. The definitions of $y_k = \ln x_k$ and $\eta_k = \ln \bar{x}_k$ allow the transformation back into the linear variables x_k and $\bar{x}_k$,

$$\begin{aligned} P(d_\Sigma) &= \gamma \int_0^{\infty} \{\mathrm{d}x_k\} \prod_{k=0}^{m-1} \left(\frac{1}{\bar{x}_k} e^{-x_k/\bar{x}_k}\right) \\ &\quad \times \delta\left(\gamma\, d_\Sigma - \frac{1}{m} \sum_{l=0}^{m-1} \left(\frac{x_l}{\bar{x}_l} - \ln \frac{x_l}{\bar{x}_l} - 1\right)\right) \qquad \text{(C.23)} \\ &= \gamma \int_0^{\infty} \{\mathrm{d}\tilde{x}_k\} \prod_{k=0}^{m-1} \left(e^{-\tilde{x}_k}\right)\, \delta\left(D - \frac{1}{m} \sum_{l=0}^{m-1} (\tilde{x}_l - \ln \tilde{x}_l)\right)\,. \qquad \text{(C.24)} \end{aligned}$$

Here, the abbreviations $\tilde{x}_k = x_k/\bar{x}_k$ and $D = \gamma\, d_\Sigma + 1$ have been introduced. For a further evaluation the Dirac δ-function is written in its Fourier representation,

$$\begin{aligned} P(d_\Sigma) &= \gamma \int_0^\infty \{\mathrm{d}\tilde{x}_k\} \prod_{k=0}^{m-1} \left(e^{-\tilde{x}_k}\right) \\ &\quad \times \int_{-\infty}^{+\infty} \frac{\mathrm{d}\alpha}{2\pi} \exp\left[i\,\alpha \left(D - \frac{1}{m} \sum_{l=0}^{m-1} (\tilde{x}_l - \ln \tilde{x}_l) \right) \right] \qquad \text{(C.25)} \\ &= \gamma \int_{-\infty}^{+\infty} \frac{\mathrm{d}\alpha}{2\pi}\, e^{i\,\alpha\, D} \\ &\quad \times \prod_{k=0}^{m-1} \int_0^\infty \mathrm{d}\tilde{x}_k \exp\left[-\left(1 + i\frac{\alpha}{m}\right) \tilde{x}_k + i\,\frac{\alpha}{m}\, \ln \tilde{x}_k \right] . \qquad \text{(C.26)} \end{aligned}$$

The integral over $\mathrm{d}\tilde{x}_k$ in Eq. (C.26) is analytically known. Thus the final result

$$P(d_\Sigma) = \gamma \int_{-\infty}^{+\infty} \frac{\mathrm{d}\alpha}{2\pi}\, e^{i\,\alpha\,(\gamma\, d_\Sigma + 1)} \left[\frac{\Gamma\left(1 + i\,\frac{\alpha}{m}\right)}{\left(1 + i\,\frac{\alpha}{m}\right)^{1 + i\,\frac{\alpha}{m}}} \right]^m \qquad \text{(C.27)}$$

is obtained. A further exact treatment of the problem is not feasible. However, numerical evaluations showed that a χ^2-distribution with m degrees of freedom, Eq. (5.22), is for all values of m a very good approximation to Eq. (C.27).

D Test for an exponential distribution

Given are N observed, independent events $x_1, \ldots, x_N$ following the same probability distribution p. The assumption of an exponential distribution

$$p(x_k) = e^{-x} \qquad \text{(D.1)}$$

of the x_k is to be verified by checking whether the necessary condition

$$\frac{\overline{x_k^2}}{\overline{x_k}^2} = \frac{2}{1^2} = 2 \qquad \text{(D.2)}$$

is fulfilled. The derivation presented in this section reproduces the work of Harney [140].

The moments required in Eq. (D.2) are not directly accessible. They are estimated from the data by

$$M_1 = \frac{1}{N} \sum_{k=1}^{N} x_k, \quad M_2 = \frac{1}{N} \sum_{k=1}^{N} x_k^2 . \qquad \text{(D.3)}$$

If assumption Eq. (D.1) holds, the variance of M_1 is

$$\begin{aligned}
\overline{M_1^2} - \overline{M_1}^2 &= \frac{1}{N^2}\left[\overline{\left(\sum_k x_k\right)^2} - \left(\sum_k \overline{x_k}\right)^2\right] \\
&= \frac{1}{N^2}\left[N\,(N-1) + \sum_k \overline{x_k^2} - N^2\right] \\
&= \frac{1}{N^2}\left[-N + 2\,N\right] = \frac{1}{N}\,, \qquad \text{(D.4)}
\end{aligned}$$

where $\overline{x_k^n} = n!$ has been used in the last line. Therefore, the first moment is estimated by $M_1 \pm (1/N)^{1/2}$. Further, if Eq. (D.1) holds, the variance of M_2 is

$$\begin{aligned}
\overline{M_2^2} - \overline{M_2}^2 &= \frac{1}{N^2}\left[\overline{\left(\sum_k x_k^2\right)^2} - \left(\sum_k \overline{x_k^2}\right)^2\right] \\
&= \frac{1}{N^2}\left[4\,N\,(N-1) + \sum_k \overline{x_k^4} - 4\,N^2\right] \\
&= \frac{1}{N^2}\left[-4\,N + 24\,N\right] = \frac{20}{N}\,. \qquad \text{(D.5)}
\end{aligned}$$

Hence the second moment is estimated by $M_2 \pm (20/N)^{1/2}$.

The results Eq. (D.4) and Eq. (D.5) can be written approximately as

$$\begin{aligned}
M_1 \pm \sqrt{\frac{1}{N}} &= M_1\left(1 \pm \sqrt{\frac{1}{N}}/M_1\right) \approx M_1\left(1 \pm \sqrt{\frac{1}{N}}/\overline{M_1}\right) \\
&\approx M_1\left(1 \pm \sqrt{\frac{1}{N}}\right)\,, \qquad \text{(D.6)} \\
M_2 \pm \sqrt{\frac{20}{N}} &\approx M_2\left(1 \pm \sqrt{\frac{20}{N}}/\overline{M_2}\right) \approx M_2\left(1 \pm \sqrt{\frac{20}{N}}/2\right) \\
&\approx M_2\left(1 \pm \sqrt{\frac{5}{N}}\right)\,. \qquad \text{(D.7)}
\end{aligned}$$

Gaussian error propagation now gives

$$\frac{M_2}{M_1^2}\left(1 \pm \sqrt{4\,N^{-1} + 5\,N^{-1}}\right) = \frac{M_2}{M_1^2}\left(1 \pm \sqrt{\frac{9}{N}}\right) \qquad \text{(D.8)}$$

as an approximation of Eq. (D.2) with a 1-σ error estimation.

References

[1] I. Newton: *Philosophiae naturalis principia mathematica* (Jussu Societas Regiae ac Typis Josephi Streater, London, 1686).

[2] H. Poincaré: *Les Méthodes Nouvelles de la Mécanique Céleste, Tome I* (Gauthier-Villars, Paris, 1892).

[3] A. N. Kolmogorov: *On Conservation of Conditionally-Periodic Motions for a Small Change in Hamilton's Function*, Dokl. Acad. Nauk. USSR **98**, 525 (1954).

[4] V. I. Arnold: *Small Denominators II, Proof of a Theorem of A. N. Kolmogorov on the Preservation of Conditionally-Periodic Motions under a Small Perturbation of the Hamiltionian*, Russ. Math. Surveys **18**, 5 (1963).

[5] J. Moser: *Convergent Series Expansions of Quasi-Periodic Motions*, Math. Ann. **169**, 163 (1967).

[6] E. Ott: *Chaos in dynamical systems* (Cambridge University Press, Cambridge, 1993).

[7] T.-Y. Li and J. A. Yorke: *Period Three Implies Chaos*, Amer. Math. Monthly **82**, 985 (1975).

[8] Y. G. Sinai: *Dynamical systems with elastic reflections*, Russ. Math. Surv. **25**, 137 (1970).

[9] L. A. Bunimovich: *On the Ergodic Properties of Nowhere Dispersing Billiards*, Comm. Math. Phys. **65**, 295 (1979).

[10] M. V. Berry: *Regularity and chaos in classical mechanics, illustrated by three deformations of a circular 'billiard'*, Eur. J. Phys. **2**, 91 (1981).

[11] M. C. Gutzwiller: *Energy Spectrum According to Classical Mechanics*, J. Math. Phys. **11**, 1791 (1970).

[12] S. W. McDonald and A. N. Kaufman: *Spectrum and Eigenfunctions for a Hamiltonian with Stochastic Trajectories*, Phys. Rev. Lett. **42**, 1189 (1979).

[13] O. Bohigas, M. J. Giannoni, and C. Schmit: *Characterization of Chaotic Quantum Spectra and Universality of Level Fluctuation Laws*, Phys. Rev. Lett. **52**, 1 (1984).

[14] M. C. Gutzwiller: in *Chaos in Classical and Quantum Mechanics*, Interdisciplinary Applied Mathematics, Ed.: F. John, L. Kadanoff, J. E. Marsden, L. Sirovich, and S. Wiggins (Springer, New York, 1990).

[15] M. Brack and K. Bhaduri: *Semicalssical Physics* (Westview Press, Boulder, 2003).

[16] E. Doron, U. Smilansky, and A. Frenkel: *Experimental Demonstration of Chaotic Scattering of Microwaves*, Phys. Rev. Lett. **65**, 3072 (1990).

[17] H.-J. Stöckmann and J. Stein: *"Quantum" Chaos in Billiards Studied by Microwave Absorption*, Phys. Rev. Lett. **64**, 2215 (1990).

[18] H.-D. Gräf, H. L. Harney, H. Lengeler, C. H. Lewenkopf, C. Rangacharyulu, A. Richter, P. Schardt, and H. A. Weidenmüller: *Distribution of Eigenmodes in a Superconducting Stadium Billiard with Chaotic Dynamics*, Phys. Rev. Lett. **69**, 1296 (1992).

[19] A. Richter: *Playing Billiards with Microwaves — Quantum Manifestations of Classical Chaos*, in *Emerging Applications of Number Theory*, **109**, The IMA Volumes in Mathematics and its Applications, Ed.: D. A. Hejhal, J. Friedmann, M. C. Gutzwiller, and A. M. Odlyzko (Springer, New York, 1999), p. 479.

[20] P. So, S. M. Anlage, E. Ott, and R. N. Oerter: *Wave Chaos Experiments with and without Time Reversal Symmetry: GUE and GOE Statistics*, Phys. Rev. Lett. **74**, 2662 (1995).

[21] U. Stoffregen, J. Stein, H.-J. Stöckmann, M. Kuś, and F. Haake: *Microwave Billiards with Broken Time Reversal Symmetry*, Phys. Rev. Lett. **74**, 2666 (1995).

[22] J. H. Christenson, J. W. Cronin, V. L. Fitch, and R. Turlay: *Evidence for the* 2π *Decay of the* K_2^0 *Meson*, Phys. Rev. Lett. **13**, 138 (1964).

[23] J. J. Sakurai: in *Modern Quantum Mechanics*, 1st edition, Ed.: S. F. Tuan (Addison-Wesley Publishing Company, Inc., California, 1985).

[24] D. Bodansky, W. J. Braithwaite, D. C. Shreve, D. W. Storm, and W. G. Weitkamp: *Tests of Time-Reversal Invariance in the Reactions* $Mg^{24} + d \rightleftarrows Mg^{25} + p$, Phys. Rev. Lett. **17**, 589 (1966).

[25] W. G. Weitkamp, D. W. Storm, D. C. Shreve, W. J. Braithwaite, and D. Bodansky: *Test of Time-Reversal Invariance in the Reactions* $Mg^{24} + d \rightleftarrows Mg^{25} + p$, Phys. Rev. **165**, 1233 (1968).

[26] W. von Witsch, A. Richter, and P. von Brentano: *A test of time-reversal invariance in the reactions* $^{24}Mg(\alpha, p)^{27}Al$ *and* $^{27}Al(p, \alpha)^{24}Mg$, Phys. Lett. **22**, 631 (1966).

[27] W. von Witsch, A. Richter, and P. von Brentano: *Upper Limit of T Non-conservation in the Reactions* $^{24}Mg + \alpha \rightleftarrows {}^{27}Al + p$, Phys. Rev. Lett. **19**, 524 (1967).

[28] S. T. Thornton, C. M. Jones, J. K. Bair, M. D. Mancusi, and H. B. Willard: *Test of Time-Reversal Invariance in the Reactions* $^{16}O(d, \alpha)^{14}N$ *and* $^{14}N(\alpha, d)^{16}O$, Phys. Rev. C **3**, 1065 (1971).

[29] A. Richter: *Present Status of Time-Reversal Invariance in the Nuclear Interactions*, in *Interaction Studies in Nuclei*, Ed.: H. Jochim and B. Ziegler (North-Holland Publ. Co., Amsterdam, 1975), p. 191.

[30] E. Blanke, H. Driller, W. Glöckle, H. Genz, A. Richter, and G. Schrieder: *Improved Experimental Test of Detailed Balance and Time Reversibility in the Reactions* $^{27}Al + p \rightleftharpoons {}^{24}Mg + \alpha$, Phys. Rev. Lett. **51**, 355 (1983).

[31] H. L. Harney, A. Hüpper, and A. Richter: *Ericson fluctuations, detailed balance and time-reversal invariance*, Nucl. Phys. A **518**, 35 (1990).

[32] V. E. Bunakov, H. L. Harney, and A. Richter: *Bayesian statistics and experiments on stochastic variables*, Nucl. Phys. A **560**, 71 (1993).

[33] T. Ericson: *Fluctuations of Nuclear Cross Sections in the "Continuum" Region*, Phys. Rev. Lett. **5**, 430 (1960).

[34] T. Ericson: *Nuclear enhancement of T violation effects*, Phys. Lett. **23**, 97 (1966).

[35] C. Mahaux and H. A. Weidenmüller: *Compound nuclear reactions as a test of T-invariance*, Phys. Lett. **23**, 100 (1966).

[36] E. M. Henley and B. A. Jacobsohn: *Time Reversal in Nuclear Interactions*, Phys. Rev. **113**, 225 (1959).

[37] J. M. Pearson and A. Richter: *Time-reversibility violation and isolated nuclear resonances*, Phys. Lett. B **56**, 112 (1975).

[38] H. Driller, E. Blanke, H. Genz, A. Richter, G. Schrieder, and J. M. Pearson: *Test of detailed balance at isolated resonances in the reactions* $^{27}Al+p\rightleftharpoons^{24}Mg+\alpha$ *and time reversibility*, Nucl. Phys. A **317**, 300 (1979).

[39] B. Dietz, T. Friedrich, H. L. Harney, M. Miski-Oglu, A. Richter, F. Schäfer, and H. A. Weidenmüller: *Induced Time-Reversal Symmetry Breaking Observed in Microwave Billiards*, Phys. Rev. Lett. **98**, 074103 (2007).

[40] C. H. Lewenkopf, A. Müller, and E. Doron: *Microwave scattering in an irregularly shaped cavity: Random-matrix analysis*, Phys. Rev. A **45**, 2635 (1992).

[41] S. Albeverio, F. Haake, P. Kurasov, M. Kuś, and P. Šeba: *S-matrix, resonances, and wave functions for transport through billiards with leads*, J. Math. Phys. **37**, 4888 (1996).

[42] H. Alt, H.-D. Gräf, T. Guhr, H. L. Harney, R. Hofferbert, H. Rehfeld, A. Richter, and P. Schardt: *Correlation-hole method for the spectra of superconducting microwave billiards*, Phys. Rev. E **55**, 6674 (1997).

[43] C. Mahaux and H. A. Weidenmüller: *Shell-Model Approach to Nuclear Reactions* (North-Holland Publ. Co., Amsterdam, 1969).

[44] C. M. Marcus, A. J. Rimberg, R. M. Westervelt, P. F. Hopkins, and A. C. Gossard: *Conductance Fluctuations and Chaotic Scattering in Ballistic Microstructures*, Phys. Rev. Lett. **69**, 506 (1992).

[45] M. C. Gutzwiller: *Nobel Symposium: Quantum Chaos Y2K*, Phys. Scr. **T90**, 13 (2001).

[46] N. Agraït, A. L. Yeyati, and J. M. van Ruitenbeek: *Quantum properties of atomic-sized conductors*, Phys. Rep. **377**, 81 (2003).

[47] H. A. Weidenmüller: *Ericson fluctuations versus conductance fluctuations: Similarities and differences*, Nucl. Phys. A **518**, 1 (1990).

[48] J. J. M. Verbaarschot, H. A. Weidenmüller, and M. R. Zirnbauer: *Grassmann integration and the theory of compound-nucleus reactions*, Phys. Lett. B **149**, 263 (1984).

[49] T. Friedrich: *Eigenschaften von Pilzbillards und Korrelationsfunktionen von Streumatrixelementen in Mikrowellenresonatoren*, Dissertation D17, TU Darmstadt, 2007.

[50] Y. V. Fyodorov, D. V. Savin, and H.-J. Sommers: *Scattering, reflection and impedance of waves in chaotic and disordered systems with absorption*, J. Phys. A: Math. Gen. **38**, 10731 (2005).

[51] G. Bergmann: *Weak localization in thin films, a time-of-flight experiment with conduction electrons*, Phys. Rep. **107**, 1 (1984).

[52] A. Buchleitner, I. Guarneri, and J. Zakrzewski: *Conductance fluctuations in microwave-driven Rydberg atoms*, Europhys. Lett. **44**, 162 (1998).

[53] J. Madroñero and A. Buchleitner: *Ericson Fluctuations in an Open Deterministic Quantum System: Theory Meets Experiment*, Phys. Rev. Lett. **95**, 263601 (2005).

[54] L. E. Reichl: *The Transition to Chaos: Conservative Classical Systems and Quantum Manifestations* (Springer-Verlag, New York, 2004).

[55] E. Noether: *Invariante Variantionsprobleme*, Nachr. v. d. Ges. d. Wiss. zu Göttingen **2**, 235 (1918).

[56] H.-J. Stöckmann: *Quantum Chaos: an introduction* (Cambridge University Press, Cambridge, UK, 1999).

[57] F. Haake: in *Quantum Signatures of Chaos*, 2nd edition, Ed.: H. Haken (Springer-Verlag, Berlin Heidelberg New York, 2000).

[58] H. A. Weidenmüller: *Chaos in Atomkernen*, Physik Journal **3**, 41 (2004).

[59] T. Guhr, A. Müller-Groeling, and H. A. Weidenmüller: *Random-matrix theories in quantum physics: common concepts*, Phys. Rep. **299**, 189 (1998).

[60] R. L. Weaver: *Spectral statistics in elastodynamics*, J. Acoust. Soc. Am. **85**, 1005 (1989).

[61] T. Gensty, K. Becker, I. Fischer, W. Elsäßer, C. Degen, P. Debernardi, and G. P. Bava: *Wave Chaos in Real-World Vertical-Cavity Surface-Emitting Lasers*, Phys. Rev. Lett. **94**, 233901 (2005).

[62] R. U. Haq, A. Pandey, and O. Bohigas: *Fluctuation Properties of Nuclear Energy Levels: Do Theory and Experiment Agree?*, Phys. Rev. Lett. **48**, 1086 (1982).

[63] O. Bohigas and H. A. Weidenmüller: *Aspects of Chaos in Nuclear Physics*, Ann. Rev. Nucl. Part. Sci. **38**, 421 (1988).

[64] J. F. Shriner, E. G. Bilpuch, P. M. Endt, and G. E. Mitchell: *Fluctuation Properties of States in* $^{26}Al^{*}$, Z. Phys. A **335**, 393 (1990).

[65] V. M. Akulin, C. Bréchignac, and A. Sarfati: *Quantum Shell Effect on Dissociation Energies, Shapes, and Thermal Properties of Metallic Clusters from the Random Matrix Model*, Phys. Rev. Lett. **75**, 220 (1995).

[66] S. Drożdż, A. Trellakis, and J. Wambach: *Spectral Decorrelation of Nuclear Levels in the Presence of Continuum Decay*, Phys. Rev. Lett. **76**, 4891 (1996).

[67] C. W. J. Beenakker: *Random-matrix theory of quantum transport*, Rev. Mod. Phys. **69**, 731 (1997).

[68] J. D. Jackson: *Classical Electrodynamics* (John Wiley and Sons, New York, 1999).

[69] C. Dembowski: *Aufbau eines modularen supraleitenden Hohlraumresonators auf der Basis von verbleitem Kupfer und Anderson-Lokalisierung in Mikrowellenbillards*, Diplomarbeit, TU Darmstadt, 1997 (unpublished).

[70] J.-L. Thomas, P. Roux, and M. Fink: *Inverse Scattering Analysis with an Acoustic Time-Reversal Mirror*, Phys. Rev. Lett. **72**, 637 (1994).

[71] J. de Rosny, A. Tourin, A. Derode, P. Roux, and M. Fink: *Weak Localization and Time Reversal of Ultrasound in a Rotational Flow*, Phys. Rev. Lett. **95**, 074301 (2005).

[72] A. Kaminski, S. Rosenkranz, H. M. Fretwell, J. C. Campuzano, Z. Li, H. Raffy, W. G. Cullen, H. You, C. G. Olson, C. M. Varma, and H. Höchst: *Spontaneous breaking of time-reversal symmetry in the pseudogap state of a high-T_c superconductor*, Nature **416**, 610 (2002).

[73] A. P. Mackenzie and Y. Maeno: *The superconductivity of Sr_2RuO_4 and the physics of spin-triplet pairing*, Rev. Mod. Phys. **75**, 657 (2003).

[74] B. Braunecker, P. A. Lee, and Z. Wang: *Edge Currents in Superconductors with a Broken Time-Reversal Symmetry*, Phys. Rev. Lett. **95**, 017004 (2005).

[75] T. Mayer-Kuckuk: *Kernphysik: Eine Einführung*, 7^{th} edition (Vieweg+Teubner, Wiesbaden, 2002).

[76] C. Kittel: *Einführung in die Festkörperphysik*, 13^{th} edition (Oldenbourg Verlag, München, 2002).

[77] B. Lax and K. J. Button: *Microwave ferrites and ferrimagnetics* (McGraw-Hill, New York, 1962).

[78] S. Krupička: *Physik der Ferrite und der verwandten magnetischen Oxide* (Friedr. Vieweg + Sohn, Braunschweig, 1973).

[79] F. Schäfer: *Untersuchung der Zeitumkehrinvarianz in Quantenbillards*, Diplomarbeit, TU Darmstadt, 2005 (unpublished).

[80] C. Dembowski, H.-D. Gräf, A. Heine, R. Hofferbert, H. Rehfeld, , and A. Richter: *First Experimental Evidence for Chaos-Assisted Tunneling in a Microwave Annular Billiard*, Phys. Rev. Lett. **84**, 867 (2000).

[81] R. Hofferbert, H. Alt, C. Dembowski, H.-D. Gräf, H. L. Harney, A. Heine, H. Rehfeld, and A. Richter: *Experimental investigations of chaos-assisted tunneling in a microwave annular billiard*, Phys. Rev. E **71**, 046201 (2005).

[82] R. Hofferbert: *Wellendynamisches Chaos in einem supraleitenden 3D-Sinai-Billard und Chaos-induziertes Tunneln in einem 2D-Ring-Billard*, Dissertation D17, TU Darmstadt, 1999.

[83] D. H. Wu, J. S. A. Bridgewater, A. Gokirmak, and S. M. Anlage: *Probability Amplitude Fluctuations in Experimental Wave Chaotic Eigenmodes with and Without Time-Reversal Symmetry*, Phys. Rev. Lett. **81**, 2890 (1998).

[84] H. Schanze, H.-J. Stöckmann, M. Martínez-Mares, and C. H. Lewenkopf: *Universal transport properties of open microwave cavities with and without time-reversal symmetry*, Phys. Rev. E **71**, 016223 (2005).

[85] O. Bohigas: *Random matrix theories and chaotic dynamics*, in *Chaos et Physique Quantique/Chaos and Quantum Physics*, Les Houches, Ed.: M.-J. Giannoni, A. Voros, and J. Zinn-Justin (Elsevier Science Publishers, Amsterdam, 1991).

[86] F. J. Dyson: *A Brownian-Motion Model for the Eigenvalues of a Random Matrix*, J. Math. Phys. **3**, 1191 (1962).

[87] A. Pandey: *Statistical properties of many-particle spectra. IV. New ensembles by Stieltjes transform methods*, Ann. Phys. **134**, 110 (1981).

[88] H. Alt, C. I. Barbosa, H.-D. Gräf, T. Guhr, H. L. Harney, R. Hofferbert, H. Rehfeld, and A. Richter: *Coupled Microwave Billiards as a Model for Symmetry Breaking*, Phys. Rev. Lett. **81**, 4847 (1998).

[89] B. Dietz, T. Guhr, H. L. Harney, and A. Richter: *Strength Distributions and Symmetry Breaking in Coupled Microwave Billiards*, Phys. Rev. Lett. **96**, 254101 (2006).

[90] B. Dietz, B. Mößner, T. Papenbrock, U. Reif, and A. Richter: *Bouncing ball orbits and symmetry breaking effects in a three-dimensional chaotic billiard*, Phys. Rev. E **77**, 046221 (2008).

[91] R. L. Weaver and O. I. Lobkis: *Enhanced Backscattering and Modal Echo of Reverberant Elastic Waves*, Phys. Rev. Lett. **84**, 4942 (2000).

[92] U. Kuhl, H.-J. Stöckmann, and R. Weaver: *Classical wave experiments on chaotic scattering*, J. Phys. A **38**, 10433 (2005).

[93] T. Ericson and T. Mayer-Kuckuk: *Fluctuations in Nuclear Reactions*, Ann. Rev. Nucl. Sci. **16**, 183 (1966).

[94] L. Colli, U. Facchini, I. Iori, G. M. Marcazzan, M. Milazzo, and F. Tonolini: *Fluctuations in the cross section of* $Si^{28}(n,\ \alpha)Mg^{25}$ *reaction with fast neutrons*, Phys. Lett. **1**, 120 (1962).

[95] U. Facchini, E. S. Menichella, and F. Tonolini: *Statistical emission and Ericson fluctions in* $(p,\ \alpha)$ *and* $(d,\ \alpha)$ *reactions*, Phys. Lett. **1**, 209 (1962).

[96] P. von Brentano, J. Ernst, O. Häusser, T. Mayer-Kuckuk, A. Richter, and W. V. Witsch: *Statistical fluctuations in the cross sections of the reactions* $Cl^{35}(p,\ \alpha)S^{32}$ *and* $Cl^{37}(p,\ \alpha)S^{34}$, Phys. Lett. **9**, 48 (1964).

[97] B. W. Allardyce, P. J. Dallimore, I. Hall, N. W. Tanner, A. Richter, P. von Brentano, and T. Mayer-Kuckuk: *An analysis of cross-section fluctuations in the region* $^{26}Mg(p,\ \alpha)^{23}Na$, Nucl. Phys. **85**, 193 (1965).

[98] B. W. Allardyce, P. J. Dallimore, I. Hall, N. W. Tanner, A. Richter, P. von Brentano, and T. Mayer-Kuckuk: *Modulated fluctuations in the reaction* $^{26}Mg(p,\ \alpha)^{23}Na$, Phys. Lett. **18**, 140 (1965).

[99] A. Richter: *Die Untersuchung der Kernreaktion* $^{26}Mg\,(p,\,\alpha)\,^{23}Na$ *und die Interpretation des Reaktionsmechanismus mit einem modifizierten statistischen Modell*, Dissertation, Ruprecht-Karl-Universität Heidelberg, 1966.

[100] J. J. M. Verbaarschot, H. A. Weidenmüller, and M. R. Zirnbauer: *Grassmann integration in stochastic quantum physics: The case of compound-nucleus scattering*, Phys. Rep. **129**, 367 (1985).

[101] T. Ericson: *A Theory of Fluctuations in Nuclear Cross Sections*, Ann. of Phys. (N.Y.) **23**, 390 (1963).

[102] B. Dietz, T. Friedrich, H. L. Harney, M. Miski-Oglu, A. Richter, F. Schäfer, and H. A. Weidenmüller: *Chaotic Scattering in the Regime of Weakly Overlapping Resonances*, Phys. Rev. E **78**, 055204(R) (2008).

[103] H. Primack and U. Smilansky: *Quantal consequences of perturbations which destroy structurally unstable orbits in chaotic billiards*, J. Phys. A **27**, 4439 (1994).

[104] M. Taheri Gelevarzi: *Gekoppelte Mikrowellenbillards unterschiedlicher Größen*, Diplomarbeit, TU Darmstadt, 2006 (unpublished).

[105] H. Schanze, E. R. P. Alves, C. H. Lewenkopf, and H.-J. Stöckmann: *Transmission fluctuations in chaotic microwave billiards with and without time-reversal symmetry*, Phys. Rev. E **64**, 065201(R) (2001).

[106] R. Schäfer, H.-J. Stöckmann, T. Gorin, and T. H. Seligman: *Experimental Verification of Fidelity Decay: From Perturbative to Fermi Golden Rule Regime*, Phys. Rev. Lett. **95**, 184102 (2005).

[107] S. Hemmady, X. Zheng, E. Ott, T. M. Antonsen, and S. M. Anlage: *Universal Impedance Fluctuations in Wave Chaotic Systems*, Phys. Rev. Lett. **94**, 014102 (2005).

[108] H. Weyl: *Über die Abhängigkeit der Eigenschwingungen einer Membran von deren Begrenzung*, Journal f. Mathematik **141**, 1 (1912).

[109] H. Weyl: *Über das Spektrum der Hohlraumstrahlung*, Journal f. Mathematik **141**, 163 (1912).

[110] H. P. Baltes and E. R. Hilf: *Spectra of Finite Systems* (Bibliographisches Institut, Mannheim, 1976).

[111] W. von Witsch, A. Richter, and P. von Brentano: in *Proceedings of the International Conference on Nuclear Physics, Gatlinburg, Tennessee, 1966* (Academic Press Inc., New York, 1967), discussion remark by H. A. Weidenmüller.

[112] W. von Witsch, A. Richter, and P. von Brentano: *Test of Time-Reversal Invariance through the Reactions* $^{24}Mg + \alpha \rightleftharpoons {}^{27}Al + p$, Phys. Rev. **169**, 923 (1968).

[113] E. Blanke: *Test der Zeitumkehrinvarianz in der starken Wechselwirkung über das Prinzip des detaillierten Gleichgewichts in den Reaktionen* $^{27}Al + p \rightleftharpoons ^{24}Mg + \alpha$ *bei niedrigen Energien*, Dissertation, Ruhr-Universität Bochum, 1977.

[114] N. Bohr: *Neutron Capture and Nuclear Constitution*, Nature **137**, 344 (1936).

[115] P. W. Brouwer and C. W. J. Beenakker: *Voltage-probe and imaginary-potential models for dephasing in a chaotic quantum dot*, Phys. Rev. B **55**, 4695 (1997).

[116] R. Schäfer, T. Gorin, T. H. Seligman, and H.-J. Stöckmann: *Correlation functions of scattering matrix elements in microwave cavities with strong absorption*, J. Phys. A: Math. Gen. **36**, 3289 (2003).

[117] H. A. Weidenmüller: in *Scattering*, Ed.: E. R. Pike and P. C. Sabatier (Academic Press Inc., New York, 2000), Chap. 3.1.4, p. 1393.

[118] C. A. Engelbrecht and H. A. Weidenmüller: *Hauser-Feshbach Theory and Ericson Fluctuations in the Presence of Direct Reactions*, Phys. Rev. C **8**, 859 (1973).

[119] H. K. Vonach, A. Katsanos, and J. R. Huizenga: *Cross-Section Fluctuations in the* Mn^{55} (p, α) Cr^{52} *Reaction*, Phys. Rev. Lett. **13**, 88 (1964).

[120] C. Mahaux and H. A. Weidenmüller: *Recent Developments in Compound-Nucleus Theory*, Ann. Rev. Nucl. Part. Sci. **29**, 1 (1979).

[121] W. Hauser and H. Feshbach: *The Inelastic Scattering of Neutrons*, Phys. Rev. **87**, 366 (1952).

[122] O. Bohigas and M.-J. Giannoni: in *Chaotic motion and random matrix theories*, **209**, Lecture Notes in Physics (Springer, Berlin-Heidelberg, 1984), p. 1.

[123] K. B. Efetov: *Supersymmetry and theory of disordered metals*, Adv. in Phys. **32**, 53 (1983).

[124] K. Efetov: *Supersymmetry in Disorder and Chaos* (Cambridge University Press, Cambridge, 1997).

[125] J. J. M. Verbaarschot: *Investigation of the formula for the average of two S-matrix elements in compound nucleus reactions*, Ann. Phys. **168**, 368 (1986).

[126] H. A. Weidenmüller: *Statistical Theory of Nuclear Reactions and the Gaussian Orthogonal Ensemble*, Ann. Phys. **158**, 120 (1984).

[127] J. M. Blatt and V. F. Weisskopf: *Theoretical Nuclear Physics* (Springer, New York, 1979).

[128] D. Agassi, H. A. Weidenmüller, and G. Mantzouranis: *The statistical theory of nuclear reactions for strongly overlapping resonances as a theory of transport phenomena*, Phys. Rep. **22**, 145 (1975).

[129] A. Richter, W. Von Witsch, P. von Brentano, O. Häusser, and T. Mayer-Kuckuk: *The level densities in the compound nuclei Al^{27} and Ar^{38} at 20 MeV excitation energy*, Phys. Lett. **14**, 121 (1965).

[130] H. Feshbach: *Unified theory of nuclear reactions*, Ann. Phys. **5**, 357 (1958).

[131] J. Verbaarschot: *S-Matrix Fluctuations with Broken Time Reversal Invariance*, 2007, private communication.

[132] W. R. Gibbs: *Finite-Sample-Size Effects in Nuclear Cross-Section Fluctuations*, Phys. Rev. **139**, B1185 (1965).

[133] P. J. Dallimore and I. Hall: *An analysis of some synthetic cross-section fluctuation data*, Nucl. Phys. **88**, 193 (1966).

[134] M. Böhning and A. Richter: *Spectral analysis of fluctuations in the reaction $^{26}Mg(p, \alpha)^{23}Na$*, in *Recent Progress in Nuclear Physics with Tandems*, Ed.: W. Hering (MPI, Heidelberg, Germany, 1966), p. 15.

[135] J. Hellström and P. J. Dallimore: *Level widths in the compound nucleus ^{32}S from the reaction $^{31}P(p, p_0)$*, Nucl. Phys. A **125**, 684 (1969).

[136] T. Ericson: in *Lectures in theoretical physics, Vol VIII C — Nuclear Structure Physics*, Ed.: P. D. Kunz, D. A. Lind, and W. E. Brittin (University Press, Boulder, 1965).

[137] T. Gorin and T. H. Seligman: *Signatures of the correlation hole in total and partial cross sections*, Phys. Rev. E **65**, 026214 (2002).

[138] H. Alt, H. D. Gräf, H. L. Harney, R. Hofferbert, H. Lengeler, A. Richter, P. Schardt, and H. A. Weidenmüller: *Gaussian Orthogonal Ensemble Statistics in a Microwave Stadium Billiard with Chaotic Dynamics: Porter-Thomas Distribution and Algebraic Decay of Time Correlations*, Phys. Rev. Lett. **74**, 62 (1995).

[139] A. Chintchin: *Korrelationstheorie stationärer Prozesse*, Math. Ann. **109**, 604 (1934).

[140] H. L. Harney: *Überprüfung des zweiten Moments der Exponentialverteilung*, 2008, private communication.

[141] J. A. Nelder and R. Mead: *A Simplex Method for Function Minimization*, The Comp. Journ. **7**, 308 (1965).

[142] H. L. Harney, A. Richter, and H. A. Weidenmüller: *Breaking of isospin symmetry in compound-nucleus reactions*, Rev. Mod. Phys. **58**, 607 (1986).

[143] G. E. Mitchell, E. G. Bilpuch, P. M. Endt, and J. F. Shriner: *Broken Symmetries and Chaotic Behavior in* ^{26}Al, Phys. Rev. Lett. **61**, 1473 (1988).

[144] S. Åberg, A. Heine, G. Mitchell, and A. Richter: *Isospin symmetry breaking in* ^{93}Tc *and statistical properties*, Phys. Lett. B **598**, 42 (2004).

[145] H. Alt: *Gekoppelte supraleitende Mikrowellenbillards als Modellsystem für Symmetriebrechung*, Dissertation D17, TU Darmstadt, 1998.

[146] H.-J. Sommers and S. Iida: *Eigenvector statistics in the crossover region between Gaussian orthogonal and unitary ensembles*, Phys. Rev. E **49**, R2513 (1994).

[147] Z. Pluhař, H. A. Weidenmüller, J. A. Zuk, and C. H. Lewenkopf: *Suppression of Weak Localization due to Magnetic Flux in Few-Channel Ballistic Microstructures*, Phys. Rev. Lett. **73**, 2115 (1994).

[148] Z. Pluhař, H. A. Weidenmüller, J. A. Zuk, C. H. Lewenkopf, and F. J. Wegner: *Crossover from Orthogonal to Unitary Symmetry for Ballistic Electron Transport in Chaotic Microstructures*, Ann. Phys. **243**, 1 (1995).

[149] F. Haake, M. Kuś, P. Šeba, H.-J. Stöckmann, and U. Stoffregen: *Microwave billiards with broken time reversal invariance*, J. Phys. A: Math. Gen. **29**, 5745 (1996).

[150] B. Dietz: 2008, private communication.

[151] M. V. Berry: *Regular and irregular semiclassical wavefunctions*, J. Phys. A **10**, 2083 (1977).

[152] G. R. Satchler: *Average compound nucleus cross sections in the continuum*, Phys. Lett. **7**, 55 (1963).

[153] W. Kretschmer and M. Wangler: *Model-Independent Determination of the Compound-Elastic Enhancement Factor in a Polarized-Proton Fluctuation Experiment*, Phys. Rev. Lett. **41**, 1224 (1978).

[154] J. W. Tepel, H. M. Hofmann, and H. A. Weidenmüller: *Hauser-Feshbach formulas for medium and strong absorption*, Phys. Lett. B **49**, 1 (1974).

[155] H. L. Harney, H. A. Weidenmüller, and A. Richter: *Elastic enhancement factor in charge exchange reactions*, Phys. Lett. B **96**, 227 (1980).

[156] D. V. Savin, Y. V. Fyodorov, and H. J. Sommers: *Correlation Functions of Impedance and Scattering Matrix Elements in Chaotic Absorbing Cavities*, Acta Phys. Pol. A **109**, 53 (2006), proceedings of the 2nd Workshop on Quantum Chaos and Localisation Phenomena, Warsaw, Poland, May 19-22.

[157] H. L. Harney and H. A. Weidenmüller: 2008, private communication.

[158] H. L. Harney: *FRD-Fehler*, 2007, private communication.

[159] H. L. Harney: *Bayesian Statistics — Parameter Estimation and Decisions* (Springer Verlag, Heidelberg, 2003).

Acknowledgments

Finally I want to say a big "Thank you" to all the people that helped and supported me during this work. Physics has become a very complex field and no one can know everything or do everything by himself anymore. Here at the Institute of Nuclear Physics of the TU Darmstadt both, the people and the equipment, are just what you need to give your best.

My special thanks go to Professor Dr. Dr. h.c. mult. Achim Richter. You had faith in me, gave me the proper challenges and the allies to solve them. Your striving for excellence gave me a feeling of how things should be done. You are a man of your word and stand by your people if help is needed. And you gave me the possibility to go to Maryland, which was and is a great scientific and personal experience to me. I further have to thank Professor Dr. Hanns Ludwig Harney. You have open ears and an open heart for every problem. Your expertise in statistical analyses made you an invaluable asset in my quest. Thanks also to Professor Dr. Hans Arwed Weidenmüller. Your mind is as sharp as ever and any theory that passes your judgment may pass anything. I further thank you, Professor Jacobus Verbaarschot, for contributing your computer code and your derivation of the GUE formula. Thank you Professor Steven Mark Anlage, you are a great adviser, I was never more inspired than during these three month in your group. And thanks to you I am now known as the "impedance man".

Six especially big thank you go to my (former) colleagues. Barbara, your calculations and knowledge of Fortran made my day. Thomas, I will miss the evenings we spent discussing the seemingly most innocent yet most puzzling topics. Maksim, you are still the undisputed number one when discussing experimental questions. Stefan, everyone should have such a faithful beta tester for ones computer programs as you have been. Pedro, your experiments made me learn a lot about cold measurements and our Helium system. And Majid, without your billiard half of my work could not have been done. Kudos to all of you!

Last but not least my thanks go to the Graduiertenkolleg 410 and the Deutsche Telekom Foundation for their support. Thank you Christiane Frense-Heck and Dr. Klaus-Jürgen Krath for your personal efforts. This work was supported by DFG within SFB 634.

Lebenslauf

Florian Schäfer

05. Juli 1980	geboren in Dieburg
1987–2000	Schulausbildung (Grundschule, Gymnasium, Gymnasiale Oberstufe) in Dieburg
Juni 2000	Abitur
2000–2005	Studium der Physik an der Technischen Universität Darmstadt
September 2005	Diplom in Physik; Abschluss des Studiums
seit Oktober 2005	Doktorand am Institut für Kernphysik der Technischen Universität Darmstadt
2005–2006	Promotionsstipendium des „Graduiertenkolleg 410“ der Deutschen Forschungsgemeinschaft
seit Januar 2007	Promotionsstipendium der Deutsche Telekom Stiftung